

**Expression, purification and structural analysis of  
key components of the *Shigella* T3SS basal body in two states**

Dissertation

Zur Erlangung des naturwissenschaftlichen Doktorgrades

Doctor rerum naturalium  
(Dr. rer. nat)

eingereicht an der

Fakultät für Mathematik, Informatik und Naturwissenschaften  
im Fachbereich Chemie  
der Universität Hamburg

vorgelegt von Antje Kamprad

Hamburg, 2019



This work was carried out from October 2014 till December 2016 at the Max Planck Institute for Infection Biology Berlin and was continued till December 2019 at the Helmholtzzentrum für Infektionsforschung (HZI) at the University of Hamburg at DESY Campus under the supervision of Prof. Dr. Michael Kolbe.

This work has partially been published as a research manuscript:

“Cryo-EM structure of the *Shigella* type III needle complex”; Michele Lunelli, Antje Kamprad, Jörg Bürger, Thorsten Mielke, Christian M.T. Spahn and Michael Kolbe, Plos Pathogens, accepted December 2019

**Gutachter der Dissertation:**

- |               |                         |
|---------------|-------------------------|
| 1. Gutachter: | Prof. Dr. Michael Kolbe |
| 2. Gutachter  | Prof. Dr. Henning Tidow |

**Disputation – Datum: Freitag 06.03.2020**

**Prüfungskommission**

- |                     |                         |
|---------------------|-------------------------|
| 1. Vorsitz:         | Prof. Dr. Michael Kolbe |
| 2. Stellv. Vorsitz: | Prof. Dr. Arwen Pearson |
| 3. Beisitz:         | Dr. Charlotte Uetrecht  |



# Zusammenfassung

*Shigella flexneri* ist ein gram-negatives Bakterium, welches den menschlichen Darm mit Hilfe des Typ-3-Sekretionssystems (T3SS) befällt. Das T3SS ist ein Transmembrantransporter und für eine erfolgreiche Infektion unabdingbar. Ein hervorstechendes Merkmal des T3SS ist der Basalkörper, bestehend aus einem inneren und äußeren Membranring, welche eine Nadel-artige Struktur die mit einem kurzen Hohlzylinder, dem inner rod, verbunden ist umschließen [1]. Der Basalkörper in Verbindung mit den Basalkörper-assoziierten Bestandteilen des Exportapparates wird Nadelkomplex genannt und kann aus der Bakterienmembran isoliert werden. Um den Infektionsprozess zu ermöglichen, transportiert *Shigella* Effektorproteine über das T3SS direkt in das Wirtszellcytosol. Obwohl viele Fortschritte im Verständnis über den Aufbau des T3SS erzielt wurden [2-4], ist nur wenig über die molekularen Mechanismen bekannt, welche die Effektorsekretion ermöglichen.

In dieser Studie werden die Struktur des periplasmatischen Innermembranringes und des Konnektors des *Shigella* T3SS, in Abwesenheit von Effektoren (Apo) und mit einem Effektor im T3SS untersucht. Drei Proteine, MxiG, MxiJ und MxiD, bilden den Innermembranring (MxiG und MxiJ) und den Konnektor (MxiD) und ihr Aufbau war bis jetzt unbekannt. Um die Struktur des T3SS während des Effektortransportes zu analysieren, wurde ein Effektorfusionsprotein benutzt [5]. Die Struktur des Innermembranrings und des Konnektors basieren auf Kryoelektronenmikroskopiedaten und konnten jeweils bis zu einer Auflösung von 3.6 Å und 3.9 Å für das Apo T3SS und 4.0 Å und 4.2 Å für das T3SS mit einem Effektor gelöst werden. Der Innermembranring fällt durch einen symmetrischen Aufbau von jeweils 24 Untereinheiten von MxiG und MxiJ auf. Kanäle mit einem negativen elektrostatischen Potential durchziehen den Innermembranring und verbinden das Periplasma mit dem bakteriellen Zytosol. Eine sequenzkonservierte Region in MxiG konnte identifiziert werden, welche für die Effektorsekretion, die strukturelle Integrität des Nadelkomplexes und die Wirtszellinvasivität eine wichtige Rolle spielt. Hierfür wurden Ein-Punkt-Mutationen durchgeführt und mittels biologischer und biochemischer Assays analysiert.

Die Verbindung zwischen dem Innermembranring und dem Ring des T3SS, welcher sich an der äußeren Membran anlagert, konnte für *Shigella* zum ersten Mal gezeigt werden; seine Struktur ist sonst nur in *Salmonella* bekannt [2]. Der Konnektor ist gekennzeichnet durch 16 symmetrische MxiD Untereinheiten die einen Ring bilden, während der Rest des äußeren Membranringes durch eine 15-fache Symmetrie gekennzeichnet ist. Die Positionen der  $\alpha$ -C-Atome des Innermembranringes und des Konnektors sind in der Apo-variante und im T3SS mit Effektorfusionsprotein sehr ähnlich.

# Abstract

*Shigella Flexneri* is a gram-negative bacterium that infects the human intestine, using the type three secretion system. Type three secretion systems (T3SS) are membrane-embedded transporters essential for the survival of gram-negative pathogens in the hosts and a continual infection. The T3SS enables *Shigella* delivery of effector proteins directly to the host cell cytosol, promoting the infection process. A prominent feature of the T3SS is the basal body, consisting of an inner and outer membrane ring, encompassing a central needle and a rod [1, 6]. The basal body in combination with the export apparatus core is entitled needle complex and can be purified from the membrane. Despite the remarkable advances and insights into the architecture of the needle complex [2-4], little is known about the molecular mechanisms underlying effector secretion.

In this study I will discuss the structure of the periplasmic inner membrane ring (IM ring) and the connector of the *Shigella* T3SS, in the apo state and in the light of effector transport. Three proteins, MxiG, MxiJ and MxiD, constitute the inner membrane ring and the connector their architecture was not known to-date. To analyze the structure of the T3SS upon effector transport, T3SS trapped with an effector fusion protein were used [5]. The IM ring and the connector derive from cryo-electron microscopy maps and could be solved at resolutions of at 3.6 Å and 3.9 Å for the apo structure, and 4.0 Å and 4.2 Å trapped with an effector, respectively.

The inner membrane ring adopts a 24-fold rotational symmetry and shows an extensive polar channel system connecting the bacterial periplasm with the cytosol. A conserved area in MxiG is essential for effector secretion, needle complex stability and invasiveness, as proven by site-directed mutagenesis in combination with biological and biochemical assays.

The inner membrane ring and the outer membrane ring are connected by  $\beta$ -sheet augmentation, which could be shown for the first time in *Shigella*. The connector adopts a 16-fold symmetry while the outer membrane ring adopts a 15-fold symmetry. Apparently, the protein backbone of the inner membrane ring and the connector are very similar in the apo and effector trapped state.

# Contents

<b>Zusammenfassung</b> .....	<b>V</b>
<b>Abstract</b> .....	<b>VII</b>
<b>Contents</b> .....	<b>VIII</b>
<b>Abbreviations</b> .....	<b>XI</b>
<b>1 Introduction</b> .....	<b>1</b>
1.1 The human pathogen <i>Shigella</i> .....	1
1.2 Bacterial secretion systems .....	3
1.3 Structure of the T3SS .....	4
1.4 T3SS activation and assembly .....	5
1.5 Proteins constituting the base of the T3SS needle complex .....	7
1.5.1 The inner membrane ring protein MxiG .....	7
1.5.2 The inner membrane ring lipoprotein MxiJ .....	7
1.5.3 The outer membrane ring protein MxiD .....	8
1.6 Needle complexes trapped with an effector .....	8
1.7 Aim of this study .....	9
<b>2 Results</b> .....	<b>Fehler! Textmarke nicht definiert.11</b>
2.1 Isolation of needle complexes .....	11
2.1.1 Optimization of the needle complex isolation .....	11
2.1.2 Obtaining top views of needle complexes .....	14
2.2 Structure of the periplasmic inner membrane ring .....	19
2.2.1 A ring building motif is present in MxiG and MxiJ .....	20
2.3 Interactions within the periplasmic inner membrane ring .....	23
2.3.1 MxiG-MxiG interaction is mediated by polar contacts .....	23
2.3.2 The inner membrane ring is channelled .....	24
2.3.3 Mutational analysis of conserved channel residues .....	26
2.3.4 The MxiG and MxiJ interface possess polar contacts .....	32
2.3.5 MxiJ subunits are connected by polar and hydrophobic interactions .....	34
2.4 The IM ring is connected to the OM ring via $\beta$ -sheet augmentation .....	38
2.4.1 The 15- and 16-fold symmetry in the secretin and connector region .....	38
2.4.2 A RBM is present in the N1 domain of MxiD <sub>34-171</sub> .....	40
2.4.3 MxiD and MxiG $\beta$ -sheet augmentation is essential for needle formation .....	41
2.5 MxiD <sub>34-171</sub> inter- and intramolecular interaction .....	44
2.5.1 The N0-N1 interface is stabilized by hydrophobic and polar interactions .....	44
2.5.2 The N1 domain mediates MxiD <sub>34-171</sub> intermolecular interaction .....	44
2.5.3 The connectors of <i>Shigella</i> and <i>Salmonella</i> comprise similar dimensions .....	47

2.6	The apo and the trapped needle complex basal body in comparison .....	49
2.6.1	Global differences in the dimensions of apo and effector trapped needle complex.....	50
2.6.2	Density differences in the needle lumen and the export apparatus core.....	52
2.6.3	Minor changes in the MxiG D2 $\beta$ -sheet and the MxiJ loops facing the export apparatus ..	56
2.6.4	The structures of the connectors and their interactions are very similar .....	59
2.7	Validation of the atomic models .....	61
<b>3</b>	<b>Discussion and perspectives .....</b>	<b>64</b>
3.1	Symmetries and dimensions of the <i>Shigella</i> T3SS in comparison to other T3SS .....	65
3.2	Outer membrane and inner membrane ring interact via $\beta$ -sheet augmentation .....	66
3.3	Symmetry mismatch of connector and the outer membrane ring .....	66
3.4	IM ring stability and assembly.....	68
3.5	PMF dependent effector transport .....	69
3.6	Structural changes in the basal body upon effector transport .....	71
<b>4</b>	<b>Materials and methods .....</b>	<b>72</b>
4.1	Kits, Machinery, Chemicals and consumables .....	72
4.2	Buffer solutions .....	76
4.3	Bacteria & DNA .....	79
4.4	Enzymes .....	82
4.5	Cellular Methods .....	83
4.5.1	General cell culture.....	83
4.5.2	Gentamicin protection assay .....	83
4.6	Molecular Methods .....	84
4.6.1	Polymerase Chain Reaction (PCR).....	84
4.6.2	Quickchange Site-Directed Mutagenesis.....	84
4.6.3	Colony PCR .....	86
4.6.4	Agarose gel electrophoresis.....	86
4.6.5	Conventional cloning .....	86
4.7	Microbiological & Biochemical Methods .....	88
4.7.1	Bacterial culture.....	88
4.7.2	Adaptation to minimal medium.....	88
4.7.3	Electro-competent cells.....	89
4.7.4	Transformation of bacteria .....	89
4.7.5	Secretion assay .....	90
4.7.6	Sodium dodecylsulfate polyacrylamide gel electrophoresis (SDS-PAGE) .....	90
4.7.7	Western blotting .....	91
4.7.8	Expression test.....	91
4.7.9	Expression and purification of needle complexes .....	92
4.7.10	Immunofluorescence imaging .....	93
4.8	Negative staining and cryo-EM .....	94

4.8.1	Grid preparation.....	94
4.8.2	Negative staining and transmission electron microscopy (TEM) .....	94
4.8.3	cryogenic electron microscopy (cryo-EM) data collection.....	94
4.8.4	Single particle-analysis .....	95
4.9	Model building, structure refinement and analysis.....	96
4.9.1	Model building .....	96
4.9.2	Structure validation .....	97
4.9.3	Structural analysis .....	98
	<b>References.....</b>	<b>100</b>
	<b>Attachment .....</b>	<b>107</b>
	<b>List of tables .....</b>	<b>109</b>
	<b>List of figures.....</b>	<b>110</b>
	<b>Acknowledgement.....</b>	<b>112</b>
	<b>Eidesstattliche Versicherung*:</b> .....	<b>113</b>

# Abbreviations

Abbreviation	explanation
°C	Degree Celsius
µg	Microgram
µl	Microliter
µm	Micrometer
µM	micromolar concentration
Å	Ångström
AHT	Anhydrotetracycline
APS	Ammoniumpersulfate
AU	Absorption units
bp	Base pairs
BSA	Bovine serum albumin
CFU	Colony forming units
COOH	Carboxy-terminus
C-terminus	Carboxy-terminus
Da	Dalton
ddH <sub>2</sub> O	Double distilled water
ddNTP	2',3'-Dideoxynukleosidtriphosphat
DMEM	Dulbecco's Modified Eagle's Medium
DMSO	Dimethylsulfoxid
DNA	Desoxyribonucleic acid
dNTP	Desoxyribonukleosidtriphosphat
dsDNA	Double stranded DNA
<i>E. coli</i>	Escherichia coli
EDTA	Ethylendiamintetraacetate
<i>et al.</i>	et alia, lat.
EtBr	Ethidiumbromide
for	forward
FSC	Fetal cow serum
g	Gram
h	Hour(s)
HCl	Hydrochloric acid
kcal	Kilocalories
kDa	Kilodalton
kpb	Kilo base pairs
kV	Kilovolt
l	Liter
LB	Lysogeny broth
M	Molar
MDa	Megadalton
mF	Millifarad
mg	Milligram
Milli-Q-water	Nuclease and protease free purified water
min	Minutes
ml	Milliliter
mM	Millimolar concentration
mol	Avogadro number
MW	Molecular weight
NaOH	Sodium hydroxide
NC	Type three secretion system needle complex

nm	Nanometer
N-terminus	Amino-terminus
OD	Optical density
PAGE	Polyacrylamide gel electrophoresis
PBS	Phosphate buffered saline
PCR	Polymerase chain reaction
pH	Potentia Hydrogenii, lat.
pI	Isoelectric point
PTA	Phosphotungstic acid
rcf	Radial centrifugational force
RT	Room temperature
rvs	reverse
SDS	Sodium dodecyl sulphate
sec.	Second
spp.	Species
T3SS	Type three secretion system
TEM	Transmission electron microscopy
TSB	Tryptic soy broth
u	Units
v/v	Volume / volume
w/v	Weight / volume
wt	Wild type
X-ray	Roentgen rays
Ω	Ohm

Amino acid	Three letter code	One letter code
Glycine	Gly	G
Proline	Pro	P
Alanine	Ala	A
Valine	Val	V
Leucine	Leu	L
Isoleucine	Ile	I
Methionine	Met	M
Cysteine	Cys	C
Phenylalanine	Phe	F
Tryptophane	Trp	W
Histidine	His	H
Lysine	Lys	K
Arginine	Arg	R
Glutamine	Gln	Q
Asparagine	Asn	N
Glutamic acid	Glu	E
Aspartic acid	Asp	D
Serine	Ser	S
Threonine	Thr	T
Thyrosine	Tyr	Y

# 1 Introduction

Diarrhoeal diseases, lead to 2.2 million death humans [7] and are the second leading cause of post neonatal child mortality in the world (WHO, 2017) [8]. *Shigella* is a gram-negative enterobacterium evoking Shigellosis and has common ancestors with the human pathogens *E.coli*, *Salmonella*, *Virbrio cholera* and *Pseudomonas*, and the plant pathogens *Erwinia* spp and *Pseudomonas syringae*. The mentioned bacteria use the Type three secretion system (T3SS) to promote infection.

## 1.1 The human pathogen *Shigella*

*Shigella* is facultative anaerobic, rod-shaped and not able to form spores, though considered a remarkably infectious pathogen [9, 10]. An amount of 10-100 bacteria was found to be sufficient to cause an infection of the host [9, 10]. To-date, still no efficacious vaccine is available [11].

Up-taken by contaminated food or water, *Shigella flexneri* traverses the human gut. Two pathways for the uptake were suggested so far, both dependent on the T3SS. One pathway suggests the direct invasion through the intestinal epithelial cell layer through finger-like protrusions called filpodia [12]. The alternative pathway is a bit more complex. After transcytosis though the M cells, located in the Payer's patches, *Shigella* escapes the macrophage and enters the epithelial cells from the basolateral side utilizing a first set of effectors, secreted by the T3SS (Figure 1). Pro-inflammatory interleukins released from the epithelial cells and pyroptotic macrophages lead to chemotactic recruitment of neutrophils and natural killer cells. Neutrophils that migrate to the basolateral side contribute to destabilization of the epithelial cell layer, also facilitating entrance of *Shigella* to the basolateral side. After invasion of the host cell epithelium, *Shigella* escapes the host cell vacuole and spreads from one cell to another, using a rearrangement of the host cell actin filaments known as "comet-like tails" [13]. To escape the host cell vacuole, another set of effectors is secreted, proteins promoting the infection process and suppressing host cell defense.

## 1 Introduction

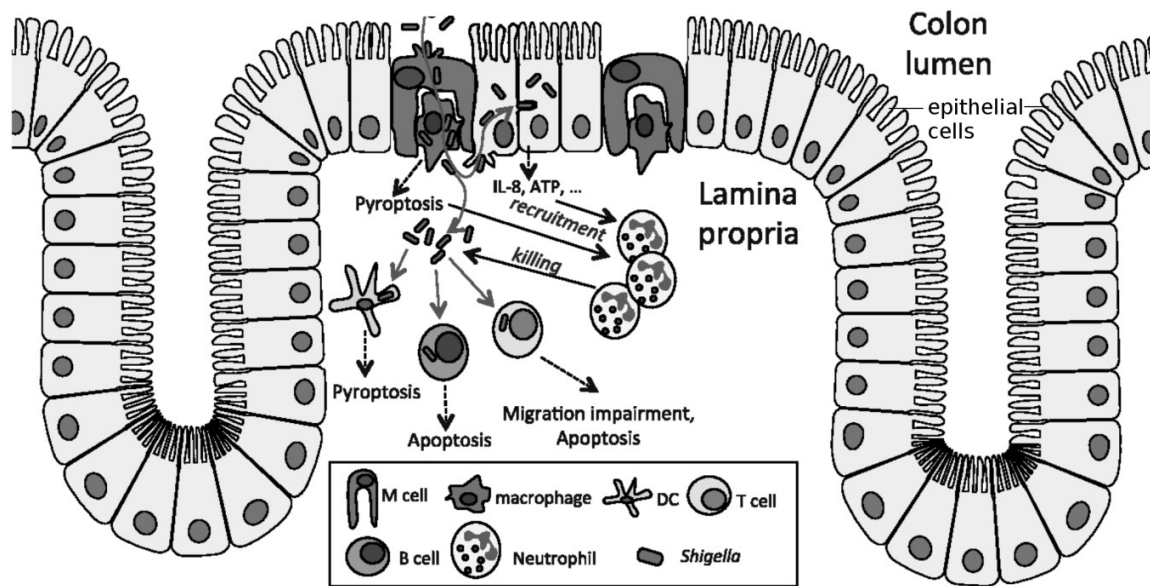


Figure 1: *Shigella* pathogenesis. The release of interleukin-(IL) 8 from epithelial cells in addition to IL-1 $\beta$  and IL-18 released by pyroptotic macrophages recruits neutrophil leukocytes, fostering inflammation. Transmigration of neutrophils to the luminal side contributes to the destabilization of the epithelial barrier and facilitates bacterial translocation to the Lamina propria. Figure adapted from [12]

The type three secretion system, which is used to deliver effectors to the host cell membrane, is a macromolecular transport complex of 3.5 MDa, embedded in both bacterial membranes. The T3SS shares genetic ancestors with the bacterial flagellum, another bacterial secretion system.

## 1.2 Bacterial secretion systems

Simple translocation systems that transfer proteins across the inner membrane in the bacterial periplasm are the general secretion (sec), or the tat secretion pathway. In the sec-pathway, a cleavage N-terminal signal sequence of the nascent polypeptide is recognized by the chaperone SecB and targeted to the heterotrimeric transmembrane channel complex SecYEG. The N-terminus of the polypeptide chain is translocated to the periplasm using ATP-Hydrolysis. Signal peptidases cleave off the N-terminal signal sequence and release the protein into the periplasmic space [14]. In the signal recognition particle (SRP) pathway, the transmembrane region of the nascent protein is bound by the SRP which guides the complex to the SecYEG channel, where it is translocated into the periplasm [15]. In contrast to the sec-dependent pathway, the transmembrane region recognized by the SRP is not cleaved off after translocation, but remains in the membrane.

More sophisticated translocation systems allow transport of proteins out of the gram-negative bacterial cell into exterior space. The Type I – VI secretion systems transport specific sets of proteins and comprise a  $\beta$ -barrel channel anchored to the outer membrane called secretin. Similar to the T3SS, the Type II secretion system harbour an inner membrane ring and an outer membrane ring, which are connected [16]. Though, the secretion process differs from the T3SS: Type II effectors are translocated to the periplasm via the sec-dependant pathway. Binding of periplasmic effectors to the inner membrane ring or secretin domain initiates pseudopilus guided and ATP-hydrolysis fuelled translocation to the extracellular side [17].

The phylogenetic relation of the T3SS to the flagellum is revealed in their structural similarity in the export apparatus (1.3 Structure of the T3SS). Other components as for instance the basal body are less conserved [18]. Instead of the secretin  $\beta$ -barrel that reaches from the outer membrane to the periplasm, flagella have two ring systems to bridge that space and connect with the inner membrane ring. In *Shigella*, the inner membrane ring is smaller than the respective flagellar component [18]. Since the T3SS is used for secretion of effectors and the flagellum for motion, the flagellar system translocates structural components instead, which assemble to the extracellular filament. T3SS orthologues of the stator proteins MotB and MotA, conducting flagellar rotation, have not yet been discovered [18].

### 1.3 Structure of the T3SS

Approximately 30 genes of *Shigella* contribute to the T3SS and the majority of them is carried in a ~ 230 bp plasmid, called virulence plasmid [19]. The virulence plasmid is organized in several operons, the *mxi* (membrane expression of invasion plasmid antigens) and *spa* (surface presentation of antigens) operons coding for ~ 20 structural proteins while genes in the *ipa* (invasion plasmid antigens) operon encode effectors [20].

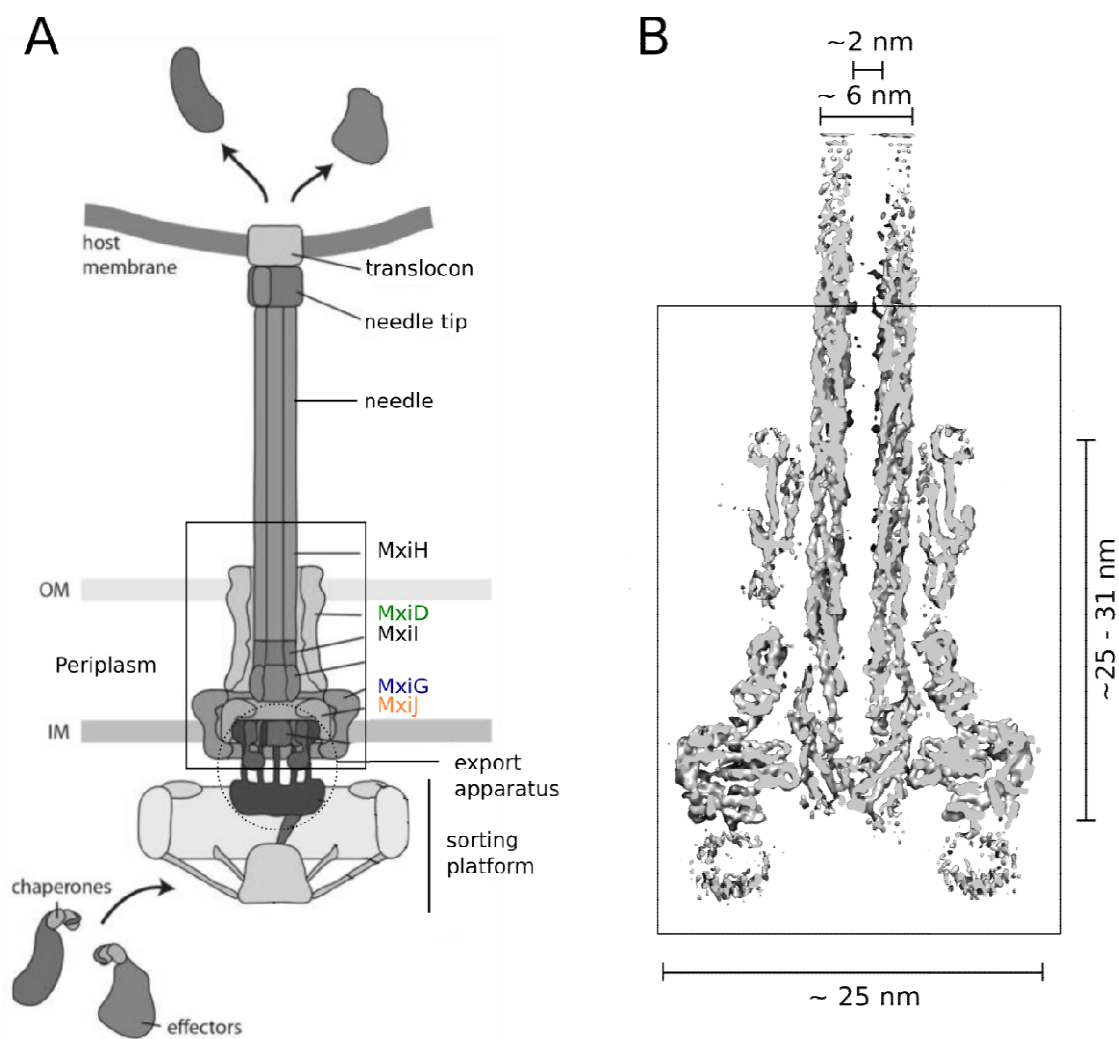


Figure 2: Overview on the T3SS architecture. A) Schematic representation of the T3SS; the export apparatus and cytoplasmic sorting platform are labelled, OM – outer membrane, IM – inner membrane. The proteins forming the basal body, MxiD, MxiG and MxiJ, are highlighted in colour. The region of the needle complex is boxed. Figure adapted from [1]. B) Central slice of a purified *Shigella* needle complex, reconstructed with single particle analysis from a cryo-EM dataset. The approximate dimensions of the basal body and the needle are indicated.

The T3SS consists of several components. The inner and outer membrane ring (IM and OM ring, respectively) integrate in their respective membrane (Figure 2). The inner membrane ring is composed of two concentric rings, formed by two proteins, MxiG and MxiJ. MxiD forms the secretin barrel and the connector. The assembly of MxiD, MxiG and MxiJ together with the embedded hollow needle and inner rod is called basal body [6]. The needle is connected at the proximal end via the inner rod to the export apparatus.

The export apparatus consists of several proteins, SpaPQRS and MxiA [21], and reaches from the bacterial periplasm to the cytosol. The export apparatus interacts in the bacterial cytosol with the sorting platform, to which effectors can bind. Chaperons are released from effectors after binding to the sorting platform and the stripped effectors are transported with their N-terminus first through the export apparatus, the rod and the needle to the host cell. The entity of basal body, inner rod, needle, export apparatus, sorting platform, effectors and their chaperones are called type three secretion system [22].

#### 1.4 T3SS activation and assembly

Transcription regulators of T3SS structure genes and effectors belong to the AraC protein family and bind DNA by conserved helix-loop-helix motives [23]. In *Shigella*, VirF is considered the master regulator of the gene *virBs* [24, 25]. At 37°C, the temperature in the human gut, a transcription repressor is released from the *virF* promoter of *Shigella flexneri*, facilitating the VirF expression and subsequent activation of genes responsible for T3 formation (*mxi* and *spa* operons), activation and effector release [26]. Other factors identified for inducing T3 gene expression are low Ca<sup>2+</sup> concentration in *Pseudomonas* and medium osmolarity and pH in *Salmonella* [27].

Formation of the basal body was considered the initial step of T3SS assembly [28]. Two models exist to-date: the Outside-in and the Inside-out model which differ in whether the outer membrane ring or the inner membrane ring are required in early stages of T3 assembly and the activity of a periplasmic peptidoglycan-cleaving enzyme, required for secretin barrel assembly [29].

Fluorescent *in vivo* experiments in *Yersinia* suggest that the outer membrane ring assembles first via the sec-dependent pathway [28]. For *Salmonella*, the inside-out model was suggested [2, 4, 30], based on heterologous overexpressed proteins.

## 1 Introduction

In *Shigella*, the outer membrane ring and the connector are formed by MxiD, a protein belonging to the family of secretins, which are also present in T2SS and T3 pili [31]. Co-expression studies suggested the inner membrane ring component MxiJ stabilizes the MxiD ring; Though, the result has to be taken with caution since the interaction was observed in the absence of the MxiD pilotin [32]. The N-terminus of MxiD reaches deep into the periplasm and was shown to bind the C-terminus of the inner membrane ring protein MxiG, in the respective *Yersinia* orthologues [33] and recently also for *Salmonella* [2]. Co-Immunoprecipitation studies and fluorescent experiments in *Yersinia* implied that the presence of the secretin is required for assembly of the MxiG ring [28].

MxiG is associated to the inner membrane [34] and fusion protein studies suggest that translocation of the MxiG C-terminus to the periplasm is dependent on a transmembrane region of MxiG, that could be bound by the Signal recognition particle (SRP) [15]. Like the sec-dependent pathway, the SRP pathway utilizes the SecYEG channel. In contrast to the sec-pathway, the signal sequence is not cleaved off and remains in the inner membrane.

Like MxiD, MxiJ is translocated into the periplasm via the sec-dependent pathway [35]. The *Salmonella* orthologue is suggested to initiate the formation of the IM ring at the export apparatus [4, 36].

In the Outside-in model, the export apparatus and the sorting platform form and attach after the basal body is assembled. Though, the exact time point of their assembly remains unclear. Needle and inner rod would assemble in the last stages of needle complex (NC) formation.

Since the export apparatus represents the focal point of NC assembly in the inside-out model, this component would be present from the very beginning. The export apparatus would be ready to secrete inner rod and needle subunits into the periplasm at earlier stages than in the Outside-in model. Secretion competence is gained, once the sorting platform and the cytoplasmic components of the export apparatus attach. Once the assembly of the T3SS is completed, effectors are secreted dependent on the stage of infection in a hierarchical manner [37].

## 1.5 Proteins constituting the base of the T3SS needle complex

The T3SS basal body spans both bacterial membranes and forms a pore, harbouring the central needle, which is connected at the proximal end via the inner rod to the export apparatus. The three proteins MxiD, MxiG and MxiJ form the outer and inner ring, respectively, and their assembly is referred to as the base [38]. The needle is a helical assembly of MxiH subunits, similar to the inner rod, which is formed by the protein MxiI. The base in combination with the needle and inner rod is the basal body [29]. Including the export apparatus core to the basal body, the complex is referred to as the needle complex [2], which can be purified using an N-terminal tag on the needle protein.

### 1.5.1 The inner membrane ring protein MxiG

MxiG is a 42 kDa protein [34] that possesses an N-terminal transmembrane region from amino acid 127-141 (TMHMM server result) and is less conserved than MxiD and MxiJ. MxiG is 371 amino acids long and in contrast to MxiD and MxiJ, it does not comprise an N-terminal signal sequence. The structure of the cytosolic domain was solved at 1.6 Ångström and pull down studies showed that it interacts with the sorting platform component Spa33 [39]. It shows only low strict sequence conservation with orthologous proteins (Figure 12) and the structure of the periplasmic domains was lacking.

### 1.5.2 The inner membrane ring lipoprotein MxiJ

MxiJ is a lipoprotein that possesses an N-terminal sec-signalling sequence (amino acid 1-17) [35] and comprises 241 residues, unprocessed. The LIG-C lipobox motive in the signal sequence is recognized and cleaved between glycine and cysteine by the signal peptidase II [40]. Palmitoylation of the cysteine sulfhydryl group at amino acid 18 anchors the protein to the inner membrane. After processing, the apparent molecular weight of MxiJ is ~ 22 kDa. A C-terminal helix is predicted from 212-231 (TMHMM server result) and the last 9 amino acids proceed into the cytosol. MxiJ is of higher conservation than MxiG (Figure 19) and forms the inner of both IM rings. Like for the periplasmic domains for MxiG, there was no structure of MxiJ available so far.

## 1 Introduction

### 1.5.3 The outer membrane ring protein MxiD

MxiD is a well-conserved outer membrane protein comprising 566 residues and has an apparent molecular weight of 63 kDa. It is inserted into the periplasmic space via the sec-dependent pathway. After cleavage of the sec signal peptide 1-22 by the signal peptidase I, the protein has an apparent MW of 60 kDa. Based on sequence similarities, MxiD belongs to the Gsp D family, which includes secretins from Type II – Type IV secretion systems. After translocation of MxiD over the bacterial inner membrane, the MxiD C-terminus is suggested to bind the pilotin protein MxiM, which guides both proteins via the Lol-pathway to the outer bacterial membrane [32, 41]. Studies in *E.coli* and *Pseudomonas* suggested that the oligomerization of the MxiD subunits to the double layered outer membrane ring might happen independently of the  $\beta$ -barrel assembly machinery (BAM complex), which usually assists formation of  $\beta$ -barrel structures embedded in the outer membrane, as for example OM porins [42, 43]. Atomic structures from various secretins are available; however, the structure of MxiD<sub>34-170</sub> was to-date unknown.

### 1.6 Needle complexes trapped with an effector

Prior to transport, effector proteins are unfolded at the sorting platform and are transported with their N-terminus first through the needle channel [5]. IpaB is forming the translucent pore in the host cell membrane, together with IpaC. Secretion of IpaB, among other Ipa effectors, is co-dependent on IpaD, which is suggested to “plug” in the T3SS in the absence of secretion activation signals [6, 44]. A former member of the Kolbe lab, Dr. Kim Dohlich, designed and tested a construct that traps an effector in the needle lumen. She used the effector protein IpaB fused at the C-terminus with a RNA Methyltransferase (PDB ID 1IPA) from *Thermus thermophilus* (IpaB-knot). The methyltransferase cannot be unfolded by the T3SS [5], hence blocking the needle lumen. Immunogold labelling and TEV protease assay on purified needle complexes showed that IpaB-knot fusion protein is located in the needle lumen. Furthermore, it was shown that IpaB-knot blocks T3SS dependent secretion and impairs invasiveness [5].

## 1.7 Aim of this study

Though high resolution structures of *Salmonella* T3SS and orthologues were solved [2, 45], well-resolved structures of main components of the *Shigella* T3SS were lacking. Of the inner ring protein MxiG, only the cytoplasmic domain was determined by X-ray crystallography [39]. Of MxiD, forming outer membrane ring, only a 19 amino acid stretch of the full-length 566 amino acid long protein was solved by solid state nuclear magnetic resonance (ssNMR) spectroscopy [32]. The structure of MxiJ, contributing to the inner membrane ring, was unknown. Therefore, there was a need for investigation, especially in the light of structural changes upon effector transport.

The goal of this study was to gain insights into the structure of the T3SS needle complex in both states, apo and trapped with an effector, in particular of the inner membrane ring (MxiG and MxiJ) and the outer membrane ring (MxiD).

Traditional structural determination techniques like X-ray crystallography and NMR and are powerful to solve proteins with a molecular weight of ~ 50 kDa, the novel technique of single particle cryo electron microscopy allows the analysis of large (~ 300 - 500 kDa and higher MW) molecules and complexes in a near-atomic range [46]. Especially for detergent solubilised membrane proteins like the T3SS complex, techniques like X-ray crystallography have shown to be difficult. Here, cryo-EM facilitates the reconstruction of the specimen in the near native state. Since the purified sample is flash-frozen, no crystal packing of the protein needs to be fostered. Also, no fixative or contrast enhancer is used. Though, the reduced signal-to-noise ratio of cryo-EM micrographs requires a higher amount of homogenous particles to allow a good reconstruction of the specimen.

Hence, expression and purification of the needle complex was optimized to allow the collection of cryo-EM data sets. To allow near-native conditions during expression, mutant strains of *Shigella flexneri* M90T were used. The needle complex genes were not overexpressed in *E.coli* strains, genetically engineered for protein expression, deficient in certain proteases and allowing the usage T7-promoter regulated pET-vector system.

The near-atomic maps, derived from single particle analysis, allowed building and refinement of the inner membrane ring and the connector. The relevance of identified structural features in the models were validated generating point mutants and testing them for effector secretion, needle complex stability and bacterial invasiveness with biological and biochemical assays.

## 1 Introduction

## 2 Results

### 2.1 Isolation of needle complexes

Structure determination by cryo-electron microscopy (cryo-EM) single-particle analysis requires a highly pure, monodisperse sample of high concentration and homogeneity [46]. Hence optimization trials for the protein expression and the needle complex purification procedure were performed.

#### 2.1.1 Optimization of the needle complex isolation

To purify apo and effector trapped needle complexes from *Shigella*; MxiH was N-terminally Strep-tagged and introduced in *Shigella* M90T  $\Delta ipaD$  strains on an inducible plasmid. In the *Shigella* M90T  $\Delta ipaD$  strain, the gene on the virulence plasmid encoding for the effector IpaD was disrupted by an antibiotic resistance cassette, as described by Datsenko & Wanner, 2000 [47]. The effector IpaD controls, together with IpaB, the blocking of the T3SS in absence of secretion signals [48], resulting in hypersecretory bacteria, if not present. In the apo needle complex strain, in addition to  $\Delta ipaD$ , the gene for MxiH was knocked out, to avoid background expression of untagged needle proteins [47]. All strains used in this study are listed in Table 9: Bacterial strains used in this study. Optimization of needle complex isolation was performed on the apo needle complex strain M90T  $\Delta ipaD \Delta mxiH + strep-Xa-mxiH$  and resulting conditions were successfully applied to the purification of mutant and effector trapped needle complexes described in this study.

## 2 Results

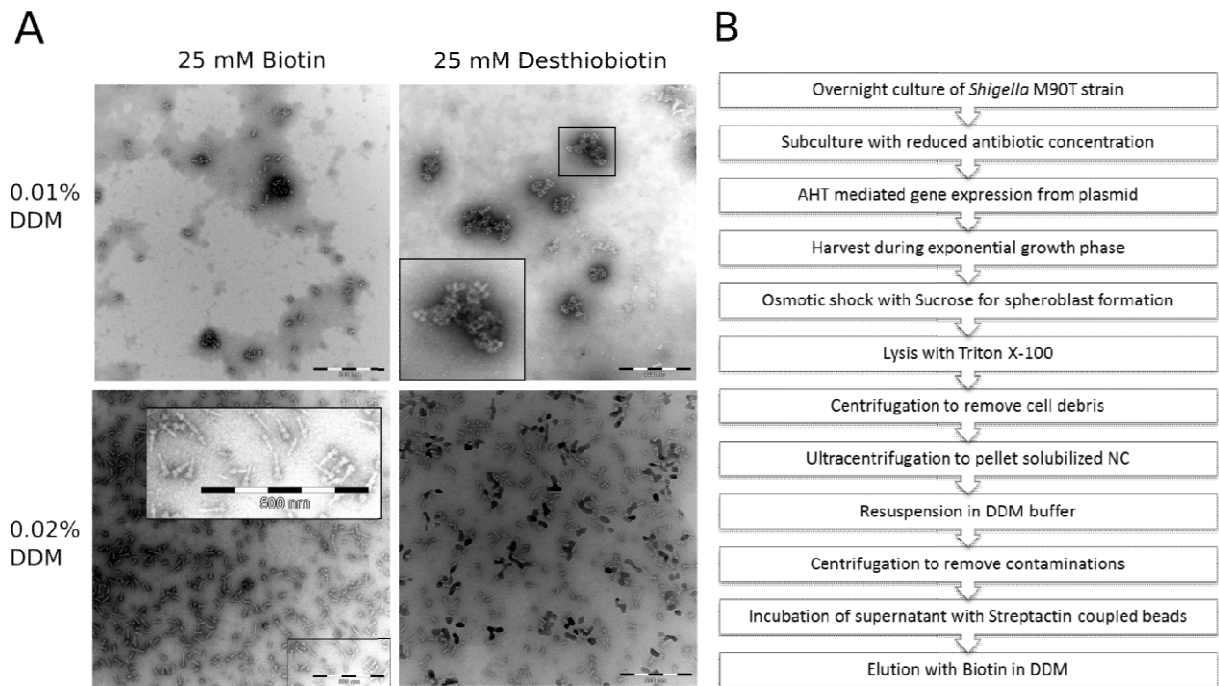


Figure 3: Optimization of the elution buffer composition for needle complex isolation. A) TEM images of PTA stained isolated needle complexes, isolated at different elution conditions. The areas depicted are representative for the purification performed with the respective elution buffer. Magnified areas are boxed. Using 0.02% DDM detergent and 25 mM Biotin allowed isolation of needle complexes while other conditions led to less and/or aggregated particles. B) Key steps of the optimized T3SS needle complex purification protocol

Varying the detergent and eluent concentrations, the elution buffer composition could be optimized, resulting in intact, detergent solubilised needle complexes (Figure 3). The homogeneously resuspended bacterial lysates were split and applied in equal volumes to the resin and eluted in equal volumes (Figure 3A). Elutions performed with 25 mM Biotin in 0.02 % w/v n-Dodecyl  $\beta$ -D-maltoside (DDM) showed a higher concentration of needles than elutions performed in the respective buffer with 25 mM Desthiobiotin. Lowering the concentration of detergent to from 0.02% to 0.01% w/v DDM resulted in aggregated needle complexes for Biotin and Desthiobiotin. Since the dissociation constant  $K_d$  of Biotin to Streptavidin is  $10^4$  lower than the  $K_d$  of Streptavidin ( $K_d$  of  $\sim 10^{-14}$  M compared to  $\sim 10^{-10}$  M) [49], biotin can in theory release more needle complexes from the resin. At detergent concentrations close to the critical micelle concentration (CMC) of 0.15 - 0.17 mM, the amount of surfactant molecules present in the buffer is not sufficient to solubilise single needle complexes, resulting in aggregation. Therefore, 0.02% w/v DDM was used after the first ultracentrifugation step, to solubilise pelleted needle complexes, and was present till the elution. The concentration of Biotin was 25 mM in the elution buffer. Furthermore,

increasing the buffer capacity to 500 mM TRIS, pH 8.0 helped to solve Biotin, which reacts acidic in aqueous solutions. Since decreasing the pH results in decreased binding affinity of Biotin to Streptavidin [50], it is essential to keep the pH above 4 to allow displacement of Strep-tagged proteins by Biotin molecules.

A schematic overview on key steps of the optimized purification protocol is depicted in Figure 3B and a detailed description is given in the material and methods section.

Adopting strains to minimal medium, which is a technique used in experimental evolution [51], was utilized to increase the protein expression and subsequently the concentration of purified needle complexes. It was successfully performed for the *Shigella* M90T strain with IpaB-knot trapped in the needle lumen of the T3SS (*M90T ΔipaD ipaB::rrmA + strep-Xa-mxiH*). To apply selective pressure, bacteria were incubated on minimal medium agar plates supplemented with 1 mM amino acids (M9+AA) with increasing antibiotic concentrations over cultivating time (4.7.2 Adaptation to minimal medium).

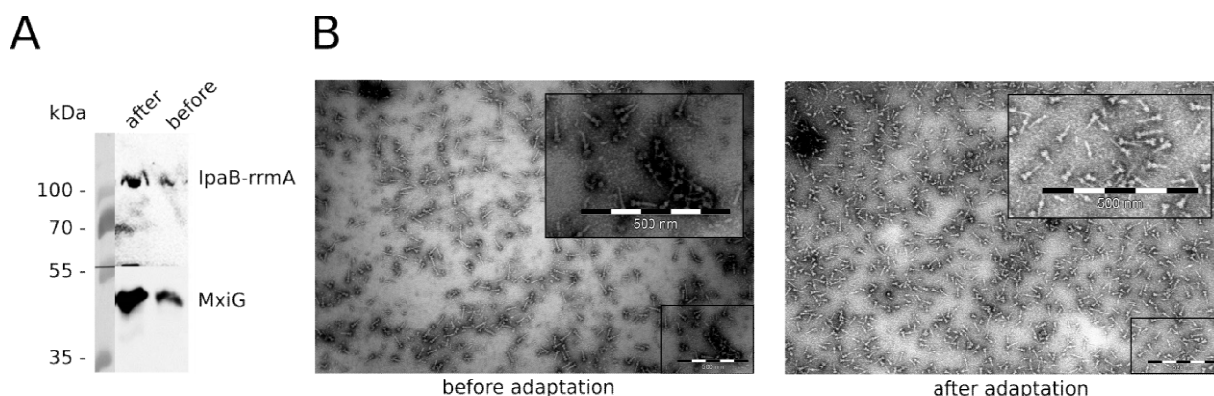


Figure 4: Adaptation of the trapped needle complex strain to minimal medium increased the relative needle complex amount that can be isolated. *M90T ΔipaD ipaB::knot + strep-Xa-mxiH* before and after adaptation to minimal medium are depicted here. A) Western Blot of bacteria lysates, harvested 5 hours past inoculation. The samples were normalized on cell density and equal volumes were applied on the SDS-PAGE gel. Antibodies against IpaB and MxiG were used and the respective proteins are indicated. The molecular weight standard is depicted on the left side. C) TEM images of PTA - stained isolated needle complexes before and after adaptation. The images are representative for each sample.

Adaptation to minimal medium resulted in slightly higher expression levels of the needle complex proteins IpaB-knot and MxiG (Figure 4A) in western blotting of samples normalized on cell density. Also isolating the needle complexes and in transmission electron microscopy (TEM) imaging, the approximate relative density of needle complex was higher than before adaptation (Figure 4B, representative image).

## 2 Results

Initial experiments measuring the growth rates in minimal and rich medium of the strain showed similar growth rates before and after adaptation to minimal medium. Applying the adaptation procedure to other strains did either not increase the needle complex amount that could be purified or they did not grow on minimal medium plates. The addition of supplements as for instance trace metals to the medium upon expression and usage of different media was tested and did not result in increased needle complex density.

Concentrating the needle complexes by lyophilisation caused severe damage (aggregation, degradation) to the needle complexes. Though, ultracentrifugation up to 200.000 rcf for 2 hours seems to not impair the needle complex assembly.

Hence, apo needle complexes were purified from *S. flexneri*  $\Delta ipaD \Delta mxiH$  + *strep-Xa-mxiH* and effector trapped needle complexes derived from *S. flexneri*  $\Delta ipaD ipaB::rrmA$  + *step-Xa-mxiH*, adapted to minimal medium and purified using the improved protocol. Quality and quantity of the isolated needle complexes was evaluated with phosphotungstic acid (PTA) negative staining and TEM imaging (described in chapter 4.8 **Negative staining and cryo-EM**) before collecting the cryo-EM data sets.

The structure of the apo needle complex will be discussed in the chapters 2.2 – 2.5 while structural differences between the apo and trapped state of the needle complex will be analysed in chapter 2.6 **The apo and the trapped needle complex basal body in comparison.**

### 2.1.2 Obtaining top views of needle complexes

Having different orientations of the particles on the grid is useful to obtain good 3D reconstructions of the specimen [52]. Options to obtain different orientations are either to tilt the grid upon dataset recording or to orient the sample in different positions on the grid.

As described by Schraidt *et al.* [53], the N-terminal His-tagged MxiG orthologue can be used to obtain top views of vitrified needle complexes on the cryo-EM grids [53]. Lowering the pH to 5.5 results in protonation of the side chain amine group of the His-tag and should allow attachment of the inner membrane ring to the carbon coated surface of the grids, which was charged by plasma cleaning. The

needle complex would then be oriented vertically on the grid. Since pH 5.5 is a rather harsh condition that might induce damage of the needle complex, we aimed to work at pH 8.0 and introduced a Strep-tag to the N-terminus of MxiG. A Strep-tag could function in a similar fashion: the theoretical pI of the Strep-tag II (WSHPQFEK) is 6.75 while a 6xHis tag is 7.21 (ExpPASy ProtParam, 30.09.2019). In addition, an N-terminal His-tag was cloned to MxiG. pH 8 was tested for Strep-MxiG and pH 5.5 and 8.0 were tested for His-MxiG.

The N-terminal tags were introduced by classical cloning, as shown in the following example for His-MxiG. A polymerase chain reaction (PCR) with the nucleotide coded His-tag included as an overhang in the fwd primer (Table 11: Oligonucleotides used in this study) was performed to amplify the gen from a plasmid. The expected product size of ~1160 bp was detected by agarose gel electrophoresis (Figure 5). The purified PCR construct was introduced in the pASK5C backbone by restriction digest with Nco1 and Nhe1, followed by ligation and transformation (see chapter 4.6.5 Conventional cloning) in *E. coli* DH5 $\alpha$ . A colony PCR was performed to select clones for sequencing. The pASK5C\_*His-mxiG* plasmid encodes from 5' to 3' for the 6xHis-tag, followed by a four amino acid factor Xa cleavage site and the full-length MxiG protein. The gene is under the control of an AHT-inducible tet-promoter (Figure 5B).

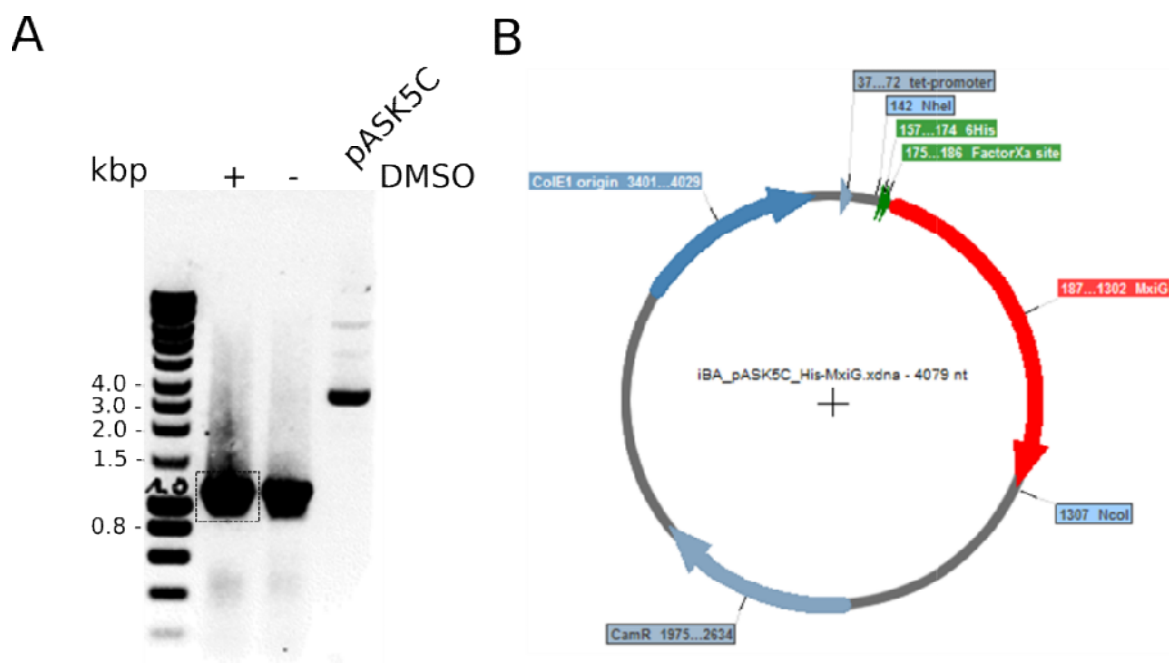


Figure 5: Cloning of *His-mxiG* into pASK5C. A) Agarose gel electrophoresis of *His-mxiG* PCR. The DNA marker range is on the left side is given in kilo base pairs. The dotted box indicates the gel region that was used for purification and digest of the PCR product. The empty target vector pASK5C is loaded in the very right lane. With and without addition of 3% DMSO, the PCR

## 2 Results

resulted in the expected product size of ~1160 kpb. B) Map of *His-mxiG* in pASK5C. Restriction sites used, resistance, gene and promoter are indicated.

*His-mxiG* was expressed in *Shigella* M90T  $\Delta ipaD \Delta mxiG$  + *strep-Xa-mxiH* and in M90T  $\Delta mxiH$  + *strep-Xa-mxiH* (Figure 6A) and the protein concentration of His-MxiG was tested with a western blot. The band visible at ~ 35 kDa can be assigned to His-MxiG. To decipher the expression levels of endogenous expressed *mxiG*, an anti-His and an anti-MxiG antibody were used. The expression of *his-mxiG* seemed to be lower in the  $\Delta mxiH$  strain than in the  $\Delta ipaD \Delta mxiG$  double knockout strain. To check for the structural integrity of the needle complex and the approximate density, needle complexes were isolated using the Strep-tag of the MxiH. Indeed, at pH 8.0 the needle complexes isolated from  $\Delta ipaD \Delta mxiG$  seem to be more stable than at pH 5.5, which fostered needle aggregation and disassembly (Figure 6B). The tubular arrangements visible at pH 5.5 show a similar diameter as the tubes formed by the MxiJ orthologue PrgK<sub>82-200</sub>, suggesting that they could consist of inner membrane ring components or could be an artefact induced by the PTA negative stain [54]. Nevertheless, the amount of needle complex top views was not very high at both pH applied for this strain.

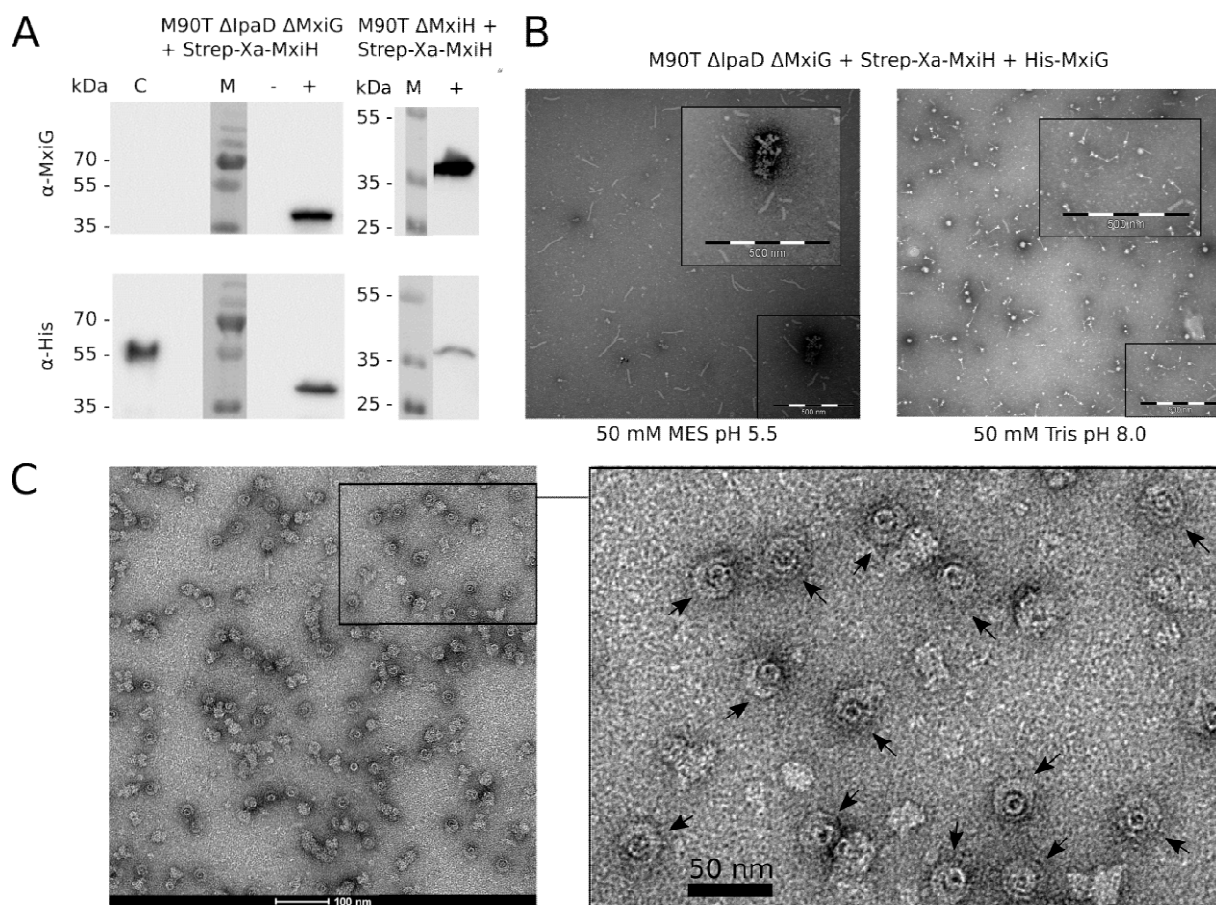


Figure 6: Fostering vertical orientation of needle complexes on the EM grid testing an N-terminal His- and Strep-tag on MxiG A) Western blot of whole cell lysates of His-MxiG in the respective genetic background indicated. Gene expression was induced with AHT ('-' before, '+' after) and samples normalized on cell density. Equal volumes were loaded on the SDS-PAGEs and stained with the respective antibodies, indicated at the left side. The same samples were loaded on the two blots. C is a His-tagged protein of 55kDa, used as an antibody control. M is the molecular weight marker. B) Needle complex purification of M90T  $\Delta$ mxiG + *Strep-Xa-mxiH* + *His-mxiG*. TEM image of negatively stained samples of the same purification eluted in different elution buffers. Needle complexes could be purified at pH 8.0 but in MES buffer at pH 5.5, degradation and aggregation is visible. C) TEM Micrographs of isolated and negatively stained needle complexes purified from *Shigella* M90T  $\Delta$ mxiG + *Strep-Xa-MxiG*. The dimensions are given in the image; top views are indicated with arrows. An N-terminal Strep-tag on MxiG allowed vertical orientation of the needle complexes on the grid.

Though, needle complexes with a Strep-tag on the MxiG N-terminus in a pH 8.0 buffer oriented in a vertical position on the grid and were present in higher density (Figure 6C).

An N-terminal Strep-tag on two proteins, MxiG and the needle protein MxiH time did not enforce a vertical orientation of needle complexes on the grid, horizontal orientations were present in a higher number in comparison to vertical orientations on the grid (data not shown), maybe due to the higher number of Strep-tags present on the needle than on the inner membrane ring. Overall, the Strep-tag on MxiG seems to work better than the His-tag for obtaining top views and might therefore be applied for future structural analysis using cryo-EM.

## 2 Results

## 2.2 Structure of the periplasmic inner membrane ring

As described in the introduction, the periplasmic inner membrane ring of the *Shigella* T3SS is formed by two proteins, MxiG and MxiJ.

The 42 kDa protein MxiG is 371 amino acids long and comprises an N-terminal cytoplasmic region, connected to the periplasmic domains by a transmembrane region (see Figure 7) [34]. The periplasmic domains are well resolved in the focussed 3D reconstruction to a resolution up to 3.2 Å [55]. The inner membrane ring model of MxiG is based on the homologues PrgH structure (PDB ID 3GR0), solved at 2.3 Å with X-ray crystallography, as described in chapter 4.9.1 Model building. The C-terminal MxiG region, comprising amino acid 340-367, was built in the focussed 3D reconstruction of the connector.

The lipoprotein MxiJ has an apparent MW of 25 kDa after cleavage of the N-terminal signal sequence and is anchored to the inner membrane via a palmitoylation site at position C18. The two periplasmic domains, connected by a linker, are followed by a predicted transmembrane region and ~ ten amino acids at the C-terminus face the bacterial cytosol (see Figure 7, Figure 8). The model of MxiJ<sub>21-197</sub> is based on the EM structure (PDB ID 2Y9J) of *Salmonella* PrgK, which share a sequence identity of 52%. The modelling process is described in chapter 4.9.1 Model building and the geometry and cross-correlation data are given in chapter 2.7 Validation of the atomic models.

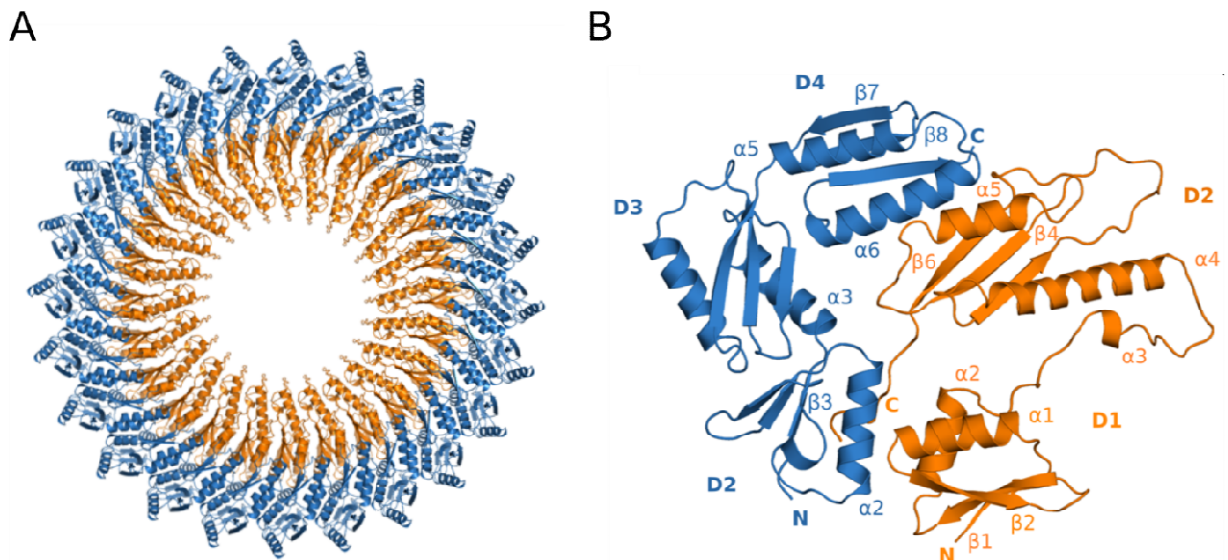


Figure 7: The *Shigella* T3SS inner membrane ring. MxiG<sub>152-367</sub> and MxiJ<sub>21-197</sub> in cartoon representation in blue (MxiG) and orange (MxiJ). A top view is depicted on the left side and a side view one MxiG and one MxiJ subunit on the right side. The secondary structure elements involved in interaction and domains are assigned. This figure is adapted from Lunelli *et al.*[55]

24 subunits of MxiG<sub>152-367</sub> and MxiJ<sub>21-197</sub> respectively form two concentric rings, with MxiG comprising the outer and MxiJ the inner ring (see Figure 7). Both proteins comprise a similar secondary structure topology, the ring-building motif.

### 2.2.1 A ring building motif is present in MxiG and MxiJ

The basal body is formed by a step-wise assembly of the three proteins MxiG, MxiJ and MxiD. A structural feature present in the inner membrane ring and the N1 domain of MxiD was suggested to assist the formation of symmetrical rings: the ring building motif [45].

Three MxiG domains and two of MxiJ form the periplasmic inner membrane ring: the D2, D3 and D4 of MxiG and the D1 and D2 domain of MxiJ (see Figure 7 and Figure 8). All domains of the inner membrane ring have a ring building motif (RBM), which is formed by two tilted  $\alpha$ -helices folded against a three-stranded  $\beta$ -sheet formed by one  $\beta$  strand folding against a two-stranded antiparallel sheet (Figure 8). The RBM is considered a conserved modular fold, present in other proteins forming ring structures, in particular of T3SS basal body proteins [45]. MxiG<sub>152-367</sub> and MxiJ<sub>21-197</sub> align with a Dali-Z-score of  $\sim 19$  to

their respective *Salmonella* orthologues PrgH and PrgK (PDB ID 5TCP), which also comprise ring building motifs (Figure 9A).

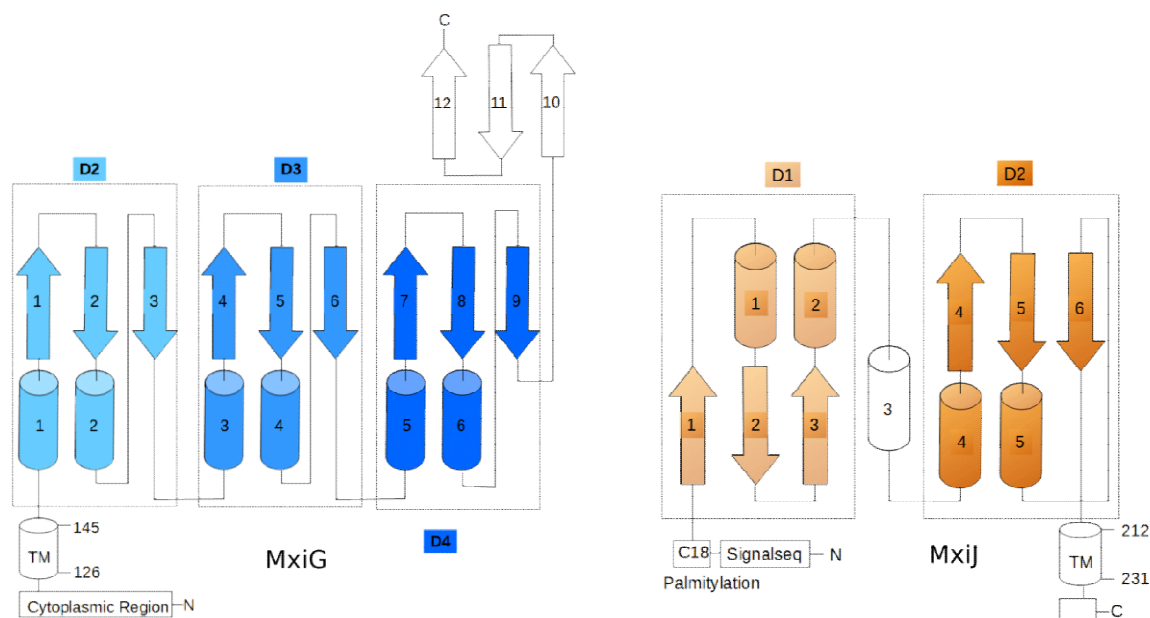


Figure 8: Topology plots of the inner membrane ring proteins MxiG and MxiJ.  $\beta$ -strands are represented by arrows,  $\alpha$ -helices by cylinders and both are numbered according to appearance in the structure. The boxed domains contain ring building motifs, consisting of two helices folded against a three-stranded  $\beta$ -sheet. All domains have an  $\alpha\beta\beta\alpha$  topology, except for the MxiJ D1 domain, comprising an inverted RBM.

Superposing the domains separately, the RMSD in the  $C\alpha$  atoms is between 1.3 and 1.7 for the periplasmic MxiG domains. In the two MxiJ domains, the RMSD is 0.8 and 1.2 (Table 1)

Table 1:  $C\alpha$  RMSD of orthologues *Shigella* and *Salmonella* domains in the IM ring. The structure of *Salmonella* is from the recently published 3.5 Å structure solved by Hu *et al.*[2], RMSD calculation was performed with PDBFold. This table is adopted from Lunelli *et al.*, [55]

<i>Shigella</i>	<i>Salmonella</i>	domain	% matched residues	RMSD [Å]
<b>MxiG</b> 152-200	PrgH 171-223	D2	100	1.66
<b>MxiG</b> 201-272	PrgH 224-294	D3	99	1.58
<b>MxiG</b> 273-340	PrgH 295-362	D4	100	1.29
<b>MxiJ</b> 21-77	PrgK 20-76	D1	100	0.77
<b>MxiJ</b> 97-191	PrgK 96-196	D2	95	1.23

Interestingly, recombinant expressed PrgK<sub>82-200</sub> forms ring structures with a diameter of 10-15 nm and variable length [56]. Occasionally, we observe a structure of similar diameter and variable length upon T3SS purification (Figure 9B) in TEM imaging. Bergeron *et al.* suggested that this structure is an oligomer

## 2 Results

of PrgK<sub>82-200</sub>, comprising the short helical turn in the D1-D2 linker, the D2 domain and the C-terminal flexible region [57]. They speculated that the linker might support the oligomerization of adjacent PrgK subunits, hence leading to the tubular structures upon expression of PrgK<sub>82-200</sub>. Furthermore, it is suggested that the export apparatus defines the 24-fold symmetry of the inner membrane ring, since in the absence of the export apparatus, a 23-fold symmetry was detected in *Salmonella* needle complexes [4]. Assisted by the ring building motive [45], the IM components assemble around it.

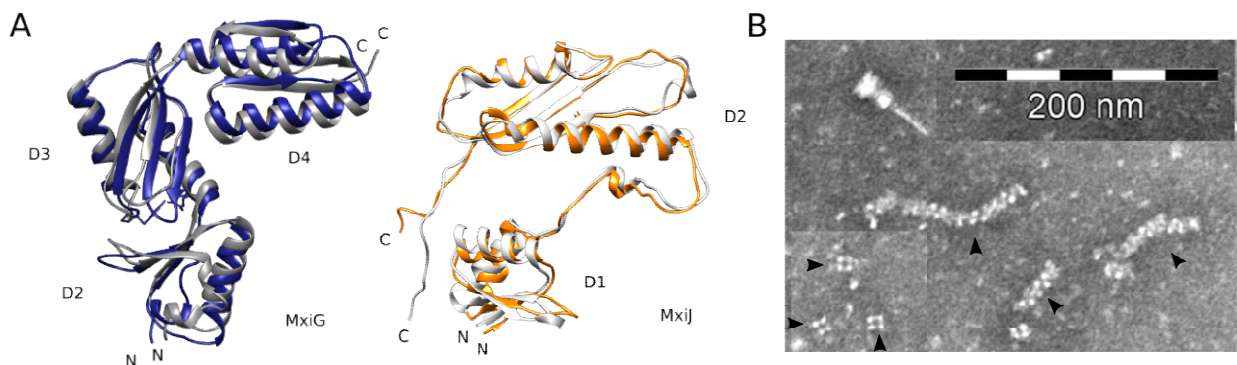


Figure 9: Ring building motives are present in MxiG and MxiJ. A) Structural alignment of MxiG and MxiJ with the *Salmonella* orthologues PrgH and PrgK (5TCP) in grey and light grey. All domains have ring building motifs. B) PTA stained image of T3SS purification. Tubular structures of constant diameter and variable length are indicated with black arrows. Top views are depicted in the lower right corner while the three other indicated structures are side views, the scale bar is given in the upper right corner.

According to mass spectrometry (MS) studies, also lipids binding to interfaces can promote stabilization of the complex and play a role in oligomerization [58]. Therefore it might be possible that the tubular structures visible in TEM imaging could contain the inner membrane ring component MxiJ, but this matter requires further investigation.

## 2.3 Interactions within the periplasmic inner membrane ring

Analysing the structure of the T3SS basal body, key regions important for structural integrity and function of the T3SS could be identified.

The periplasmic inner membrane ring is stabilized by homo- and hetero interactions of MxiG and MxiJ. Each subunit interacts with two other subunit of the same type and two of the other type. The MxiG-MxiG interface is relatively small, with  $\sim 900 \text{ \AA}^2$ , which represents  $\sim 8\%$  of the monomer surface, while the MxiJ-MxiJ interface is almost 3x the area of the MxiG, having approximately the same monomeric volume. The MxiG-MxiJ interface is formed by  $800 \text{ \AA}^2$  from one side and  $630 \text{ \AA}^2$  on the other side.

### 2.3.1 MxiG-MxiG interaction is mediated by polar contacts

MxiG-MxiG interaction is mainly stabilized by polar interactions of the D4 domain, since the D3 and D2 domains of adjacent subunits are separated by a cleft (Figure 10). The  $\alpha 5$  and  $\alpha 6$  helices in the D4 domain of one MxiG subunit interact with the  $\beta 7$  strand and the  $\alpha 3$  helix of the adjacent MxiG subunit (Figure 10B). Mostly residues with long side chains mediate the polar interactions of MxiG subunits.

The MxiG domains have a hydrophobic core (Figure 10A) and the D2-D3 domain interface in one MxiG subunits is stabilized by hydrophobic residues. While  $\sim 9\%$  of the total D3 and D4 domain surface contributes to the interaction site,  $13\%$  and  $10\%$  of the D2 and D3 domain surface, respectively, interact with each other. The solvation free energy  $\Delta^{\ddagger}G$  upon formation of the MxiG subunit is  $-6.8 \text{ kcal/mol}$  for D2-D3 and  $-0.3 \text{ kcal/mol}$  for the D3-D4 interface. Therefore the D2-D3 interface might be relevant for folding of the MxiG subunit in the periplasm.

## 2 Results

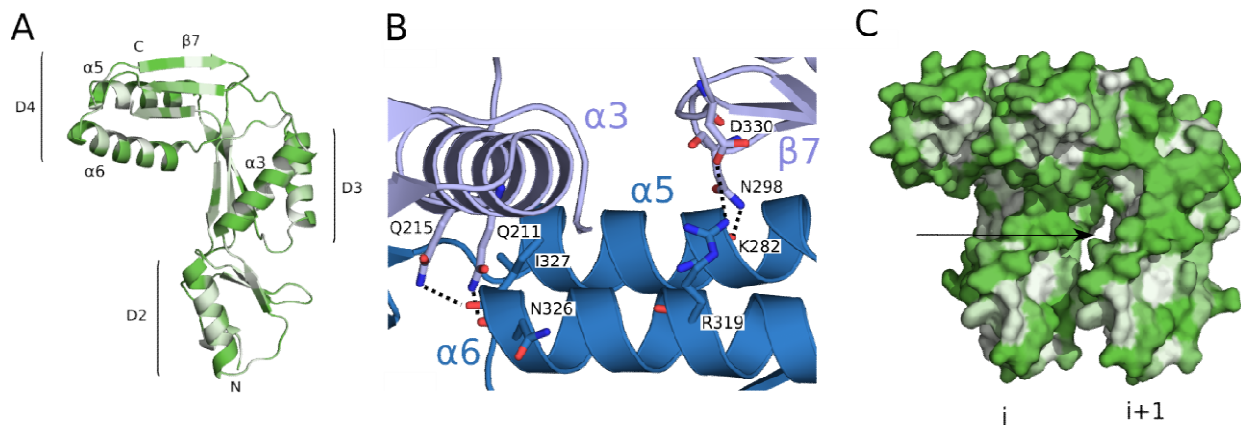


Figure 10: MxiG-MxiG interaction. A) MxiG<sub>152-367</sub> subunit depicted in cartoon representation and coloured according to Eisenberg's hydrophobicity scale, white being hydrophobic. The domains are labelled and B) Polar interaction between adjacent MxiG subunits, coloured in purple and blue. Hydrogen bonds are represented by a dotted line. C) Two neighbouring subunits in surface representation and coloured like in A. The cleft separating neighbouring D2-D3 domains is assigned with an arrow. Panel B is adapted from Lunelli *et al.*, [55]

### 2.3.2 The inner membrane ring is channelled

Two MxiG and three MxiJ subunits form a channel connecting the bacterial periplasm with the export cage, the lumen between the export apparatus and inner membrane ring [59]. From a set of channels identified with ChexVis [60], two channels forming the shortest connection with the widest diameter from periplasm to export apparatus were considered relevant, depicted in Figure 11. The channels share the same path on the export cage side and branch in two periplasmic exits A and B approximately at the MxiG-MxiJ interface. They are interconnected at the branching point and repeated 24-fold in the inner membrane ring. The channel exit B, opening at the D2-D3 MxiG interface, is with  $\sim 65$  Å slightly shorter than the channel exit A, which exits through the D3-D4 domains of MxiG and is  $\sim 75$  Å long (Figure 11B). Both channels share the same path to the export cage, with a local minimal radius of 2 Å, close to the export cage opening. Each channel possesses a local radius minimum of  $\sim 2.5$  Å and  $\sim 3.5$  Å, at around 52 Å and 56 Å after the export cage opening, respectively.

The electrostatic potential of both channels is negative throughout the path along the central line (Figure 11B). Based on the high conservation of the export apparatus components with the flagellar system [61], it is suggested that the translocation of effectors from cytoplasm through the needle is mediated by the proton motive force (PMF) [59, 62, 63]. The PMF might be related to the ATPase activity at the sorting platform, where chaperones are removed from the effectors [59, 64]. The minimal radius of the channel

would be too narrow to allow passage of small cations like sodium in a fully hydrated state [65], but protons to diffuse along a gradient [65]. Local changes in the electrostatic potential along the channel or conformational changes might be critical for T3SS functionality.

Though only few residues that form the channel surface are conserved, a tubular network of similar length and physiochemical properties is present in the *Salmonella* orthologue (Figure 15). The minimal diameter of the *Salmonella* channels is  $\sim 3.5$  Å and the electrostatic potential along the central line becomes positively charged in the opening of the respective channel A to the periplasmic side.

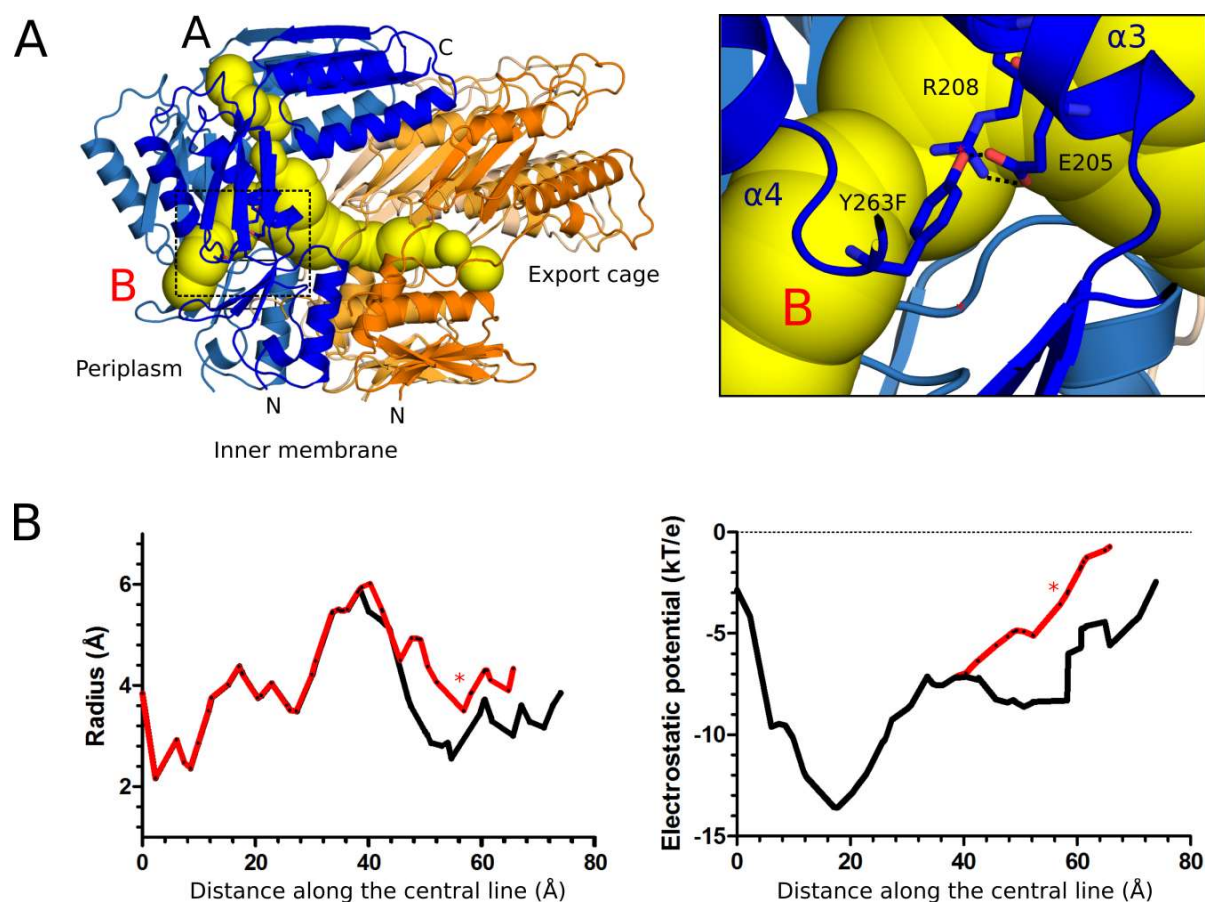


Figure 11: Channels of the periplasmic IM ring. A) The channel is coloured in yellow, the two periplasmic openings are labelled with A and B. On the right hand side a zoom on the channel exit B with the conserved residues Y263, R208 and E205 depicted as sticks. Hydrogen bonds connecting the side chains are depicted with dotted lines. B) The radius and electrostatic potential along the central line of the channels A and B, coloured in black in red, respectively. The channel starting point is at the export cage side, the red asterisk marks the radial minimum of channel exit B where the residues E205, R208 and Y263 are located. This figure is adapted from Lunelli *et al.*, [55]

Three conserved residues are located nearby the local radius minimum of channel B in *Shigella*: E205, R208 and Y263 of MxiG.

## 2 Results

### 2.3.3 Mutational analysis of conserved channel residues

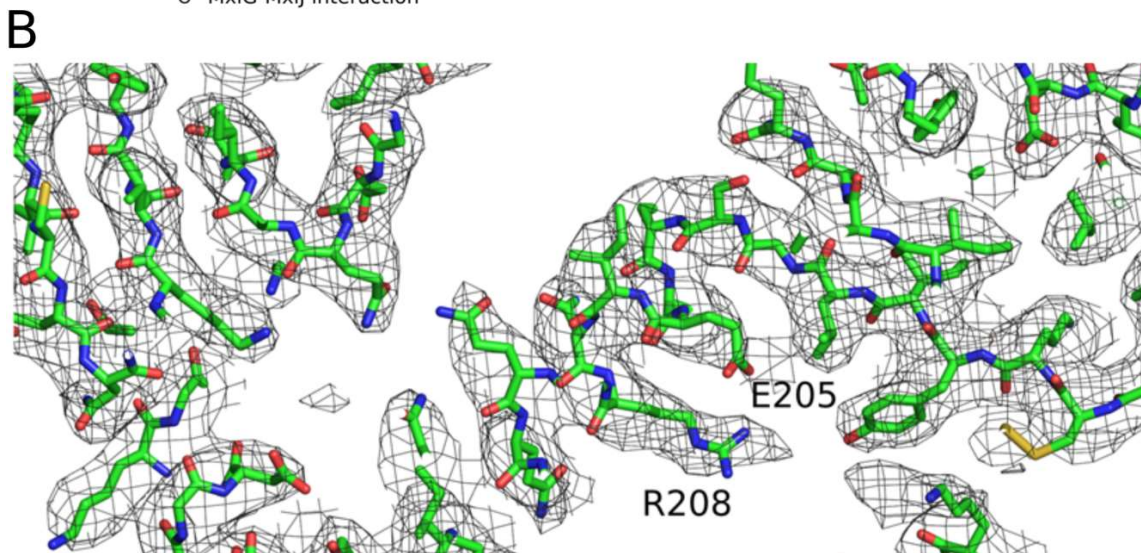
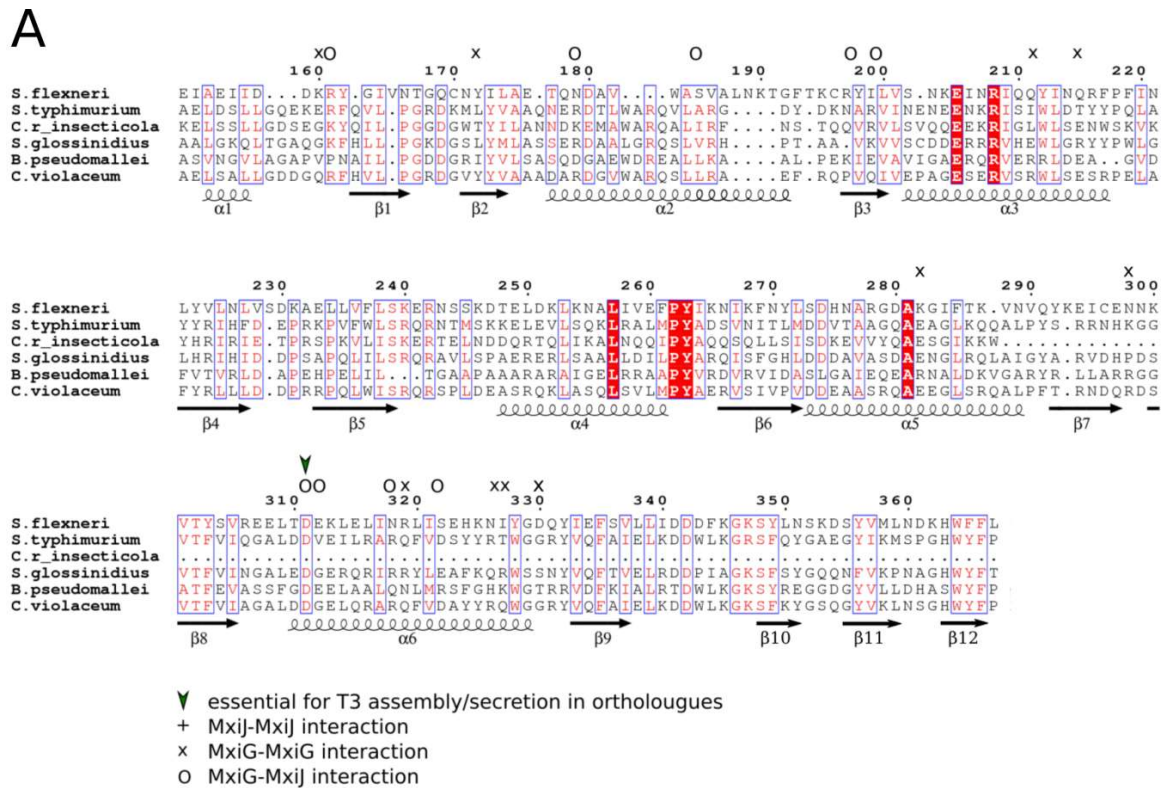


Figure 12: A) Multiple sequence alignment of the periplasmic domains of MxiG. The following proteins of T3SS expressing gram-negative bacteria are aligned: *Shigella flexneri* (POA221), *Salmonella typhimurium* (P41783), *Candidatus regiiella insecticola* (G2H2F2), *Sodalis glossinidius* (Q2NR71), *Burkholderia pseudomallei* (Q63K19), *Chromobacterium violaceum* (Q7NVC0). The secondary structure elements correspond to MxiG. Blue boxes indicate conserved residues with regards to their physicochemical properties. Fully conserved residues are depicted in white letters on red background. Residues involved in intermolecular interactions are marked with x (MxiG-MxiG) or O (MxiG-MxiJ). D311, indicated with a green arrow, was shown to abrogate secretion in *Salmonella* (Bergeron *et al.* 2015) when mutated to arginine. B) The IM ring model in the post-refined EM-map. The model is depicted in stick representation; the residues R208 and E205 are assigned. This figure is adapted from Lunelli *et al.*, [55].

Aligning the sequence to MxiG orthologues of the Type three secretion system PrgH-EprH PFAM family, it seems that only few residues of MxiG<sub>152-367</sub> are fully conserved (Figure 12A). Among them, E205, R208, P262 and Y263 are located in close proximity in a well resolved area near the channel exit B (Figure 12B, Figure 11A). Also in *Salmonella* (PDB ID 5TCP), the respective residues are located close to each other, lining the IM channel (Figure 15). The residues leucine 257 and alanine 281 are located in the hydrophobic core of the D3 and the D4 domain, respectively. E205 and R208 are part of the  $\alpha$ 3 helix, located nearby the hydrophobic D2-D3 interface and are connected by a side chain salt bridge (Figure 11A). Y263 is located in a loop and stabilized by a hydrogen bond of the hydroxyl group with the E205 side chain carboxyl group. Neither E205 nor R208 or Y263 are involved in inter-MxiG interaction. To assess the contribution of E205, R208 and Y263 to T3SS functionality and stability, site-directed mutagenesis was performed and the MxiG mutants expressed from an inducible plasmid in M90T  $\Delta$ *mxiG* knockout strain (Figure 13A).

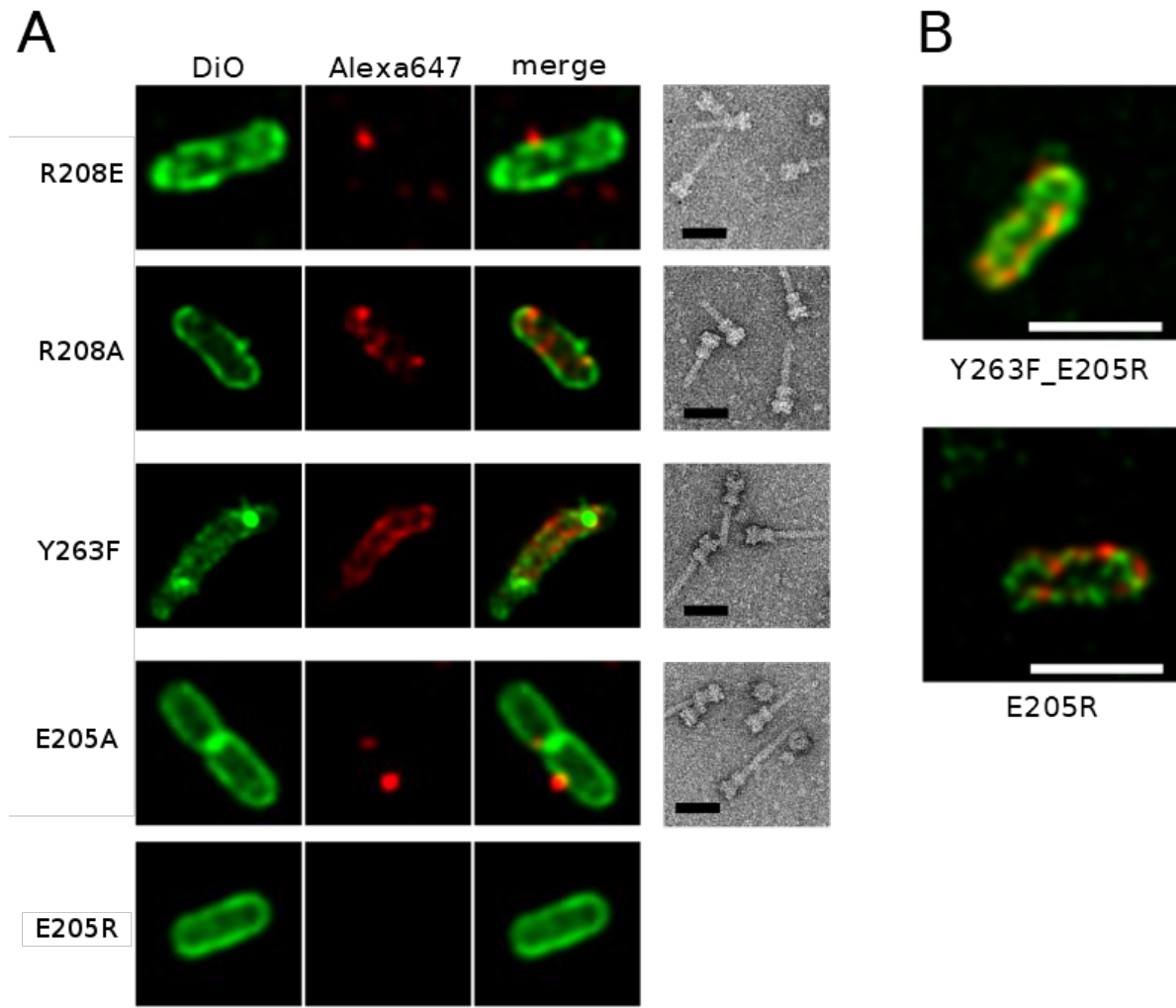


Figure 13: Immunofluorescence images and isolated needle complexes of *Shigella* mutant strains. A) The immunofluorescence images in the first row show the membrane in green, the Strep-tagged needle in red (second row) and the combination of both in the third row. In the fourth row are images of negatively stained needle complexes, isolated from the respective mutant strains. The scale bar represents 50 nm. B) Immunofluorescence images of *Shigella* mutant strains. The bacterial membrane was permeabilized prior staining. The membrane is stained in green, N-terminal Strep-tagged MxiG in red. The scale bar is 2  $\mu$ m. This figure is adapted from Lunelli *et al.*, [55]

Inverting the side chain charge of E205 to arginine leads to abrogated secretion and the strain cannot form needle complexes (E205R). Also the host cell invasiveness is reduced while the alanine mutant E205A is still able to form needle complexes, secrete effector proteins and shows a higher invasiveness compared to the E205R mutant (Figure 13A, Figure 14B). The E205R mutant is expressed and located in the bacterial membrane, as could be shown with immunofluorescence experiments, permeabilizing the bacterial membrane and using the N-terminal Strep-tag for fluorophore binding (Figure 13B). In both

mutants, E205R and E205A, the salt bridge to R208 would no longer be present, leading potentially to a re-orientation of the one or both side chains or neighbouring residues. A charged side chain in the hydrophobic D2-D3 interface might cause improper orientation of the D2-D3 domains and could subsequently impair the stabilization of the MxiG subunits. It could also be that the R208 side chain is pushed more in the direction of the channel lumen, which could cause the down regulation effector secretion (Figure 14B).

In the E205 alanine mutant, the Y263 hydroxyl group could be accessible for stabilization of the R208 side chain. Relocation of the loop containing Y263 could allow the formation of the side chain hydrogen bond, preventing the R208 side chain from moving in the direction of the channel lumen. The D2-D3 hydrophobic interface would still be accessible and the channel lumen not affected.

In contrast to the E205R mutant, the needle complex can be assembled inverting the charge of the R208 side chain (R208E, Figure 13A). Effector secretion and invasiveness are reduced, though (Figure 13B). Also the R208A mutant is able to form functional needle complexes and can secrete effectors and invade host cells (Figure 13A, Figure 14B).

Inverting the side chain charge of R208 abolishes the salt bridge formation between E205 and R208. R208E might form hydrogen bonds with side chains of residues located in the same alpha helix: Q211 or K204. Both possible hydrogen bonds would locate the R208E in the direction of the channel lumen which might cause the reduced effector secretion and invasiveness. The R208A alanine mutant though would not block the channel lumen with a charged side chain. In both mutants, R208E and R208A, the hydrogen bond between Y263 and E205 would still be possible.

Since both mutants, R208E and R208A can still form needle complexes and E205R cannot, R208 seems to be of strict functional relevance while E205 might be important for positioning of the R208 side chain.

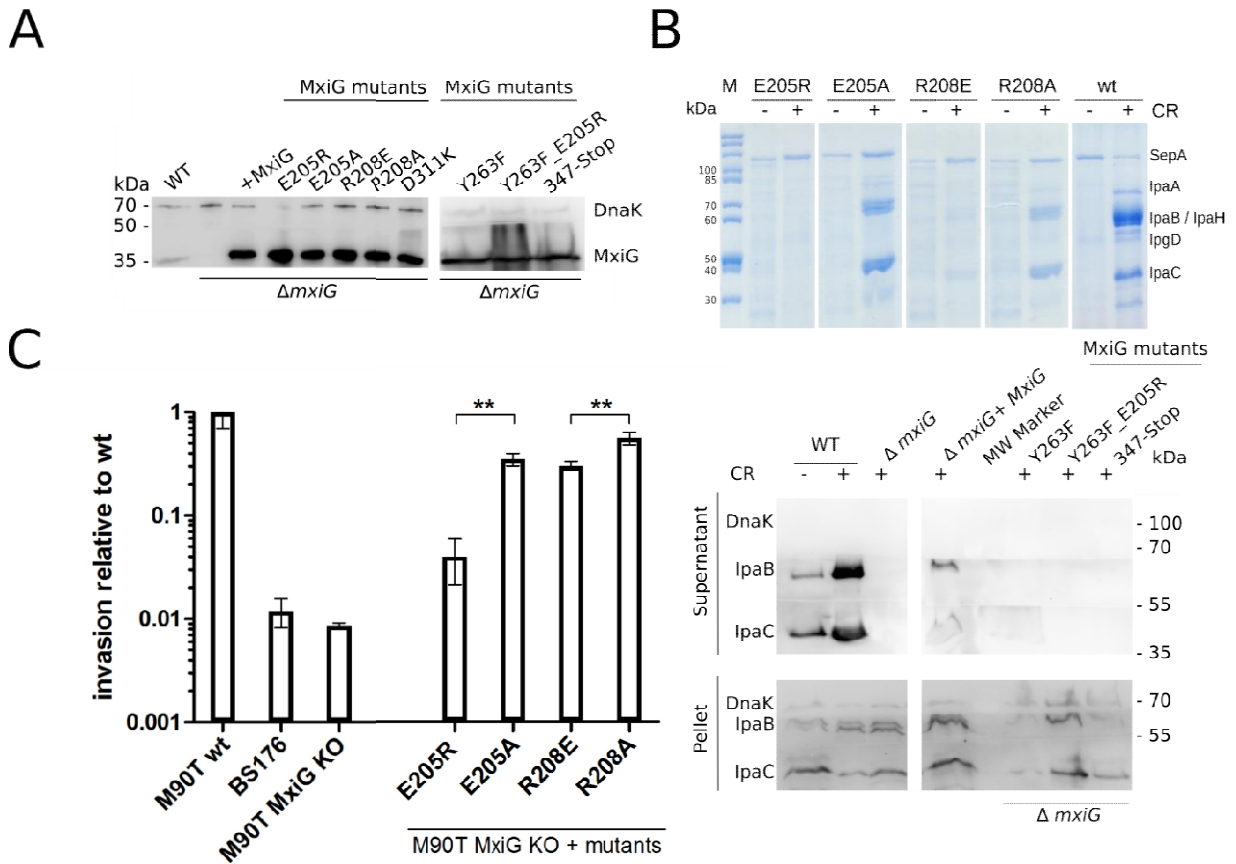


Figure 14: Expression test, secretion assay and invasion assay of *Shigella* mutant strains. A) Western blot of total cell lysates of the indicated *Shigella* strains, normalized on cell density. DnaK served as a loading control. B) Secretion assay of the indicated *Shigella* strains. Secreted proteins were analysed by SDS-PAGE (upper panel) and western blot (lower panel). Effectors are indicated on the right hand side of the SDS-PAGE and on the left side of the western Blot. SepA is secreted independently of the T3 and serves as a loading control for the SDS-PAGE, DnaK as a loading and lysis control in the western Blot. Secretion was induced using Congo red (CR). C) Invasion assay in Caco-2 cells. BS176 is a *Shigella* strain lacking the virulence plasmid. The experiment was performed in technical triplicates and the mutant strains were used in biological duplicates. The error bars assign the standard deviation. A two-sided t-test was performed for E205 and R208, the p-value for sample with \*\* is  $<0.05$ . This figure is adapted from Lunelli *et al.*, [55]

The Y263F mutant can form needle complexes but abrogates secretion (Figure 13A, Figure 14B). The Y263F mutant lacks the hydrogen bond between E205 and Y263. Repositioning of the benzyl ring in the direction of the D2- $\beta$ -sheet, moving the side chain in its preferred rotameric conformation would cause clashes and is therefore less likely to happen. Since the D2-D3 interface is not interfered with, MxiG is still stable. Though, the salt bridged residues E205-R208 could undergo repositioning, leading to impaired effector secretion.

The double mutant E205R\_Y263F can neither form needle complexes nor secrete effectors. The altered electrostatic environment near the hydrophobic D2-D3 interface could destabilize MxiG, impairing the structural stability of the T2SS needle complex. Impaired secretion might be an effect of the destabilized needle complex or due to electrostatic repulsion of R208 with E205R, pushing R208 in the direction of the channel lumen.

Also the *Salmonella* inner membrane ring (PDB ID 5TCP) possesses a similar network of channels and the conserved residues in the channel exit B show a similar orientation of the orthologous PrgH residues E228, R231 and Y285. This could lead to the assumption that this area is conserved functional relevant structural feature (Figure 15) of the T3SS needle complex.

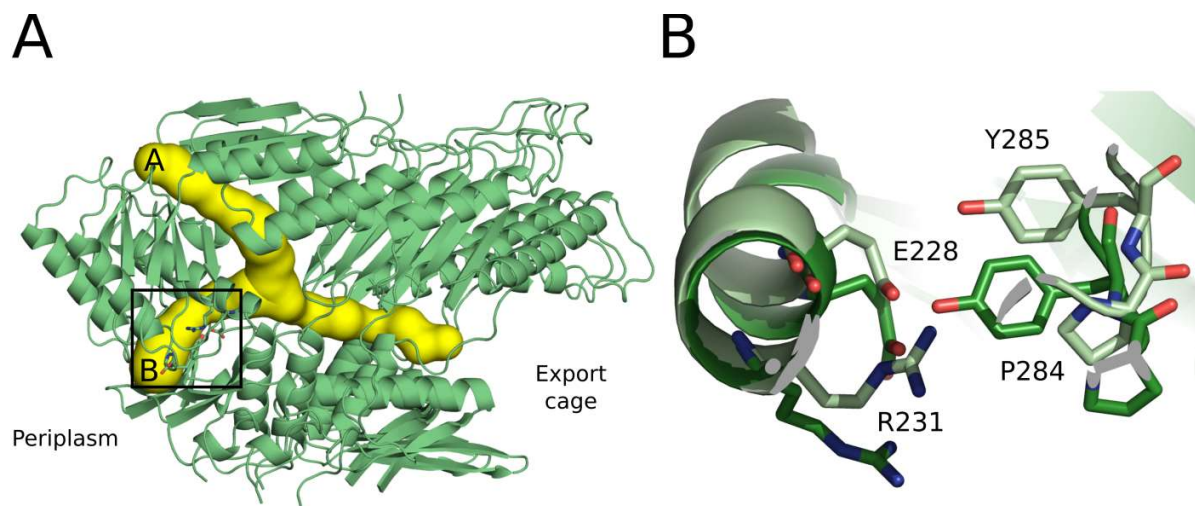


Figure 15: *Salmonella* possess channels in the IM ring. A) The *Salmonella* IM ring model (PDB ID 5TCP) with 2 PrgH subunits and 3 PrgK subunits in cartoon representation. The equivalent channels A and B are depicted in yellow. B) Structural superposition of PrgH (light green) with MxiG of the periplasmic IM ring model (dark green). The depicted region focuses on the area boxed in A). The conserved residues E228, R231, P284 and Y285 and the orthologous *Shigella* residues are depicted as sticks.

Further mutational analysis, also on orthologues, in combination with high-resolution structures could provide insights in the interplay between the residues and their role in effector transport and needle complex stability.

## 2 Results

### 2.3.4 The MxiG and MxiJ interface possess polar contacts

The MxiG-MxiJ interaction site has two main interfaces: at the D4 domain of MxiG, which sandwiches between two MxiJ D2 domains and at the MxiG D2 domain, which interacts with the C-terminal loop (P188-V197) of one MxiJ subunits and the  $\alpha$ 1- $\beta$ 2 linker of the adjacent MxiJ subunit.

The  $\alpha$ 6 helix of the MxiG D4 domain is located in a cleft formed by the two  $\alpha$ 5 helices and the  $\beta$ 6 strand of adjacent MxiJ subunits. The conserved MxiG residue D311 is located in this cleft and interacts with side chains of the conserved K167 and R168 of two adjacent MxiJ subunits, respectively (see Figure 16A). Also the backbone amide of MxiG V184 can interact with the side chain of D311.

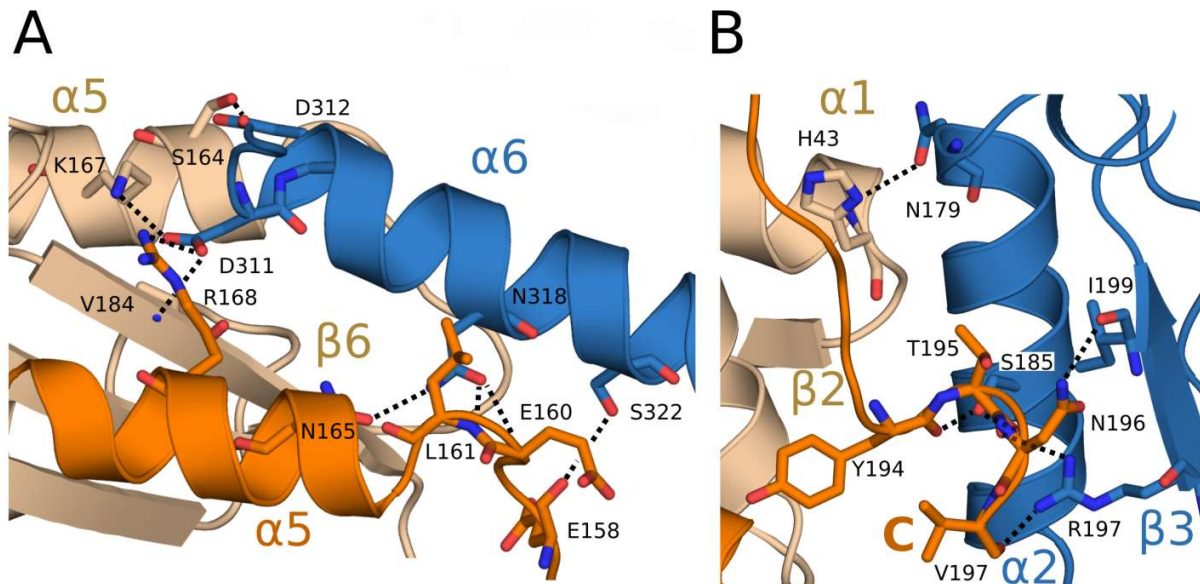


Figure 16: Polar interaction of MxiG (blue) and MxiJ (orange and beige). Interaction residues are depicted as sticks and label, the hydrogen bond is represented by a dotted line. Secondary structure elements are assigned. A) Interaction of the MxiG D4 domain with the D2 domain of MxiJ B) The C-terminus of MxiJ interacts with the D2 domain of MxiG. This figure is adapted from Lunelli *et al.*, [55]

Site-directed mutagenesis showed that substituting aspartate 311 with lysine reduced secretion of effectors compared to M90T wt (see Figure 17B). Also in invasion assays did the D311K mutant show significant reduced invasiveness compared to the M90T wt strain (Figure 17C). Substituting the orthologues aspartate with arginine led to abrogated secretion of SipA in *Salmonella* [57]. Interestingly,

double mutants of the respective interacting MxiJ orthologues proteins PrgK K168 and R169 to alanine were needed to abrogate secretion, while the single mutant K168E did not abrogate secretion [57].

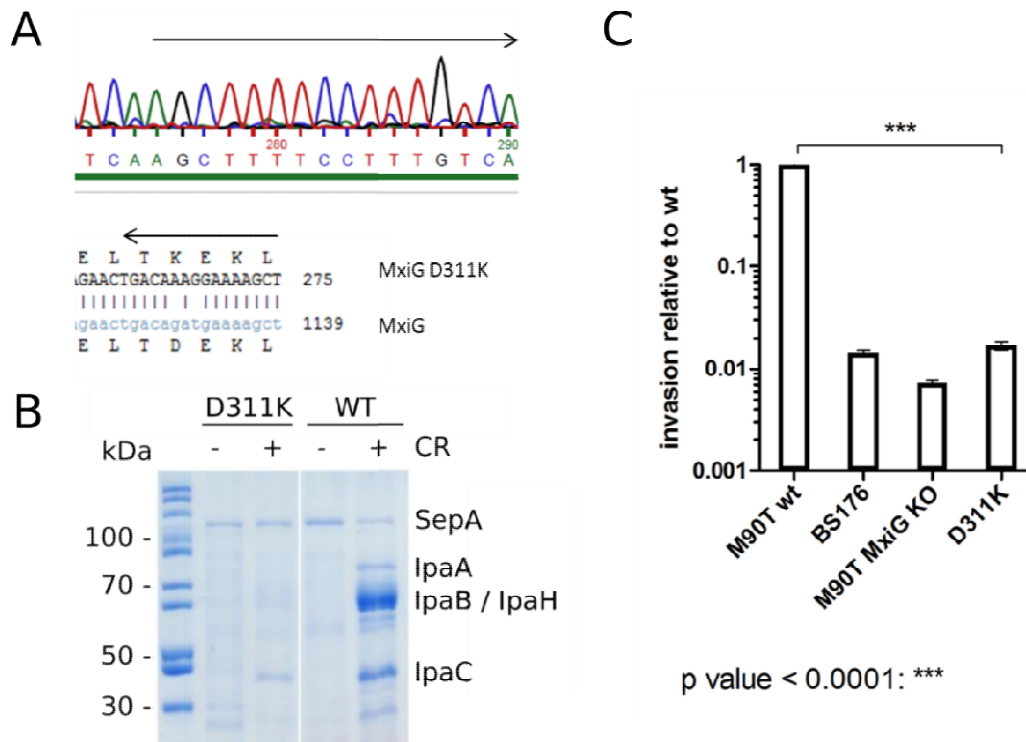


Figure 17: Site-directed mutagenesis of MxiG D311K. A) Sequencing result of D33K (upper panel) and the D311K mutant reverse complement aligned to wt MxiG (lower panel). The nucleotide 3'GAT 5' was mutated to 3'AAG 5'. B) Secretion assay of D311K, expressed on a plasmid in M90T MxiG KO strain in comparison to wt M90T. Secretion was induced using Congo red (CR). Secreted effectors are indicated on the right side, SepA serves as a T3 independently secreted loading control. C) Invasion assay in Caco-2 cells of D311K in M90T MxiG KO strain in comparison to M90T wt, the BS176 strain lacking the virulence plasmid and the M90T MxiG KO strain. The experiment was performed in technical triplicates and the mutant strains were used in biological duplicates. The error bars assign the standard deviation. A two-sided t-test was performed for the M90Twt strain and D311K. Panel B of this figure is adapted from Lunelli *et al.*, [55]

One of the two MxiJ residues, R168 or K167, might be sufficient to maintain the interaction of MxiG and MxiJ in this area. TEM images of negative stained needle complex from the strain expressing D311K might give an idea whether D311K is needed for IM ring stability maintenance and therefore leads to abrogated secretion or if it is linked another way to inhibition of functionality.

## 2 Results

### 2.3.5 MxiJ subunits are connected by polar and hydrophobic interactions

The MxiJ-J interface comprises a roughly 2.5 - 3x larger area than the MxiG-G interface, with 19% of the MxiJ monomer surface forming a total surface area of  $\sim 2400 \text{ \AA}^2$ .

In contrast to MxiG, both domains of MxiJ are in contact with the domains of the adjacent subunit. The MxiJ domains D1 and D2 are separated by a  $\sim 20$  amino acid long linker. This D1-D2 linker allows a stacked arrangement of MxiJ, with the D2 domain of one subunit positioned on top of the D1-D2 linker and the D1 domain of the adjacent subunit (Figure 18), which is also present in PrgK in *Salmonella* [38, 57].

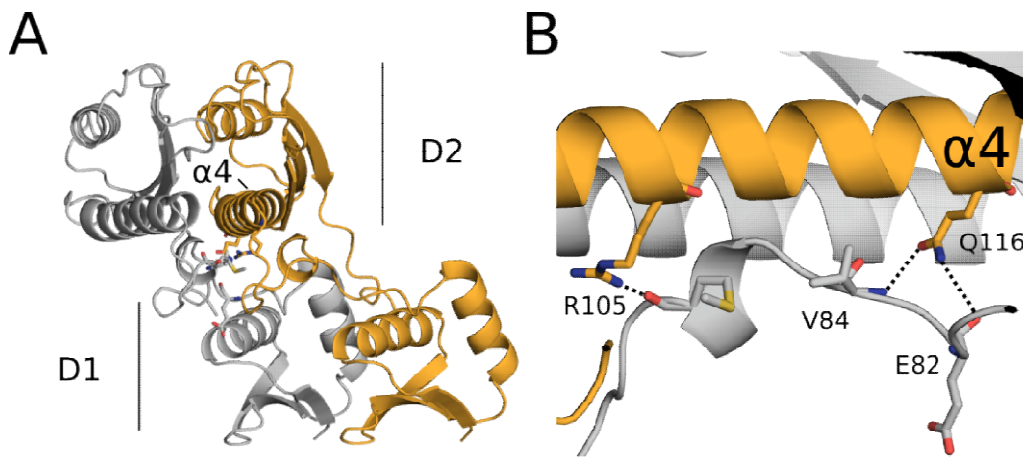


Figure 18: Adjacent MxiJ subunits are stacked. A) Two adjacent MxiJ subunits in cartoon representation, interacting residues of the  $\alpha 4$  helix and the D1-D2 linker are depicted as sticks. B) Interaction between residues of the D1-D2 linker and  $\alpha 4$  helix of the D2 domain. Hydrogen bonds are depicted as dotted lines, residues are labelled.

Several of the MxiJ residues forming hydrogen bonds to stabilize interactions between subunits are conserved among orthologues (Figure 19) and have been shown to be important for T3SS functionality. For instance, mutations of E102, A104 and H130, part of the D2 domain, led to abrogated secretion in *Pseudomonas* [66]. In comparison to MxiG, MxiJ is of higher sequence conservation.

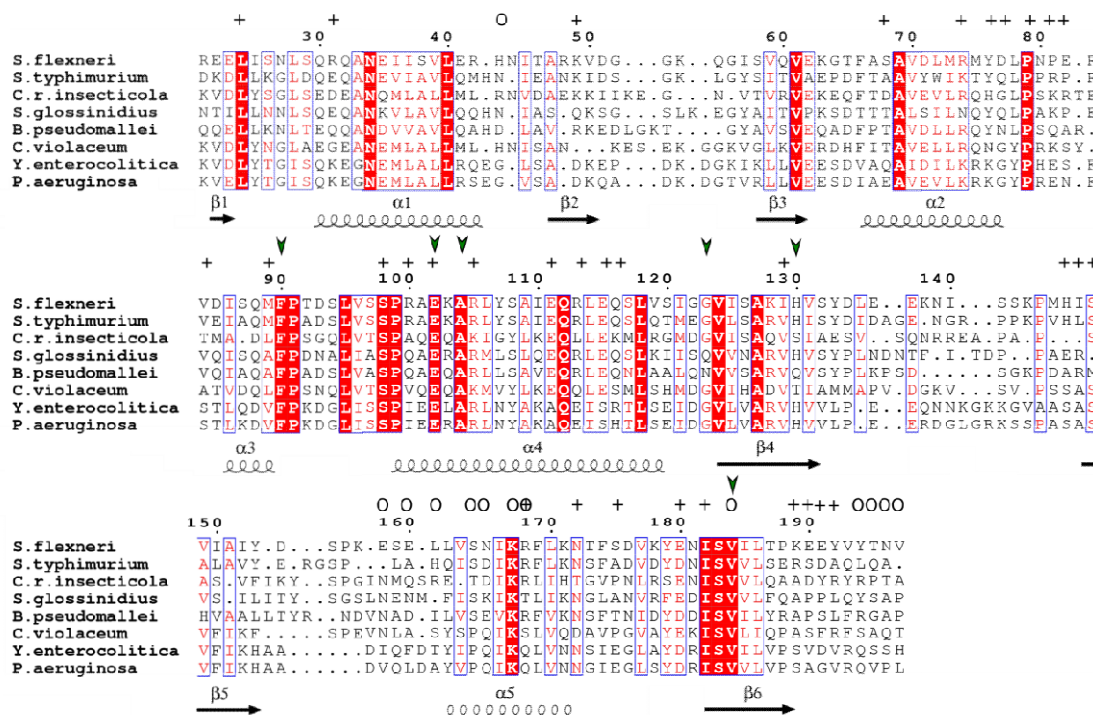
MxiJ<sub>21-197</sub>

Figure 19: Multiple sequence alignment of MxiJ<sub>21-197</sub>. MxiJ orthologues of the following species are aligned (UniProt code in brackets): *Shigella flexneri* (Q06081), *Salmonella typhimurium* (P41786), *Candidatus regiiella insecticola* (E0WTJ1), *Sodalis glossinidius* (Q2NVJ4), *Burkholderia pseudomallei* (Q3JL03), *Chromobacterium violaceum* (Q7NUV9), *Yersinia enterocolitica* (Q01251) and *Pseudomonas aeruginosa* (Q9I314). All proteins mentioned belong to the SPI-1 family, except for *Pseudomonas* PscJ, which is part of the Ysc family. The secondary structure depiction corresponds to *Shigella*. Boxed residues are similar with regards to their physicochemical properties; identical residues are depicted in white letters on red background. Residues marked with + are involved in MxiJ-MxiJ interaction, marked with O are MxiJ-MxiG interaction. Green arrows indicate residues that were shown to be of importance for T3SS assembly or secretion in orthologues. This figure is adapted from Lunelli *et al.*, [55]

Like in MxiG are the MxiJ domains internally stabilized by hydrophobic interactions, mainly formed by amphipathic helices. Hydrophobic interactions between subunits are predominantly mediated by the D2 domains (Figure 20). A hydrophobic ring-shaped patch, that contains conserved residues like F90, surrounds a polar region. Mutational analysis in *Salmonella* suggests that the F90 orthologue contributes to MxiJ interaction [57]. Both, the central polar region and the surrounding hydrophobic belt contribute to MxiJ-MxiJ stability (see Figure 20).

## 2 Results

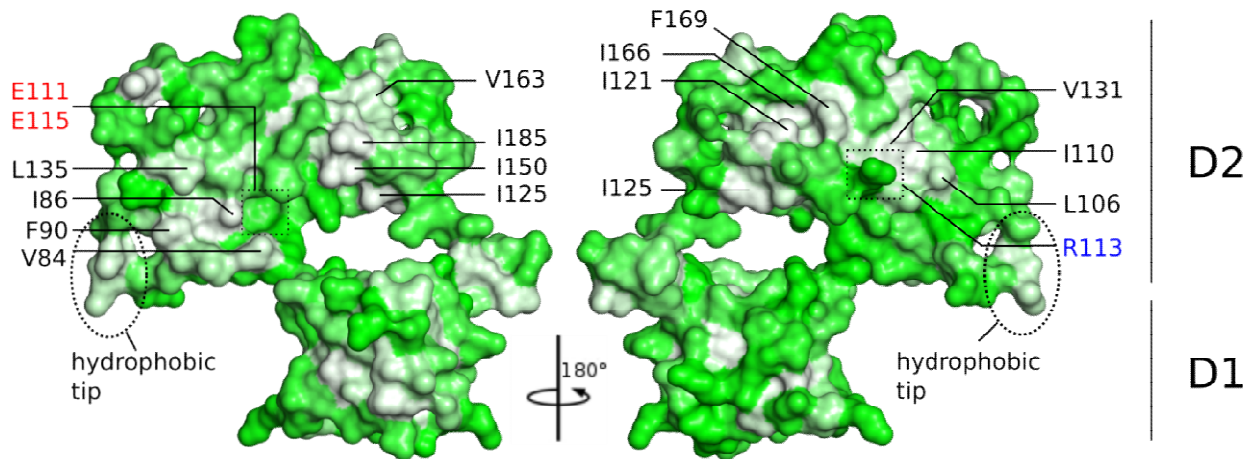


Figure 20: The MxiJ-MxiJ interaction interface. The surface is coloured according to Eisenberg's Hydrophobicity scale, white representing the most hydrophobic. R113 is part of a polar pod, which is surrounded by a hydrophobic belt. The corresponding adjacent subunit shows a hydrophobic belt surrounding a polar cavity, formed by E111 and E115 in which R133 can bind. The polar "plug" and "socket" are highlighted by a dotted box. The hydrophobic tip of the loop 90-99 facing the export apparatus is assigned. This figure is adapted from Lunelli *et al.*, [55]

The central polar "plug" contains R113, part of the  $\alpha 4$  helix, and interacts with side chains of E111 and E115, which are located in the  $\alpha 4$  helix of the adjacent MxiJ subunit (Figure 19) and form the corresponding "socket".

Other conserved residues that are involved in D2-D2 interaction are E102 and S98, which are also located nearby the loop F90-P99, that comprises conserved hydrophobic residues ("hydrophobic tip", Figure 20). The hydrophobic residues of the loop F90-P99 located at the tip face the partially hydrophobic surface of the export apparatus.

Conserved residues that are involved in mediating polar contacts between the D1 and D2 domain are depicted in Figure 21. The conserved L24 and K49 of the adjacent D1  $\beta$ -sheet interact by a side chain hydrogen bond. Also the C-terminus of one MxiJ domain interacts with residues of the D1 domain of the adjacent MxiJ subunit (Figure 21).

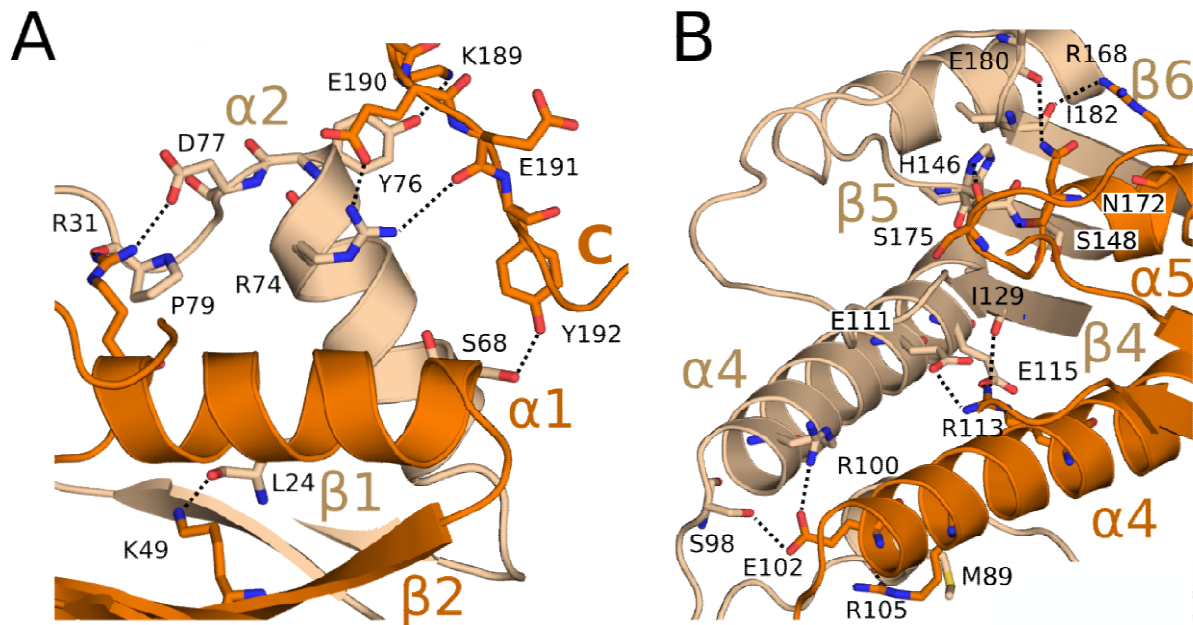


Figure 21: Polar interaction of MxiJ. Interacting residues are depicted as sticks and labelled; the hydrogen bond is represented by a dotted line. Secondary structure elements are assigned. A) Interactions involving the D1 domain. B) Polar interactions in the D2 domain, except the backbone interaction of I147-N172, which could not be depicted in this representation. This figure is adapted from Lunelli *et al.*, [55]

In general, the MxiJ-MxiJ interaction is relatively tight, compared to the MxiG-MxiG interaction, partially caused by the stacked arrangement. Additionally, the protein exposes higher sequence conservation, similar to the proteins of the export apparatus. The polar “plug”-“socket” interaction has not yet been described in orthologues. The hydrophobic tip facing the export apparatus could be of functional relevance allowing rotational freedom or be a focal point for IM ring assembly, as suggested by Hu *et al.* [2]. To test this hypothesis, point mutants of the loop F90-P99 were generated, reducing the hydrophobicity or substituting them for charged side chains. The biological effect of those mutants can be tested in future experiments.

## 2 Results

### 2.4 The IM ring is connected to the OM ring via $\beta$ -sheet augmentation

The 566 amino acid long protein MxiD comprises the outer membrane ring and is part of the connector. After sec-dependent translocation into the periplasm and cleavage of the N-terminal 22 signal peptide, the protein has an apparent molecular weight of ~60 kDa. The protease resistant secretin  $\beta$ -barrel was suggested to be the driving force for assembly of the outer membrane ring [67]. The N3 and secretin domains are well conserved and are located on top of the connector, interacting with the outer bacterial membrane while the N0 and N1 domain (amino acid 34-171) comprise the connector. The connector interacts in the N0 domain with the C-terminus of MxiG.

#### 2.4.1 The 15- and 16-fold symmetry in the secretin and connector region

Focussed refinement of the cryo-EM reconstructions on the secretin, the N3, N0 and N1 region applying 16 fold symmetry resulted in a map of ~6 Å angstrom in the secretin region, while in the N0 and N1 region, the map was of ~ 4 – 4.5 Å resolution. The  $\beta$ -barrel of the secretin was poorly resolved and not allowing tracing of the backbone (Figure 22).

The unsymmetrized C1 map revealed that the outer membrane ring, comprising the N3 and the secretin domain, actually adopts a 15-fold symmetry, while the connector region adopts a 16-fold symmetry.

For the secretin domain, an InvG based homology model generated with SWISS-MODEL based on the open secretin structure published by Hu *et al.* 2018 [68] was positioned in the unsymmetrized C1 map as rigid body, performing an extensive globular search with Chimera, using the top hits for the generation of the model. Generation of the homology model of the N3 domain and the secretin and subsequent global fit in Chimera was done by Dr. Michele Lunelli.

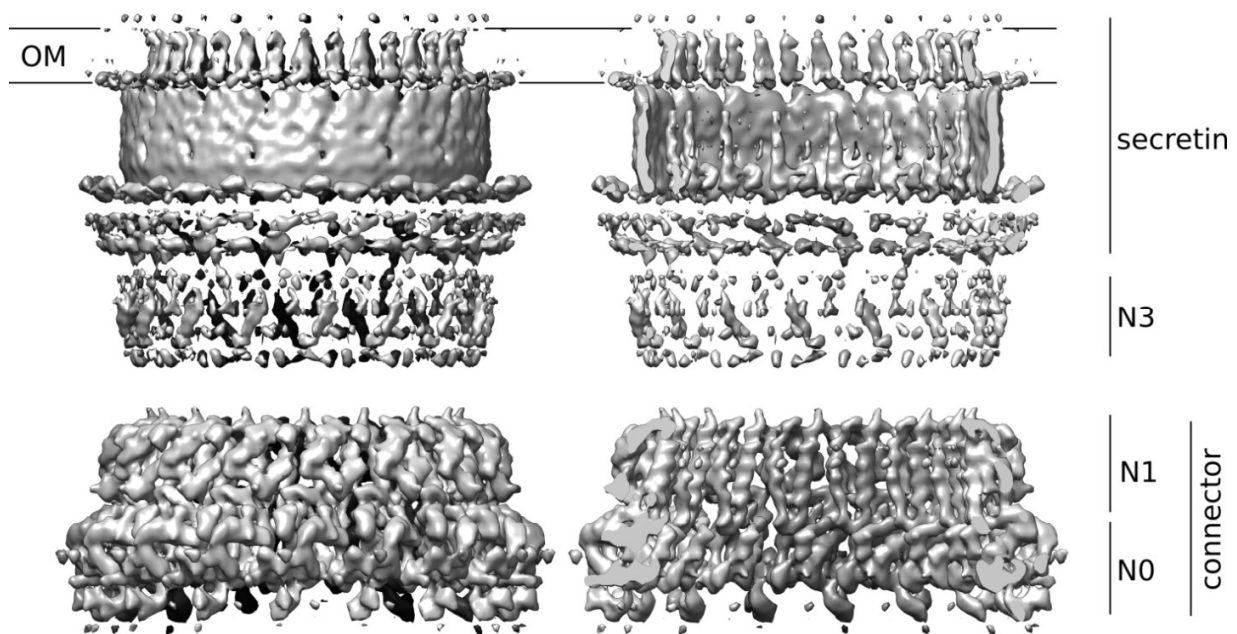


Figure 22: C16 cryo-EM map of the *Shigella* needle complex, derived from imposing 16-fold symmetry upon refinement, focussed on the N3, secretin and the connector. The needle and the inner rod and export apparatus were masked out. The threshold level is 0.09. On the left side a front view is depicted while the right image is a vertical cross-section. The backbone in the N3 and secondary structure features are visible in the connector, while the protein backbone cannot be traced in the secretin domain.

In isolated secretin rings lacking the inner membrane ring, the N0 domain remained unstructured [3, 38] while in the presence of the inner membrane ring, it was much better resolved [2]. Also secondary structure prediction of the MxiG C-terminus suggested the presence of 2 – 3  $\beta$ -strands. To resolve this feature, that would connect the inner membrane ring with MxiD, an 8 fold symmetry map was needed.

A focused reconstruction of the IM ring and the connector applying 8 fold symmetry resulted in a map of  $\sim 4$  Å resolution in the connector region (Figure 25). Modelling and refinement was therefore done in this map, based on a homology model of *E. coli* EscC (PDB ID 3GR5) for MxiD<sub>37-171</sub>, while the C-terminus of MxiG was modelled *de novo* in coot, following the density and taking large side chains as an orientation.

## 2 Results

### 2.4.2 A RBM is present in the N1 domain of MxiD<sub>34-171</sub>

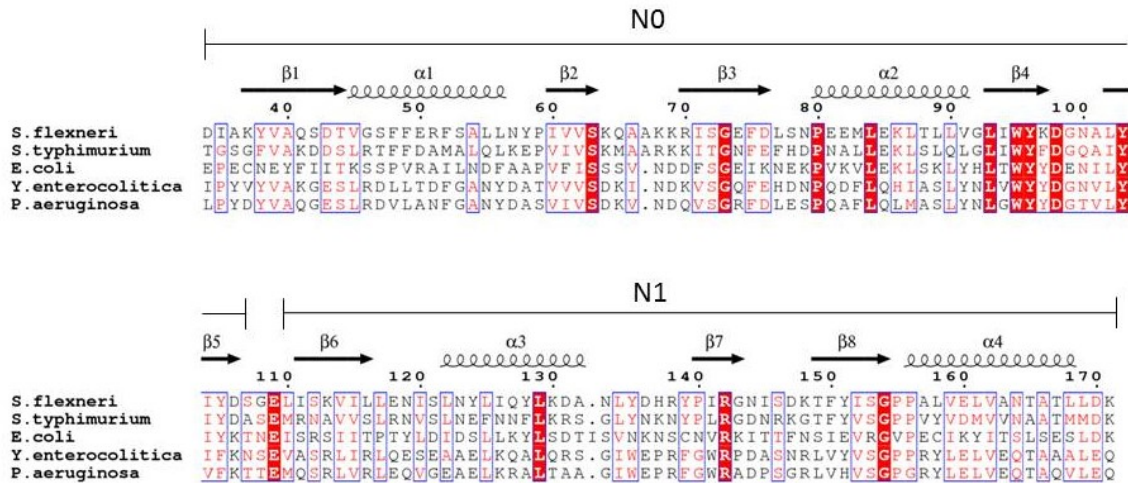


Figure 23: Multiple sequence alignment of MxiD<sub>34-171</sub> to orthologues proteins of gram-negative bacteria expressing T3SS. Sequence numbering, domains and secondary structure elements of MxiD are indicated. Residues conserved with regards to their physio-chemical properties are indicated by blue boxes. Identical residues are depicted in white letters on red background. MxiD orthologues are aligned; the UniProt code is indicated in brackets: *Shigella flexneri* (Q04641), *Salmonella typhimurium* (P35672), *E. coli* EPEC (B7UMB3), *Yersinia enterocolitica* (Q7BRZ9), and *Pseudomonas aeruginosa* (P95431) were aligned. The N1 domain comprises an inverted ring building motive with  $\beta\alpha\beta\beta\alpha$  topology. This figure is adapted from Lunelli *et al.*, [55]

Like in the domains of the periplasmic inner ring, an RBM is present in the N1 domain of MxiD (Figure 23). The MxiD RBM is inverted, exposing a  $\beta\alpha\beta\beta\alpha$  topology. The N0 domain though is formed by two amphipathic helices, sandwiched between two antiparallel  $\beta$ -sheets. One three-stranded  $\beta$ -sheet faces the N1 domain while the two-stranded sheet faces the inner membrane ring (Figure 24). The  $\beta$ -strands 4 and 5 of the N0 domain comprise hydrophobic residues of high conservation while only a few residues of the N1 domain are highly conserved.

### 2.4.3 MxiD and MxiG $\beta$ -sheet augmentation is essential for needle formation

To form the connector, 16 subunits of MxiD interact with the C-termini of MxiG. The two-stranded  $\beta$ -sheet of the N0 domain augments with the three-stranded anti-parallel  $\beta$ -sheet formed by two out of three MxiG C-termini (Figure 22A).

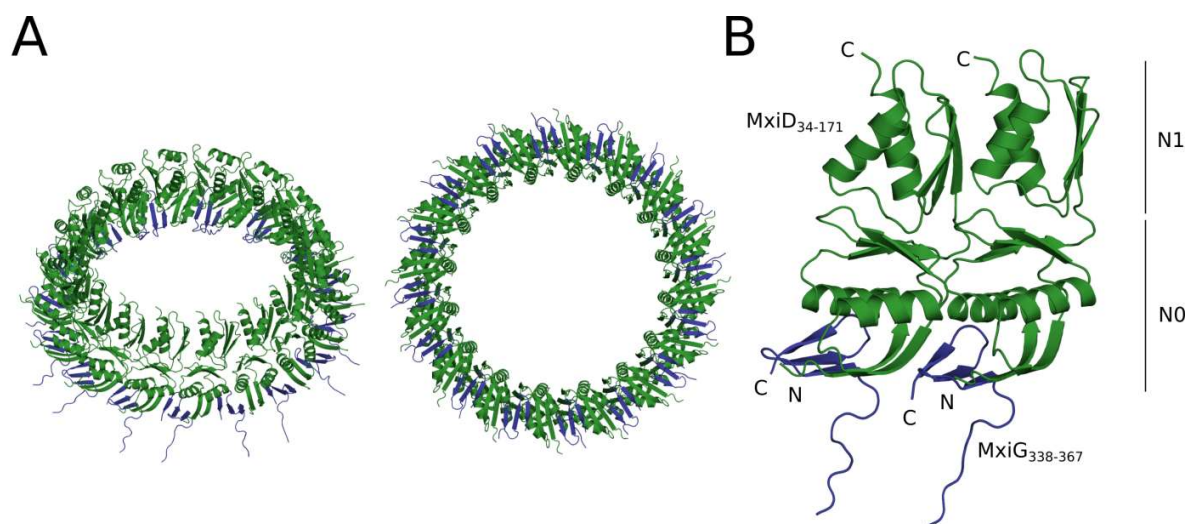


Figure 24: Model of the connector. A) Tilted top view (left) and bottom view (right) of the connector model in cartoon representation. MxiG is depicted in blue, MxiD in green. B) Two adjacent MxiD and MxiG subunits of the connector, coloured and depicted like in A). The domains are indicated on the right-hand side. This figure is adapted from Lunelli *et al.*, [55]

The tilted angle of the MxiG  $\beta$ -sheet and the inflection of the MxiD  $\beta$ -sheet facilitates formation of the  $\beta$ -sheet ring. The MxiD sheet is bent approximately at the middle up to  $\sim 45^\circ$ . One side of the MxiG sheet forms hydrogen bonds with the upwards bent part of the MxiD sheet while the adjacent MxiG sheet forms hydrogen bonds with the part of the MxiD sheet that is parallel to the IM ring (Figure 24B).

The third MxiG C-terminus could be located in the  $\sim 15$ - $20$  Å space between the IM ring and the connector. A density is visible in this area but the resolution did not allow modelling (Figure 25). The first two C-termini of MxiG augment with MxiD, while we expect the third MxiG C-terminus of the MxiG triade to be flexible and fold between the IM ring and the connector. The recently published *Salmonella* structure [2] (PDB ID 6PEM), shows that the third C-terminus of the IM ring subunit folds in a two-stranded  $\beta$ -sheet, suggested to stabilize the IM-connector interaction. This  $\beta$ -sheet is located perpendicular to the augmentation ring in the connector, facing the periplasm. The first two strands of the C-terminal form the

## 2 Results

sheet, while the region that folds into the  $\beta$ 12 strand in the other InvG termini folds back into the region between the IM ring and the connector. This is approximately the area where we see cryo-EM density (Figure 25).

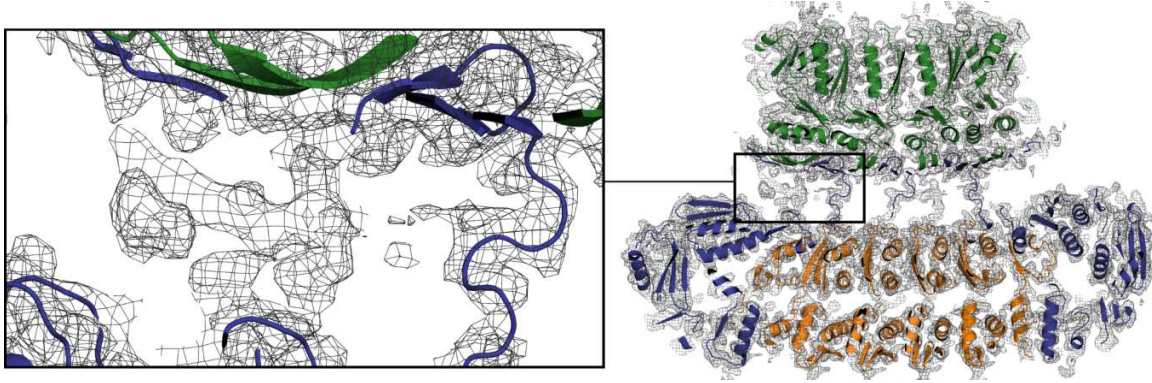


Figure 25: Density of the C8 symmetrised post-processed map of the apo NC. The model of the IM ring is depicted in blue and orange, the MxiD connector is depicted in green. The cryo-EM density in the space between the IM ring and the connector region is boxed and enlarged. It comprises a density which could be interpreted as the C-terminus of MxiG, which does not intercalating with the MxiD N0  $\beta$ -sheet. This figure is adapted from Lunelli *et al.*, [55]

The MxiD-MxiG  $\beta$ -sheet ring contains hydrophobic residues, forming a continuous hydrophobic belt. The hydrophobic surface is additionally stabilized from top by residues of the N0 domain  $\alpha$ -helices (Figure 26A). Also in the *E.coli* T2SS are the OM and IM ring connected by  $\beta$ -sheet augmentation [16] as found in the crystal structure of IM protein GspC<sup>HR</sup> in complex with the N-terminal region of OM ring protein GspD.

Mutating hydrophobic residues of the  $\beta$ -sheet in GspC<sup>HR</sup> to arginine abrogated binding to GspC in *Vibrio cholera* two-hybrid studies [16]. Also mass spectrometry and cross-linking analysis did suggest an interaction of the C-terminus of PrgH and the N-terminus of InvG [69].

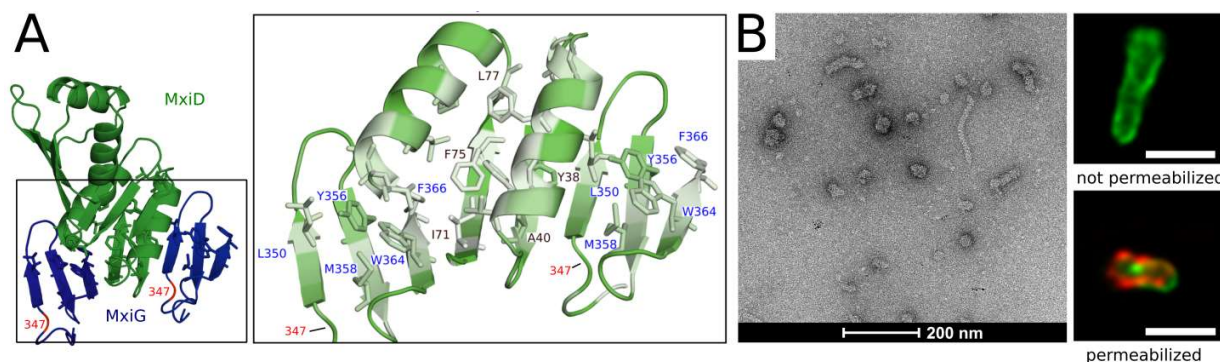


Figure 26: The  $\beta$ -sheet augmentation in the connector. A) Hydrophobic interaction of the  $\beta$ -sheet augmentation. Two MxiG C-termini and the augmenting  $\beta$ -sheet and the  $\alpha$ -helices of the MxiD N0 domain are depicted in top view. Hydrophobic MxiG residues are labelled in blue, MxiD residues in black. B) Negative stained TEM image of needle complex isolation and immunofluorescence images of a *Shigella* strain lacking the C-terminal MxiG  $\beta$ -sheet. The bacterial membrane is stained in green with a lipophilic dye while Strep-tagged proteins are detected with a red fluorescent antibody; the scale bar is 2  $\mu$ m. Substituting the MxiG residue 347 with a stop codon, no needle (Strep-MxiH) could be detected on the bacterial surface. In permeabilized *Shigella*, Strep-MxiG 347-stop could be detected in the membrane. No intact needle complexes could be isolated from *Shigella* expressing *Strep-mxiG-347-stop*, as depicted in the negative stain TEM image on the left side. This figure is adapted from Lunelli *et al.*, [55]

Deleting the C-terminal  $\beta$ -sheet of MxiG by substitution of residue 347 with a stop codon, no Strep-tagged needle could be detected on the surface of the bacteria in immunofluorescence experiments (Figure 26B).

Both, Strep-MxiG-347-stop and Strep-MxiH were present in M90T  $\Delta$ *mxiG* for this experiment. Permeabilizing M90T  $\Delta$ *mxiG* expressing *Strep-mxiG-347-stop* only, Strep-MxiG could be detected in the bacterial membrane. Performing a needle complex isolation on the bacteria, aggregated protein was visible in the negative stained images, though. Since *Strep-mxiG-347-Stop* is expressed (Figure 14B) and the protein located in the bacterial membrane (Figure 26B), the absence of needles and intact basal bodies cannot be explained by aggregation and improper processing of the MxiG-mutant but is rather caused by the lack of the C-terminal domain. Furthermore, secretion assays and subsequent western blot analysis showed a reduced secretion of the effector proteins IpaB and IpaD (Figure 14B).

Therefore it is possible to conclude that the C-terminal MxiG  $\beta$ -sheet is essential for the connection of the inner and outer basal body rings, which is required for the formation of the needle in the T3SS and T3SS functionality.

## 2 Results

### 2.5 MxiD<sub>34-171</sub> inter- and intramolecular interaction

The connector domain of MxiD comprises two globular subdomains, the N0 and N1 domain. It was shown that in the absence of the inner membrane ring, the N0 domain is rather flexible and requires the presence of the inner membrane ring to be resolved [3]. The MxiD<sub>34-171</sub> connector subunits are stabilized by polar and hydrophobic interactions. Interaction between two adjacent subunits is mediated by polar and hydrophobic contacts between N1 domains and a loop of the N0 domain while the N0 domains are separated from each other, allowing the insertion of the C-terminal MxiG  $\beta$ -sheet. The N0 and N1 interface in one subunit is mainly stabilized by hydrophobic interaction. The hydrophobic residues involved in the interface are similar in orthologues while the residues forming polar contacts are mostly not conserved.

#### 2.5.1 The N0-N1 interface is stabilized by hydrophobic and polar interactions

The N1 and N0 domain possess hydrophobic cores, formed by the amphipathic helices and hydrophobic residues present in all  $\beta$ -sheets of MxiD<sub>34-171</sub>, stabilizing the domains internally (Figure 26, Figure 27).

For the N0-N1 interaction, the  $\beta$ 4 and  $\beta$ 5 strand of the N0 domain are important. Mostly hydrophobic residues are located in the  $\beta$ 4 and  $\beta$ 5 strand, which interact with hydrophobic residues of the amphipathic  $\alpha$ 4 helix and the loop connecting the  $\alpha$ 3 helix with the  $\beta$ 7 strand. Furthermore, the hydroxyl groups of tyrosine side chains in the N0  $\beta$ 4 and  $\beta$ 5 strand form hydrogen bonds with residues of the N1 domain. For example, the conserved residue Y96 and hydroxyl group of Y105 interact with the backbone carbonyl of L134 and the backbone amide of A157, respectively. One polar contact that does not involve hydrophobic residues is the hydrogen bond between D137 of the N1 domain with the backbone amide of K97 located at the end of the  $\beta$ 4 strand.

#### 2.5.2 The N1 domain mediates MxiD<sub>34-171</sub> intermolecular interaction

The N1-N1 domain interface is  $\sim 465 \text{ \AA}^2$ , representing  $\sim 12\%$  of the total interface of one N1 domain in comparison to the N0-N0 interface, which is  $345 \text{ \AA}^2$ , representing  $7\%$  of the total surface area of one N0 domain. The N1  $\beta$ -sheet augments with the N-terminus of the orthologous inner rod protein PrgJ [2]. Furthermore, compared to several hydrogen bonds present between two adjacent N1-N1 domains, only

two residues form a hydrogen bond between N0-N0: Serine 107 and with the backbone of isoleucine 60. Therefore the N1 domain contributes in a higher amount to the oligomerization of the connector than the N0 domain and is furthermore linking the outer basal body components to the inner rod.

Several hydrogen bonds are present between the  $\beta$ -sheet of one N1 domain with the  $\alpha$  helices of the adjacent N1 domain (Figure 27). The  $\beta 7$  and  $\beta 8$  strand contribute to polar interactions while the  $\beta 6$  strand contributes to hydrophobic interface (Figure 23). The loop connecting the  $\beta 4$  and  $\beta 5$  strand of the N0 domain interacts with N1 domain of the adjacent subunit. The conserved D98 forms two hydrogen bonds, one via the backbone carbonyl with the conserved arginine 142 and the other with the side chain with Y151 (Figure 27). Also N100 forms a hydrogen bond with the conserved R142.

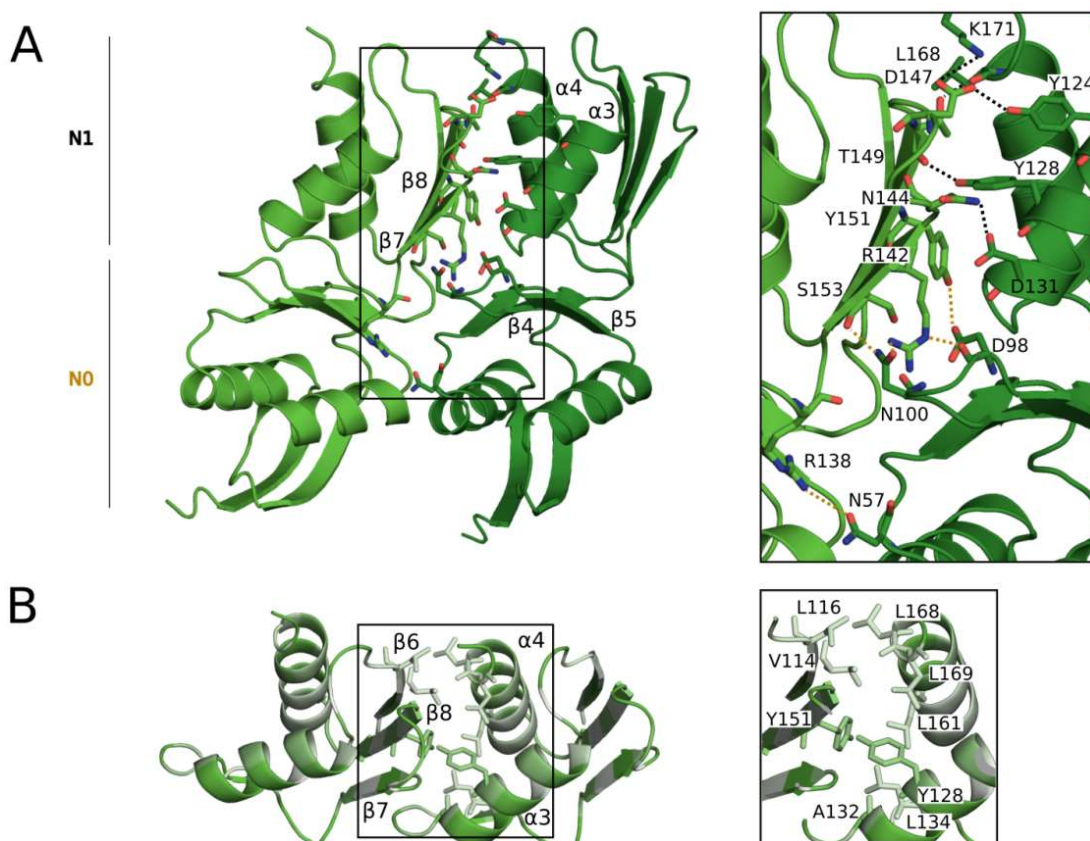


Figure 27: Intermolecular interaction of MxiD<sub>34-171</sub>. Interacting residues are depicted as sticks and labelled, secondary structure elements are assigned. Hydrogen bonds are depicted as dotted lines. A) Polar contacts of two adjacent MxiJ subunits. Hydrogen bonds between residues of the N1 domain only are depicted in black while hydrogen bonds between N0 and N1 residues are coloured in yellow. B) Hydrophobic interaction in the N1 domain. The residues are coloured according to Eisenberg's hydrophobicity scale, white being most hydrophobic. This figure is adapted from Lunelli *et al.*, [55]

Tyrosine side chains contribute also in the N1-N1 interface to polar interactions. Y124 and Y128 of the  $\alpha 3$  helix interact with residues of the loop connecting the  $\beta 7$  with the strand  $\beta 8$ . The only salt bridge present

## 2 Results

in the N1-N1 interface is formed between the side chains of K171 and D147. Only the residues D98 and R142 are conserved, the other bonded residues are of low conservation. Though, hydrophobic residues in both domains are substituted in orthologues by residues of similar physio-chemical properties (Figure 23), indicating that hydrophobic interaction is an evolutionary conserved concept in stabilization of T3SS secretin N0-N1 domains.

### 2.5.3 The connectors of *Shigella* and *Salmonella* comprise similar dimensions

For *Salmonella*, a 15-fold oligomerization of InvG was suggested [68]. Recently, Hu.*et al.* [2] showed that the connector of *Salmonella* comprises a 16-fold symmetry, while the secretin domain still comprises 15-fold symmetry [2]. The 15-meric connector model could not explain the connection of the IM ring to the connector and in N1 and N0 domain, the model-to-map fit was less good compared to the recently published 16-fold *Salmonella* connector model.

The inner and outer diameters of the N1 and N0 (Figure 28) domains in *Salmonella* and *Shigella* vary by  $\sim 5$  Å; though, these differences cannot be considered significant:

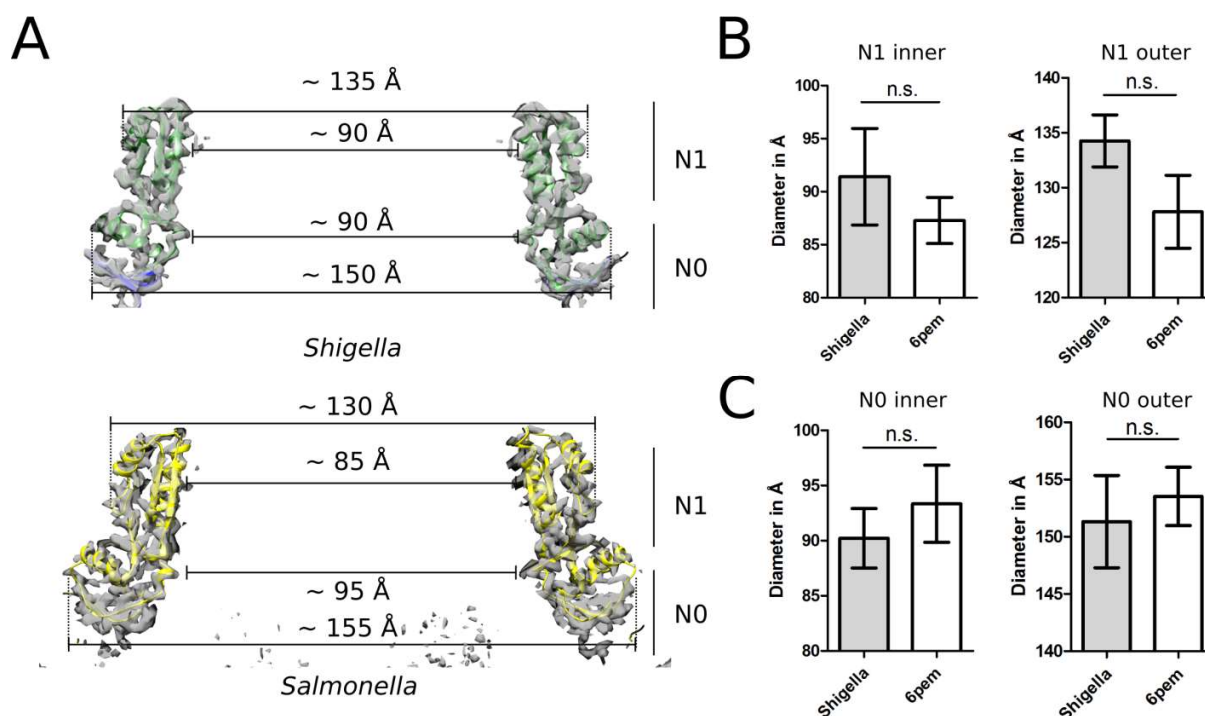


Figure 28: Dimensions of the *Shigella* and *Salmonella* T3SS connector. A) The dimensions and regions used for measurements are indicated. The *Salmonella* model (PDB ID 6PEM) is depicted in its corresponding map (EMDB 20315) at a contour level of 0.08. B) Inner and outer diameter at the N1 domain with two-tailed t-test with min. 4 pairs. The error bars represent the standard deviation of the mean; a p-value of 0.03 was used to test the null-hypothesis. B) Inner and outer dimension of the N0 domain, statistics like in B).

In the 15meric InvG<sub>34-168</sub>(PDB ID 6DV3), a shift in the N0  $\beta$ -sheet facing the IM ring is visible. The  $\beta$ 1 and  $\beta$ 2 strand are located between the N0 helices and the N-terminus of the  $\alpha$ 2 helix is slightly more upwards oriented, in the direction of the  $\beta$ 4 and  $\beta$ 5 strand.

## 2 Results

However, in the recently published 16meric *Salmonella* connector with the 16-fold symmetry, the N0 domain  $\beta$ -strands facing the IM ring superpose well with the 16meric *Shigella* connector, the  $\beta$ 1 strand is located below the  $\alpha$ 1 helix.

Taken together, the MxiD oligomer has a similar dimension in both connector domains, compared to *Salmonella* T3SS. The subdomains N0 and N1 superpose with RMSD of 0.9 and 0.7 in the C $\alpha$  atoms with respective *Salmonella* orthologues (Table 2).

Table 2: C $\alpha$  RMSD of *Shigella* MxiD to *Salmonella* InvG. The query domains are given in the first row. C- $\alpha$  atom deviations were calculated using PDBe Fold v2.59. The structure of Hu *et al.* solved at 3.5 Å (PDB ID 6PEM). This table is adapted from Lunelli *et al.*, [55]

<i>Shigella</i>	<i>Salmonella</i>	domain	% matched residues	RMSD [Å]
<b>MxiD</b> <sub>34-109</sub>	InvG <sub>32-106</sub>	N0	92	0.92
<b>MxiD</b> <sub>110-171</sub>	InvG <sub>107-165</sub>	N1	95	0.74

## 2.6 The apo and the trapped needle complex basal body in comparison

To investigate structural changes in the needle complex upon effector transport, an effector fusion construct (IpaB-knot) was designed. The fusion protein of IpaB and an RNA-methyltransferase from *Thermus thermophilus* (*rrmA*, PDB ID 1IPA) as depicted in Figure 29A, was designed by Dr. Kim Dohlich. The IpaB::*rrmA* fusion protein will be referred to as IpaB-knot. The gene was introduced with an antibiotic resistance cassette in the *Shigella* M90T  $\Delta$ *ipaD* strain by recombineering using FLP recombinase, as described by Datsenko & Wanner, 2000 [47]. Expression under the control of the endogenous virulence promoter in M90T  $\Delta$ *ipaD* resulted in the effector being trapped inside the needle lumen, as proven by TEV protease cleavage assay and immunogold labelling [5]. Furthermore could Dohlich *et al.* show that the *Shigella* strain expressing *IpaB-knot* from the virulence plasmid attenuates the invasiveness to the level of *IpaB* knockout, in comparison to the *Shigella* wild type strain [5].

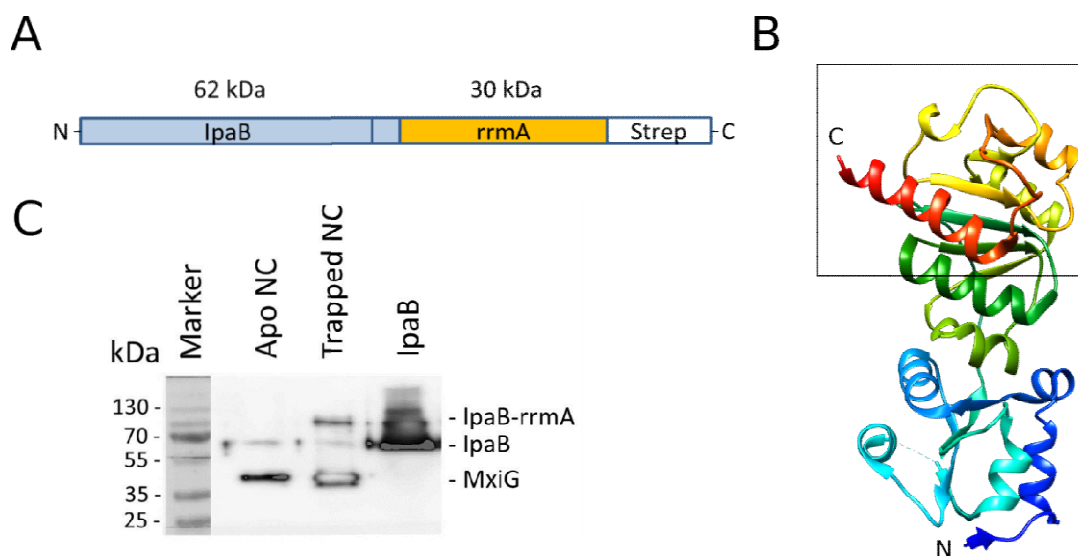


Figure 29 IpaB is fused with the 'trefoil'-knot protein *rrmA* at the C-terminus. A) Schematic depiction of the expression construct IpaB-knot, used to occlude the needle channel. IpaB is connected via a linker to the *rrmA* knot. B) Crystal structure of the RNA methyltransferase (PDB ID 1IPA) in cartoon representation. The C-terminal 'trefoil' knot region is boxed. C) The IpaB-knot fusion protein (IpaB-*rrmA*) is present in isolated needle complexes. A western blot of the Apo NC and the NC trapped with IpaB-knot, MxiG serves as a loading control for the isolated needle complexes. The full-length fusion protein IpaB-knot has a MW of ~94 kDa while IpaB migrates at ~65 kDa. Purified IpaB was used as a control.

## 2 Results

### 2.6.1 Global differences in the dimensions of apo and effector trapped needle complex

The 30 kDa RNA-methyltransferase is reported to form a 'trefoil' knot like structure [70] at the C-terminus (Figure 29) which cannot be unfolded by the sorting platform and therefore causes blocking of the needle channel with IpaB [5]. Western blot analysis of isolated needle complexes using an anti-IpaB antibody showed that the IpaB-knot co-purifies with the needle complex (Figure 29). Full-length IpaB migrating at ~62 kDa is visible in the apo and the trapped NC. In case of the fusion protein it could either be an artefact of the western blot or a degradation product of the IpaB-knot protein.

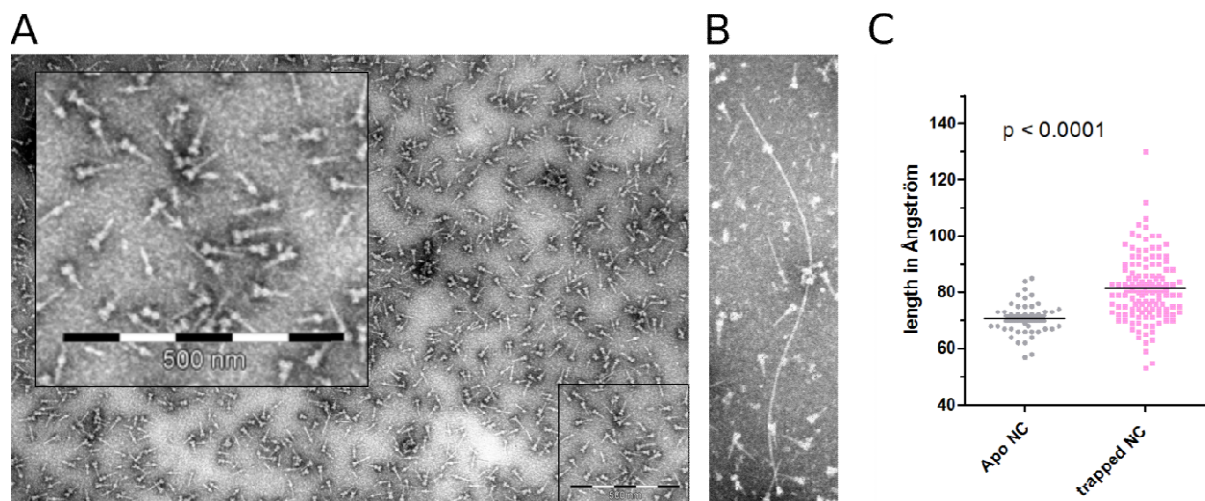


Figure 30: Trapped needle complexes can form extended needles. A) Negative stain TEM image of apo needle complexes B) Negative stain image of trapped needle complexes C) Statistical analysis of PTA-stained apo NC and trapped NC. 40 pairs were used for the two-sided t-test. The mean length is ~ 70 nm for the apo and ~80 nm for the trapped NC.

Effector trapped needle complexes showed the ability to form longer needles than apo needle complexes, as detected in negative stain TEM imaging (Figure 30). For statistical analysis, TEM images with evenly distributed particles were subjected to image analysis, excluding manually particles from the dataset that were overlaying or degraded. The mean length of the apo needle detected in TEM microscopy is ~ 70 nm. It was reported that the needle length of the needle varies and was suggested to be ~ 60-80 nm for *Salmonella* [68, 71]. The TEM imaging results of isolated *Shigella* needle complexes would be in the range of reported needle length, shorter needles could be caused by broken needle filaments. The resolution limit for this technique is ~ 1.5 nm [46].

The effector trapped needle showed the ability to form extended needle filaments (Figure 30B, C). The effector trapped in the needle channel lumen could act as a stabilizer, reducing needle shredding due to mechanical stress. MxiH has been shown to polymerize *in vitro*, therefore disassembled subunits of MxiH in the sample could polymerize on top of present needles, forming extended needle filaments (Figure 30) [72]. In TEM imaging and in the structural model, the mean diameter at the IM ring is for both, apo and trapped needle complex  $\sim 25$  nm, which is in good agreement with other models of *Shigella* [73] and orthologous T3SS structures from *Salmonella* SPI-1 system [53, 68], *Yersinia* [74] and *E. coli* [75].

Also the unsymmetrized C1 maps of apo and effector trapped needle complexes reveal their similar overall dimension (Figure 31A, B)

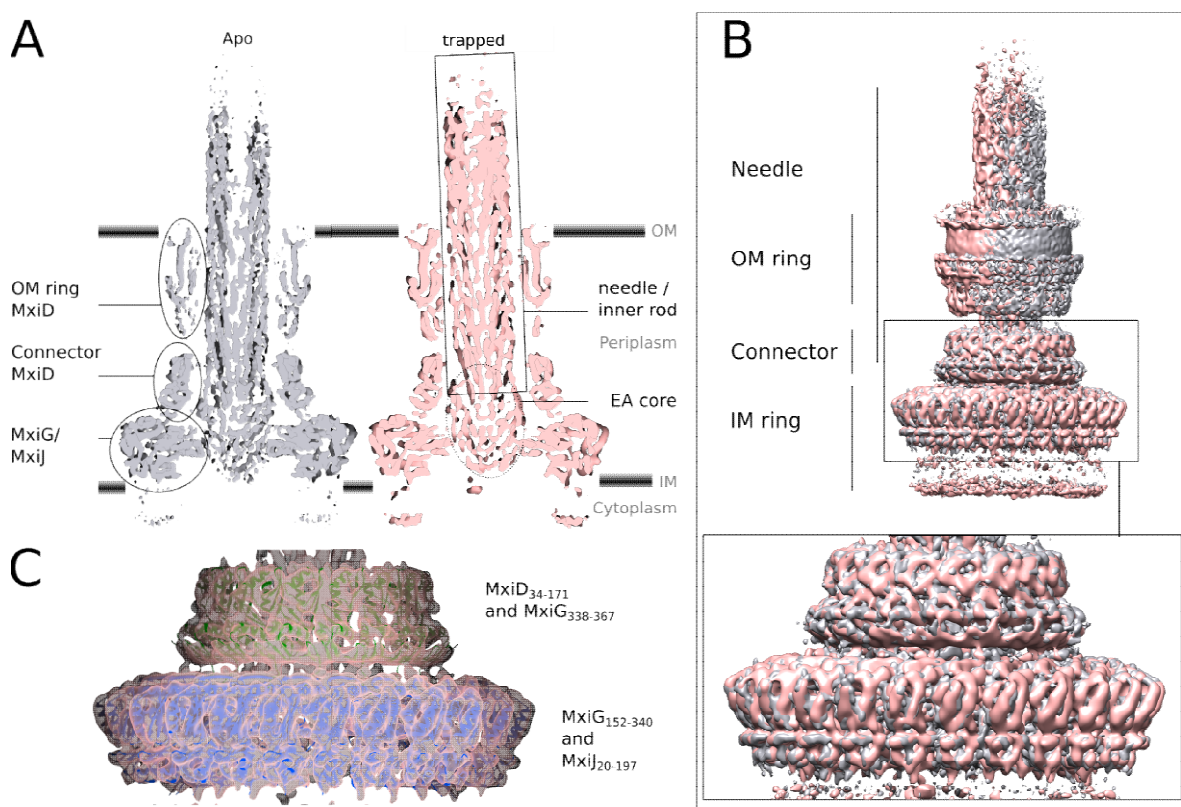


Figure 31: Unsymmetrized C1 maps of the apo and effector trapped needle complex with resolutions of 5.1 Å and 6.5Å, resp. The apo NC is depicted at a threshold of 0.078 and the trapped NC at 0.037 A) Vertical slices of the maps. The respective regions of interest are indicated. EA – export apparatus; OM – outer membrane; IM – inner membrane B) Superposition of both maps. The connector and the IM ring region superpose well. C) The connector and IM ring models built in the respective post-refined symmetrized maps of the trapped needle complex, fitted into the C1 map.

The maps were superposed in Chimera at the indicated threshold, which allowed detection of relevant features and taking the IM ring MxiG triade in consideration. Since superposition is dominated by

## 2 Results

the well-resolved IM ring, turning the map by one and two MxiG subunit results in a density mismatch in the connector domain and a cross-correlation lowered from 0.93 to 0.91. The C1 maps were used to fit the atomic models built in the symmetrised, higher resolution maps, to investigate reorientation of the inner membrane ring and the connector respectively to each other (chapter 2.6.3 Minor changes in the MxiG D2  $\beta$ -sheet and the MxiJ loops facing the export apparatus and chapter 2.6.4 The structures of the connectors and their interactions are very similar). The distance between the IM ring and the connector remained the same and also connection at the  $\beta$ -sheet augmentation site (Figure 36), indicating that very little changes occur in the needle complex base upon effector transport.

### 2.6.2 Density differences in the needle lumen and the export apparatus core

To avoid averaging out details upon refinement applying symmetries, the unsymmetrized C1 maps of the apo and effector trapped needle complexes at 5.1 Å and 6.5 Å were used for global density comparison. A needle tilt is visible in both C1 maps, making a superposition of the needle volumes difficult. Therefore the needle volumes were extracted, segmenting the trapped needle complex C1 at low threshold levels and stripping off the outer basal body components. The remaining central unit of export apparatus, inner rod and needle was resampled on the initial map and used as a mask for the apo C1 map. The threshold levels for both C1 maps were chosen as low as possible, before noise density around the needle complex was visible. The resulting extracted maps of the central needle, inner rod and export apparatus core were superposed and sliced at the centre (Figure 32).

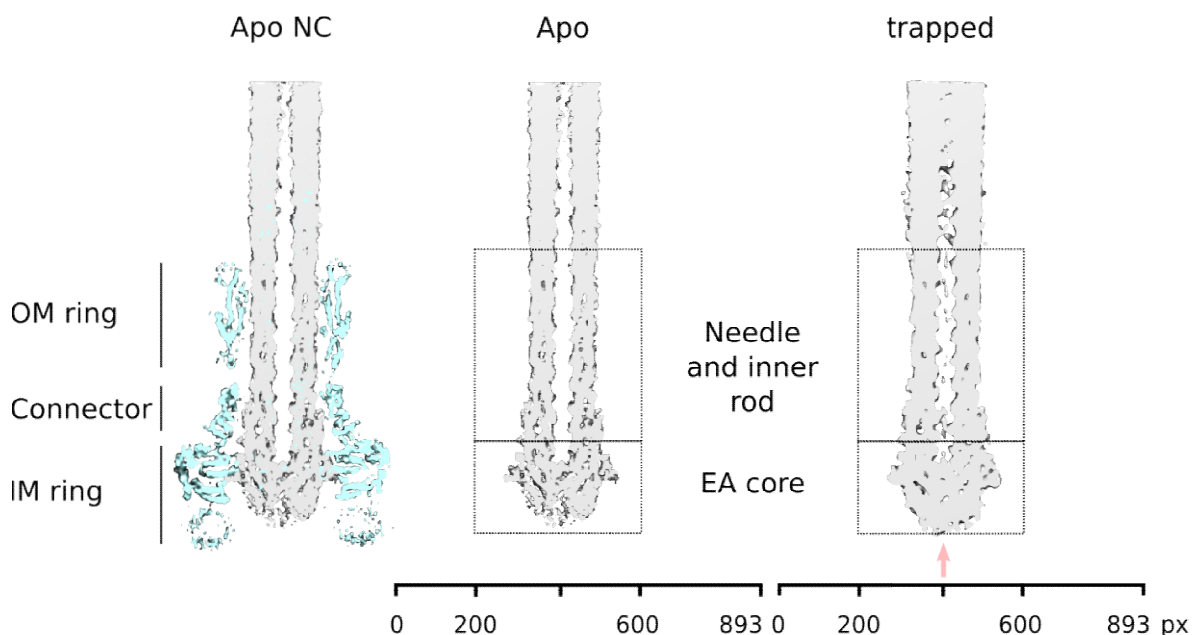


Figure 32: Vertical central cross section of needle, inner rod and export apparatus core of post-refined C1 maps of apo needle complexes and effector trapped needle complexes. The OM ring, connector and IM ring of the apo needle complex are depicted in light blue on the left hand side, at a higher threshold. Additional densities are visible in the effector trapped C1 map in the needle lumen and the export apparatus (EA) at low threshold levels. The density distribution in regions indicated with a box were analysed and are depicted in Figure 33. The additional density visible in the needle lumen at  $\sim 400 - 420$  px is indicated with a rose arrow.

As visible in Figure 32, additional density features in the needle lumen and at the bottom of the export apparatus core are visible at low threshold levels in the cryo-EM map of the trapped needle complex. Plotting the relative density of the respective regions indicated in Figure 32 over the pixels of the images, an extra density is visible at the centre of the needle lumen, highlighted with rose. The density distribution at the export apparatus core looks rather inhomogeneous. This area of the maps is also of low resolution, especially at the bottom of the export apparatus, the data have to be taken with caution. Though, in the area of the export apparatus core, the trapped NC map shows approximately  $1/3$  more density is detectable than in the apo form (Figure 33).

## 2 Results

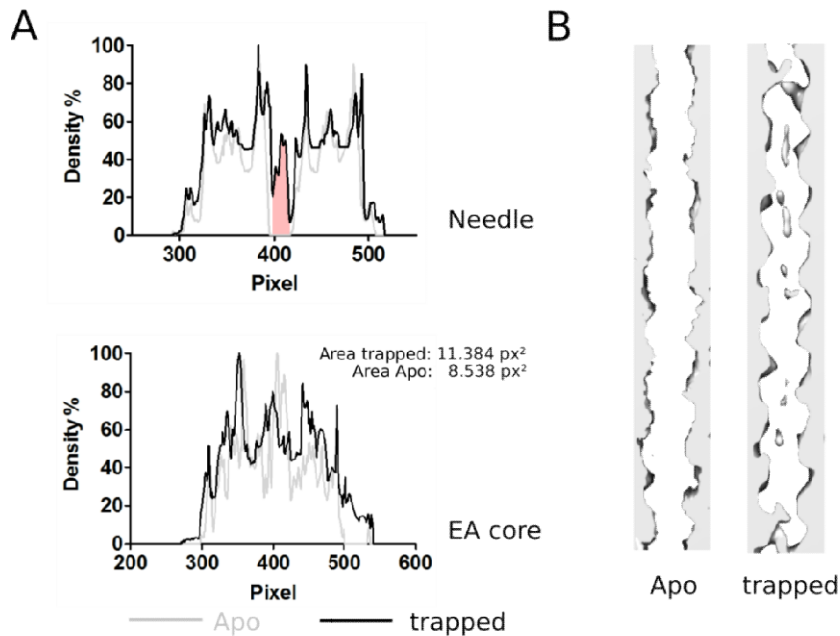


Figure 33: Density differences in post refined C1 maps of effector trapped and apo needle complexes. A) Relative density distribution of slices of apo and trapped NC maps indicated in Figure 32. The density difference in the needle lumen at ~400 – 430 px is highlighted with rose. B) Enlarged image of the needle lumen of the respective maps.

A TEV protection assay has shown on the IpaB-fusion protein has shown that a TEV cleavage site present between the C-terminal knot and the N-terminal IpaB, is shielded from TEV protease processing due to coverage of the cleavage site in the needle lumen [5]. Taking the results for *Salmonella* and *Shigella* on the effector trapped needle complex into consideration [5, 71], we could assume that the additional densities visible in the needle lumen of the trapped NC C1 map could be assigned to the at least partially unfolded IpaB effector of IpaB-knot. The additional density feature at the bottom of the export apparatus could be assigned to the C-terminal region of the IpaB-knot, representing maybe the knot. Though, since the export apparatus is rather unstable and it is not clear how many subunits are present at the bottom of the export apparatus core, the density could be assigned to a subunit of the export apparatus [21, 61].

SsNMR studies revealed a T3SS needle lumen of ~ 20 to 25 Å, with an altering negative and positive surface pattern, following the helical arrangement of needle subunits [72]. This diameter would be too

small to accommodate fully folded proteins, therefore it was suggested that the proteins traversing the channel have to be at least partially unfolded to allow passage through the needle lumen [71].

The unfolded amino acid chain of IpaB would be approximately 250 nm long, considering the 580 amino acids of IpaB and the average bond length of N-C, C-C and the N-O peptide bond (1.47 Å, 1.53 Å and 1.32 Å, respectively). Studies suggest that the unfolded effector follows a spiral way through the needle lumen [68], along the polarity pattern formed by three charged C-terminal residues of the needle protein MxiH, K66, D70 and R80[36, 72]. Considering the ~ 2.4 nm helical pitch  $H$  and a ~ 2 nm inner diameter  $D$  of the *Shigella* needle [76] (PDB ID 2MME), an amino acid chain with a total length  $T$  of 250 nm that would follow the helical pattern of the needle could curl up to a helix-like structure with a length of ~ 89 nm at the longitudinal axial  $L$ .

$$L = \frac{T}{\sqrt{H^2 + \pi D^2}} * H$$

The ~ 89 nm of unfolded IpaB helix-like model represent an approximation and does not include repulsion by side chains, which could lead to a much longer structure present in the needle lumen. It is not to be confused with an  $\alpha$ -helix, which is stabilized by backbone hydrogen bonds. Considering IpaB an  $\alpha$ -helical protein with a helical pitch of 0.54 nm and an average diameter of 1.2 nm (averaging side chains), the actual length of the  $\alpha$ -helix would be ~ 62 nm. This length would not be enough to cross the needle lumen.

Since Dohlich *et al.* [5] could show that the N-terminus of IpaB-knot fusion protein is sticking out from the needle tip, an unfolding of this protein in the needle lumen is likely. The N-terminus of the effector sticking out from the needle tip might assist in the attachment and auto-assembly of MxiH subunits on the needle, leading to extended needle filaments visible in Figure 30B.

## 2 Results

### 2.6.3 Minor changes in the MxiG D2 $\beta$ -sheet and the MxiJ loops facing the export apparatus

To analyse changes in the orientation of the connector and the IM ring respectively to each other, the models refined in their respective symmetrised maps, were fitted in the C1 maps as rigid bodies with Chimera, combined and superimposed. As visible in Figure 34A, the IM ring and the connector of the apo and effector trapped needle complex have a very similar orientation. This could either be caused by full rotation of the connector or IM ring of 3 MxiG subunits or no rotational twist occurring between the two components. Since the space between the IM ring and the connector is in both maps  $\sim 15 - 20 \text{ \AA}$ , the rotational freedom allowed by the C-terminal MxiG stretch 338-348 would be  $\sim 22.5 \text{ \AA}$ , corresponding of a turn of the connector of 1 MxiG subunit.

The IM ring subunits do only exhibit very minor rotational rearrangement respectively to each other. The difference in C $\alpha$  atom position in the MxiJ  $i+1$  helix 4 is  $1.0 - 1.2 \text{ \AA}$ , structurally aligning IM ring tetramers consisting of two MxiG and two MxiJ subunits on the MxiG chain  $i$ . Figure 34B.

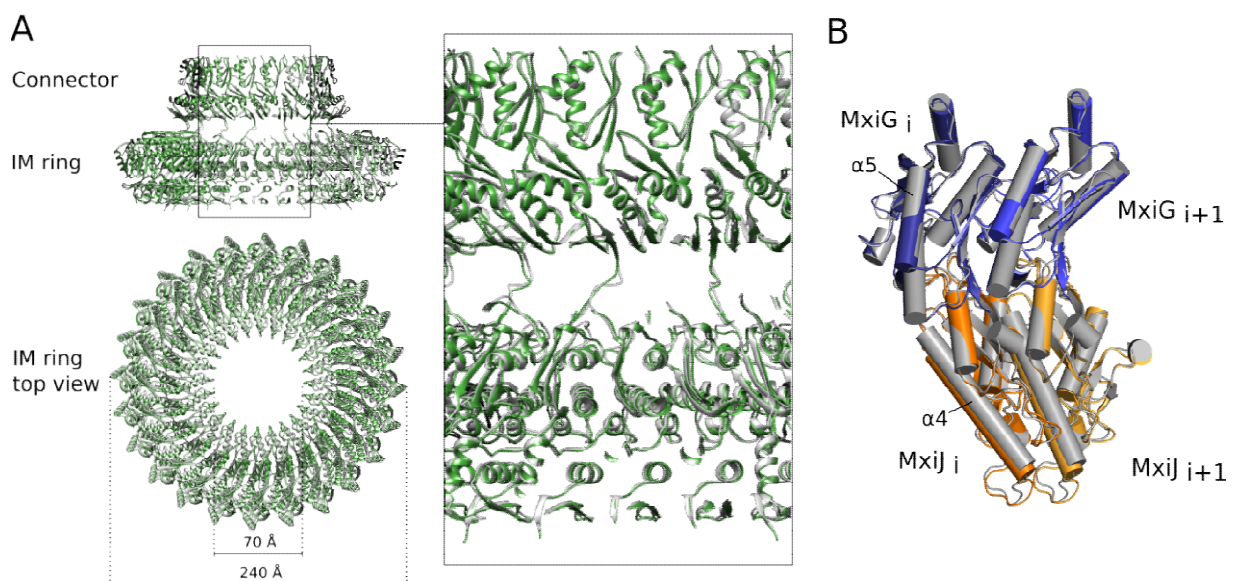


Figure 34: Superposition of the IM ring and connector models of the apo and effector trapped needle complex. A) The trapped needle complex models of the IM ring and the connector fitted in their respective maps and structurally superimposed. The trapped NC is depicted in green, while the apo models are depicted in grey. A central cropped side view is depicted on top and a  $90^\circ$  rotation around the x axis in the lower panel. No rotational reorientation of the IM ring with regards to the connector is visible. B) Top view on global superposition of IM ring tetramers, formed by two neighbouring MxiG and MxiJ subunits. The superposition is based on the MxiG subunit  $i$ . Helices are depicted as cylinders; the trapped model is coloured while the apo model is depicted in grey.

Though side chain density is visible in most areas of the effector trapped cryo-EM map, the reorientation of subunits identified with this initial test should be considered with caution, considering the overall map resolution of 3.9 Å. Normal mode analysis might help to decipher biological relevant rotational rearrangements of the subunits in the apo and effector trapped needle complex.

The MxiG-MxiG interface is ~ 2% smaller than the apo form (877 Å<sup>2</sup> compared to 897 Å<sup>2</sup>) and like in the apo form, only few residues interact with their long side chains with the neighbouring MxiG subunit.

To check the rearrangement of protein backbone, ProSmart analysis was performed using fragments of nine amino acids length for global alignment and colouring the structure according to the hinging score, which considers rotational reorientation of residues at the centre of the aligned fragments.

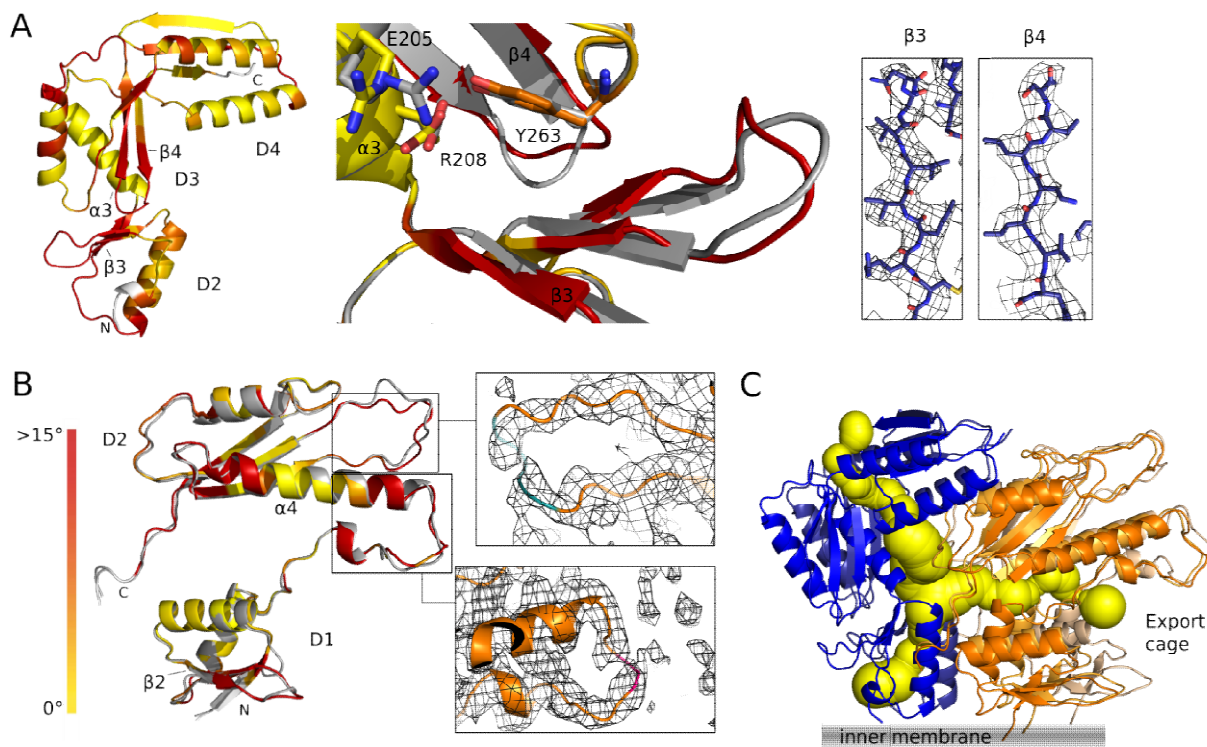


Figure 35: Structural changes in MxiG and MxiJ. A) MxiG subunits of the trapped NC coloured with the ProSmart hinging score. The backbone of the D2 and D3 domain of the trapped and apo NC MxiG (apo coloured in grey) are depicted next to it. The  $\beta_3$  and  $\beta_4$  strands of the trapped NC are depicted in the density map. B) MxiJ model of the trapped NC coloured according to ProSmart hinging score, MxiJ of the apo NC coloured in grey. The upper and lower loop facing the export apparatus are depicted in the density. The region of polar residues in the upper loop are coloured in light blue, the region with hydrophobic residues of the lower loop are coloured in hot pink. Density of the export apparatus is visible on the right side of the enlarged lower MxiJ loop in the density. C) The IM ring of the trapped channel possesses channels connecting the periplasm with the export cage. The channel is coloured in yellow, the MxiG and MxiJ subunits in blue and orange, respectively.

## 2 Results

Despite a lot regions were assigned with rotational change  $>15^\circ$ , the backbone superpose well in most ( $C\alpha$  RMSD of 0.75 Å). The largest variation is visible in the  $\beta$ -sheet of the D2 and the linker of the  $\beta$ 4 and  $\beta$ 5 strand (Figure 34), while the  $\alpha$ -helices remain stable. The D2  $\beta$ -sheet twisted slightly upwards, towards the D3 domain. The conserved residue Y263, part of the linker between the  $\alpha$ 4 helix and the  $\beta$ 6 strand, remained in the same position and the side chain is covered by density. The side chains of E205 and R208 moved slightly away from Y263, though, in this area the density is lower, and the position of two residues have to be taken with caution. The density of other regions of MxiG, for instance the  $\beta$ 3 and  $\beta$ 4 strands, are defined and backbone tracing is possible (Figure 35).

In MxiJ, only the loops connecting the secondary structure elements show variation, the RMSD of both subunits in the  $C\alpha$  atoms is 0.98 Å (Figure 35). Most structural changes occur in the loops facing the export apparatus, though, the region of the upper loop with charged and polar side chains (EEKN, amino acids 136-139) and the hydrophobic tip of the lower loop are still pointing in the direction of the export apparatus (Figure 35). Again, due to low density in the region of the upper loop, the coordinate position of the  $C\alpha$  atoms should be taken with caution. Comparing the C1 maps, the distance of the lower loop to the export apparatus is similar, suggesting that the putative hydrophobic interaction with the export apparatus is maintained.

The interface area between two neighbouring MxiJ subunits remained the same,  $\sim 2660 \text{ \AA}^2$ . Polar side chain interactions are very similar, for example the polar pod-socket interaction in the D2 domain discussed in chapter 2.3.5. MxiJ subunits are connected by polar and hydrophobic interactions is still present and mediated by the same residues.

Like in the apo needle complex, channels traverse in the inner membrane ring of the effector trapped needle complex. Two MxiG subunits and three MxiJ subunits form a channel (Figure 35C). The channel exit B, constituted by the D2-D3 interface in the apo needle complex, is positioned between the D2 domains in the trapped needle complex.

### 2.6.4 The structures of the connectors and their interactions are very similar

The connector of the trapped needle complex superposed well with the apo form of the connector. The C $\alpha$  RMSD of MxiD<sub>37-171</sub> is 0.58 Å. For the two neighbouring augmenting MxiG  $\beta$ -sheets, the C $\alpha$  RMSD is 0.35 Å and 0.75 Å, respectively, considering only the amino acid 348-367 forming the  $\beta$ -sheet (Figure 36). The interface between MxiD subunits is 1027 Å<sup>2</sup>, which is ~12 – 13% of the total MxiD<sub>37-171</sub> surface, similar to the apo form. Though the side chain orientation has to be taken with caution at a map resolution of 4.2 Å, MxiD-MxiD polar interaction is mediated by mostly the same residues. For instance, the salt bridge between lysine 171 and aspartate 147 is still present and the hydrogen bonds between tyrosine 124 with aspartate 147 and leucine 168 to threonine 149. Asparagine 100 is still hydrogen bonded to serine 153 but in the side chain instead of the backbone, mediating N0 – N1 interaction. Most backbone variation is visible in the region of the MxiD  $\beta$ 7 stand (amino acids 135-146) (Figure 36). This region comprises the conserved arginine 142, which can also form a hydrogen bond with asparagine 100 of the neighbouring subunit in the apo NC. In the trapped NC, the arginine 142 side chain has a similar orientation, but the H-bond donor-acceptor distance to asparagine 100 is larger than 4.0 Å. The backbone carbonyl group of proline 140 though can form a hydrogen bond with asparagine 100 of the neighbouring subunit and could contribute to inter MxiD subunit stabilization.

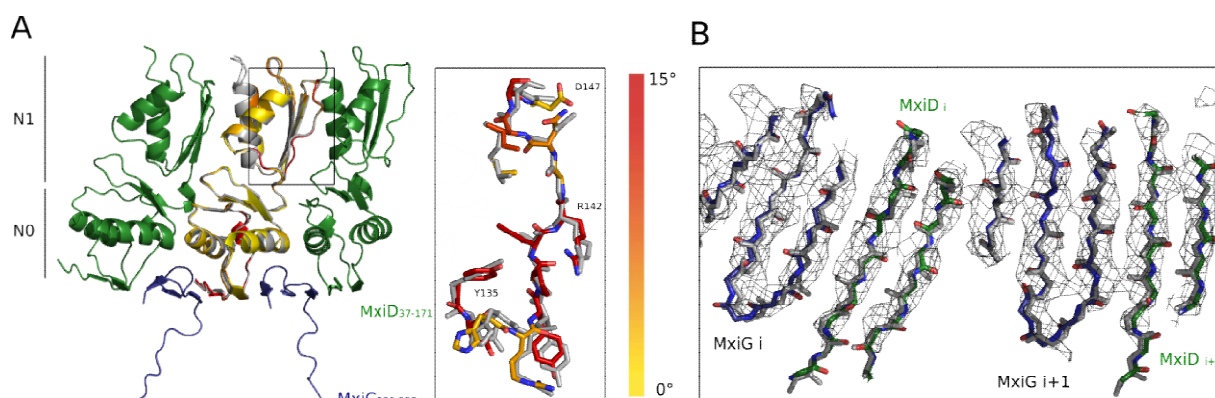


Figure 36: Connector of the trapped NC. A) 3 MxiD subunits and two C-termini of MxiG. The N0 and N1 domain of MxiD are assigned. The central One MxiD subunit is coloured with the ProSmart hinging score and superposed with the apo MxiD connector model depicted in grey. According to the hinging score, most backbone deviations occur in the N1 domain, from residue 135-147, depicted in the box in stick representation. This region comprises the in the  $\beta$ 7-strand, with the conserved residue R142 located in the centre. B) Top view of the OM ring – IM ring  $\beta$ -sheet augmentation. The model of the apo needle complex is depicted in grey.

## 2 Results

In the centre of the MxiD  $\beta 7$  strand, the formation of backbone hydrogen bonds with the neighbouring  $\beta 8$  strand is possible, between tyrosine 151 and arginine 142 (Figure 37). Though the donor-acceptor distances are for some residues  $> 3.5 \text{ \AA}$  (N144, P140), the phi and psi angles of the residues 139-143 are in the  $\beta$ -strand conformation (Figure 37). The  $\beta 7$  strand is in both models, of the apo and trapped NC, involved in the formation of the N1  $\beta$ -sheet and in polar inter-subunit interactions. The  $\beta 8$  and  $\beta 9$  strand of the N1  $\beta$ -sheet also contribute by their hydrophobic interface to inter subunit stability.

Other regions showing variations in the protein backbone are the MxiD stretch in the N0 domain, between  $\beta 2$  and  $\beta 3$  strand, which is not involved in intra- or inter-subunit contacts, and the stretch of MxiG connecting the periplasmic IM ring with the C-terminal  $\beta$ -sheets (MxiG 338-347), a region of low cryo-EM density in both, the apo and trapped NC map.

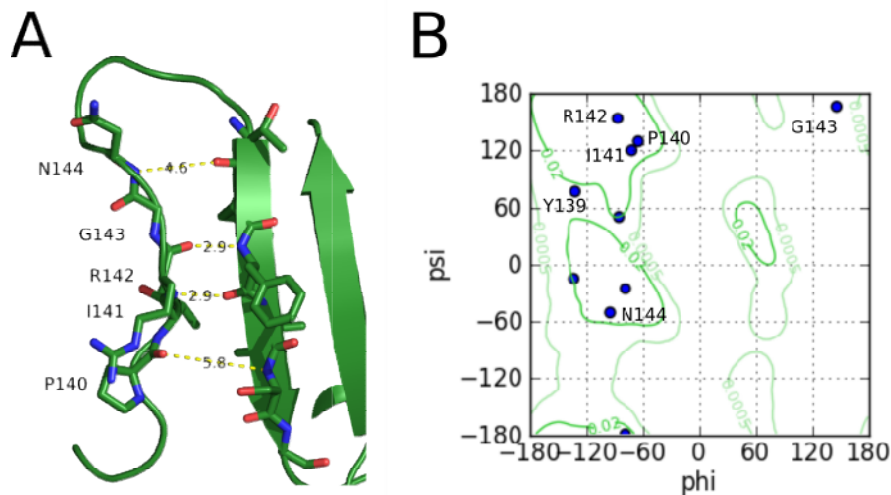


Figure 37: The MxiD  $\beta 7$  strand of the trapped NC. A) Distances between putative hydrogen bond donors and acceptors in the  $\beta 7$  and  $\beta 8$  strand of the N1 domain. The residues of the  $\beta 7$  strand are assigned and depicted as sticks. B) Ramachandran plot MxiD 136-147. Residues of the  $\beta 7$  strand and N- and C-terminal residues are indicated. The region for residues in the  $\beta$ -strand conformation is approximately in the upper left quarter, with it energetically preferred centre at  $\sim \psi 135^\circ$  and  $\phi -135^\circ$ .

Overall, it seems that the inner membrane ring and the connector do not undergo major rearrangements upon effector transport but remain stable in their dimensions, structure and orientation. Changes could occur in the export apparatus the needle lumen but require further investigation.

## 2.7 Validation of the atomic models

Table 3: Cryo-EM data collection, refinement and validation statistics. \*) MxiG<sub>152-340</sub> and MxiJ<sub>21-197</sub> \*\*) MxiD<sub>34-171</sub> and MxiG<sub>338-367</sub> \*\*\*) MxiG<sub>152-340</sub> and MxiJ<sub>20-197</sub>

	Apo needle complex		Effector trapped needle complex	
	IM ring (EMD-10045)	Connector & IM ring (EMD-10040)	IM ring	Connector & IM ring
<b>Data collection and processing</b>				
Magnification	100,000	100,000	101449	101449
Voltage (kV)	300	300	300	300
Electron exposure (e <sup>-</sup> Å <sup>-2</sup> )	25	25	25	25
Defocus range (µm)	1.5 – 4	1.5 – 4	-2 - -4.5	-2 - -4.5
Pixel size (Å)	1.38	1.38	1.38	1.38
Symmetry imposed	C24	C8	C24	C8
Initial particle images (no.)	171,833	171,833	173080	173080
Final particle images (no.)	72,298	72,298	53,954	53,954
Map resolution (Å)	3.6	3.9	4.0	4.2
FSC threshold	0.143	0.143	0.143	0.143
Map sharpening <i>B</i> factor (Å <sup>2</sup> )	-140	-120	-191	-140
Model Refinement	IM periplasmic ring*, PDB ID 6RWX	Connector **, PDB ID 6RWK	IM periplasmic ring***	Connector **
Model resolution (Å)	3.5	3.7	4.1	4.2
FSC threshold	0.5	0.5	0.5	0.5
<b>Model composition</b>				
Non-hydrogen atoms	70,968	21,760	71,184	21,760
Protein residues	8,784	2,688	8808	2688
R.m.s. deviations				
Bond lengths (Å)	0.009	0.007	0.001	0.001
Bond angles (°)	1.17	0.75	1.017	0.989
Model validation				
MolProbity score	1.62	2.84	1.99	1.90
Clashscore	3.35	14.06	7.83	7.80
Poor rotamers (%)	0.00	5.83	0.00	0.00
Ramachandran plot				
Favored (%)	91.71	87.80	89.69	92.38
Allowed (%)	8.29	12.20	10.31	7.62
Disallowed (%)	0.00	0.00	0.00	0.00
EM ringer score	3.02	3.50	1.44	1.78
CCmask	0.83	0.85	0.78	0.76

As depicted in Table 3, both Apo models have 0 Ramachandran outliers and a cross-correlation with the maps above 0.8. The connector has 6% poor rotamers and a clash score in the lower two-digit range.

## 2 Results

While the clash score of the IM ring model is in the 97<sup>th</sup> percentile, the connector is in the 57<sup>th</sup> percentile. The atoms of the connector affected by an overlap of their Van-der-Waals-radii of more than 0.4 Å are for example in the side chains of Serine 47 with arginine 51 of the same chain, Y38 and R51 and I60 with L102. All side chains mentioned interact and are covered by density. Side chain flips suggested by the MolProbity report of the connector model involve Q65, N100 and N144. The Q65 side chain amine is hydrogen bonded with the side chain carbonyl of E109. The N100 side chain is coordinated by serine 153 with the backbone carbonyl and hydroxyl group and the arginine 142 side chain amide. The asparagine 144 side chain is coordinated by the aspartate 131 side chain and the backbone amide groups of serine 146 and isoleucine 145. The resolution of the models was estimated using the cross-correlation at FSC 0.5 of the model against the full map. The respective values are listed in Table 3.

As suggested by Brown *et al.* [77], the models were tested for overfitting against noise using the Fourier shell correlation of the model against the odd and even half maps. The randomized coordinates of model were refined in a map that contained one half of the information of the full map (“half map 1” with FSC work). The fit of the model refined in the first half map in the second half map is represented by the FSCtest. For all 4 models, the FSCtest and FSCwork curves progress close to each other (Figure 38, Figure 39).

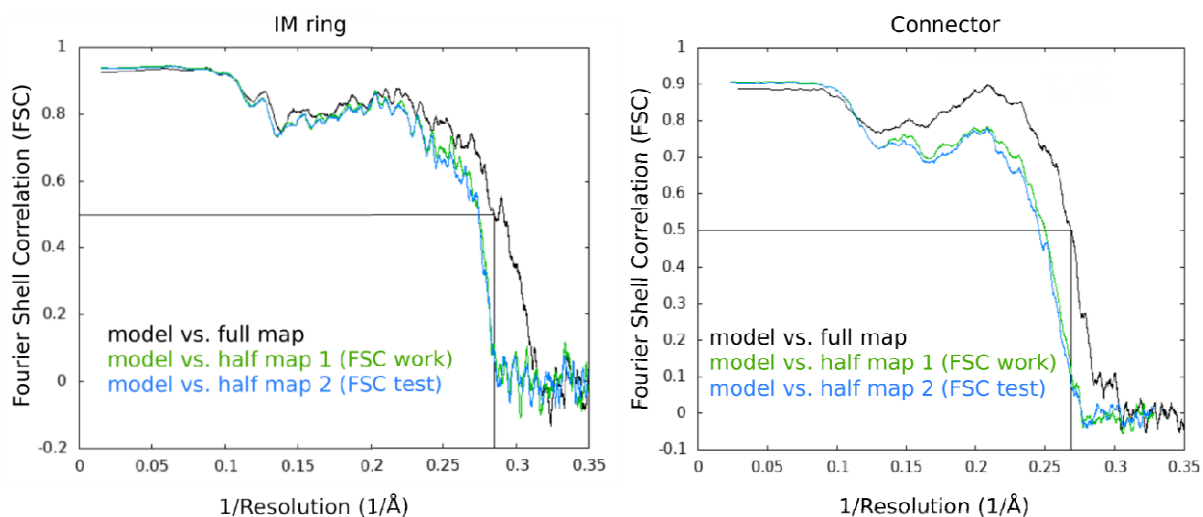


Figure 38: Fourier shell correlation curves of the atomic models of the apo IM ring and the connector with their respective maps. The model resolutions of the maps at FSC 0.5 are 3.5Å for the IM ring and 3.7Å for the connector. This figure is adapted from Lunelli *et al.*, [55]

The resolution limit applied upon refinement was around the 3.2 – 3.5 for the apo IM ring and for the substrate trapped needle complex the resolution of the map given after post-processing. Since no sharp decrease at the resolution limit that was applied upon refinement is visible for both models, the models are most likely not fitted against noise. As indicated in Figure 35 and Figure 36, the backbone of the trapped model fits the density nicely and the model meets general geometry requirements, as indicated by the 0 % Ramachandran outliers, bond and angle restraint outliers (see Table 3).

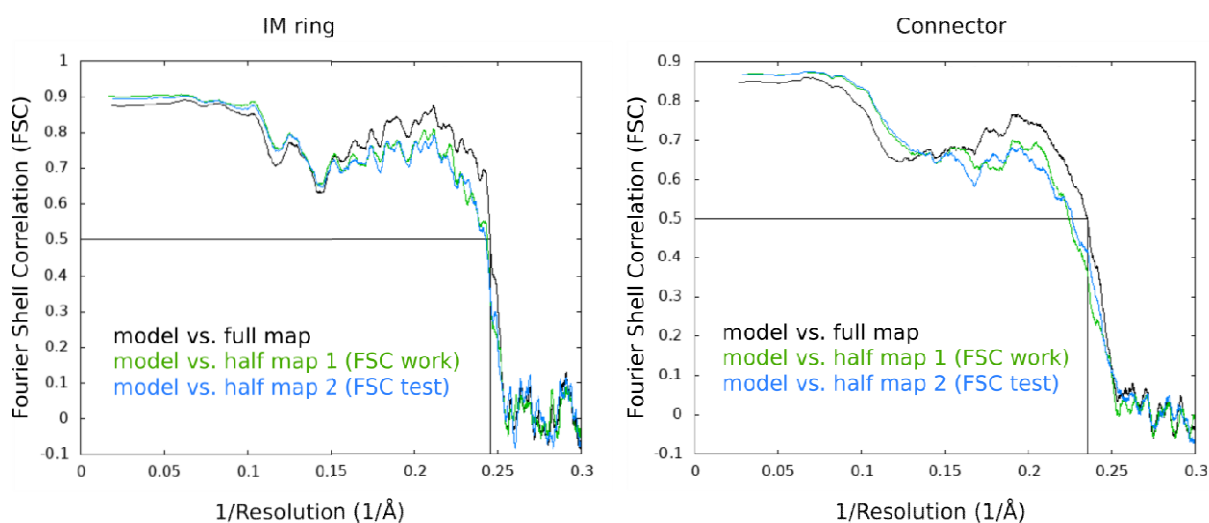


Figure 39: Fourier Shell Correlation curves of the atomic models of the trapped NC with their respective maps. The model resolution at 0.5 FSC is 4.1 for the IM ring and 4.2 for the connector. The resolution cut-off applied upon refinement was 4.0 for the IM ring and 4.2 for the Connector. This figure is adapted from Lunelli *et al.*, [55]

## 3 Discussion and perspectives

The T3SS is a bacterial transmembrane complex with approximately 20 structural proteins constituting the machinery for protein transport across membranes [19]. Extensive research led to several suggestions on how this complex machinery assembles [2, 28, 45, 68, 78]; nevertheless, many questions remain unanswered. Though it is assumed that all the proteins that constitute the basal body are known, the structures of the core components of the *Shigella* basal body, forming the inner and outer membrane ring, were unknown. Additionally, their contribution to effector secretion was not clear.

The aim of this study was to analyze structural changes of the *Shigella* T3SS needle complex basal body, in two different states, apo and trapped with an effector. To address this question, the needle complexes were isolated from *Shigella flexneri*. Near-atom cryo-EM maps generated by Dr. Michele Lunelli allowed building and refinement of basal body components, based on homology models. The structure of the periplasmic domains of the apo needle complex IM ring, constituted by the proteins MxiJ and MxiG, was refined to 3.5 Å. The apo needle complex connector domain, constituted of MxiD and the C-terminus of MxiG, was refined to 3.7 Å. For the needle complex trapped with an effector, the respective structures could be refined to 4.1 Å and 4.2 Å.

By interpreting the maps, the structural model of the connection between the IM and the OM ring could be built. The structural model was not known for *Shigella* and only recently published for *Salmonella* [2]. Fluorescence microscopy experiments suggest that the MxiG C-terminus, forming the OM-IM ring connection, is required for the formation of intact needle complexes (chapter 2.4.3 MxiD and MxiG  $\beta$ -sheet augmentation is essential for needle formation). Furthermore, channels in the IM ring were identified and analyzed (chapter 2.3.2 The inner membrane ring is channelled). Conserved residues, located nearby a local channel minimum could be identified and analyzed using fluorescence microscopy and protein complex isolation combined with TEM imaging, secretion and invasion assays. MxiG residues essential for needle complex functionality (R208) and stability (E205, Y263) could be identified (chapter 2.3.3 Mutational analysis of conserved channel residues). The conserved lower loop of MxiJ, harboring a hydrophobic tip facing the central export apparatus, might form a focal point for the

formation of the IM ring, as suggested in earlier studies [2] (chapter 2.3.5 MxiJ subunits are connected by polar and hydrophobic interactions). It seems that, upon effector transport, the structure of the IM ring and connector does not undergo major structural rearrangements but remains rather rigid and only minor conformational changes occur in the backbone atoms of IM ring subunits (Chapter 2.6.3 Minor changes in the MxiG D2  $\beta$ -sheet and the MxiJ loops facing the export apparatus).

#### 3.1 Symmetries and dimensions of the *Shigella* T3SS needle complex in comparison to orthologues

The shape and overall dimensions of ~80 nm length and ~25 nm width of the apo needle complex analyzed in this study matches well the previous reconstructions from negatively stained isolated particles and *in situ* structures of *Shigella* T3SS [74, 79] and of the *Salmonella* SPI-1 system determined at near-atomic resolution [2, 53]. In tomography studies though, the *Shigella* needle complex basal body appears to be ~31 Å in length, in comparison to ~ 25 Å from models of isolated needle complexes [74, 80, 81]. This could either be related to structural changes occurring upon needle complex isolation or be related to the rather low resolution of ~ 2.7 nm of the cryo-tomography study in *Shigella*.

The 24-fold rotational symmetry of the *Shigella* IM ring is in good agreement with other studies in *Shigella* [73], the *Salmonella* SPI-1 system [2, 53], *Yersinia* [74] and *E. coli* [75]. The previously suggested 12-fold symmetry for the *Shigella* IM ring, however, could not be confirmed by our analysis, which might be due to the negative staining or the limited resolution of the previous study [79]. Additionally, the 16-fold symmetry of the connector and the 15-fold symmetry of the secretin domain could be detected in recent *Salmonella* studies [2].

This leads to the assumption that T3SS needle complexes are structurally well conserved. Determining the number of subunits forming the inner rod and the composition of cytoplasmic sorting platform remains difficult though, since the T3SS is a highly dynamic and flexible transmembrane complex. Proteins associated with the T3SS that are visible in tomography studies but lost upon purification, like the export protein MxiA, play an important role in the assembly and function of the T3SS. Recent mass spectrometry data from our lab identified MxiA peptides associated in low amounts to

### 3 Discussion and perspectives

isolated, cross-linked T3SS needle complexes. Therefore the Kolbe lab and in particular Lara Flacht is in the process of combining *in vivo* crosslinking and subsequent analysis to contribute to clarification of the above mentioned points.

#### 3.2 Outer membrane and inner membrane ring interact via $\beta$ -sheet augmentation

To interact with the 16-fold symmetry of the connector, 16 MxiG C-termini fold into a three-stranded antiparallel  $\beta$ -sheet and augment with the N-terminal antiparallel MxiD  $\beta$ -sheet of the N0 Domain.  $\beta$ -sheet augmentation is a common protein interaction motif, well known in the context of cell-signaling pathways, ion channels and receptors [82, 83], and was previously reported for the OM and IM ring of the *Vibrio cholera* T2SS [16]. For both, the apo and effector trapped needle complex, the  $\beta$ -sheet augmentation is present with a C $\alpha$  RMSD below 0.5 Å in the MxiG C-terminus. It seems that the remaining 8 C-termini of MxiG, which we propose to fold in the space between the inner membrane ring and the connector, fold in *Salmonella* into a two-stranded  $\beta$ -sheet ( $\beta$ 10- $\beta$ 11) facing the periplasm before the C-terminus occupies the density between the IM ring and the connector [2]. Taking the good structural conservation of the *Shigella* and *Salmonella* IM ring into consideration, it is possible also *Shigella* exhibits this fold and it could not be modeled due to low resolution in this particular area.

I hypothesize that the two-stranded  $\beta$ -sheet of the third IM ring subunit C-terminus could be needed to bind periplasmic proteins which assist in assembly and/or processing of the T3SS basal body, like chaperones or proteases.

#### 3.3 Symmetry mismatch of the connector and the outer membrane ring

The C-terminal N3 and secretin domain of MxiD comprise a 15-fold symmetry, while the N-terminal connector comprises a 16-fold symmetry. It was suggested that the accommodated needle determines the 15-fold symmetry in the  $\beta$ -barrel [2], since also hexadecameric secretin rings could be isolated from recombinant expressed GspD (T2SS), which lack the central needle [3]. The absence of the C-terminus of 16<sup>th</sup> subunit could be explained by either deletion of the terminal domains of one MxiD subunit after

formation of the connector ring or recruitment of a C-terminally processed MxiD subunit to the connector. Although the fate of the C-terminal domains of the 16<sup>th</sup> MxiD subunit remains unclear, it was suggested that it is degraded [2].

Cleavage of the C-terminal domain of MxiD could occur via a periplasmic protease, as for instance proteases of the deg family, involved in protein quality control and protein folding [84, 85]. In the monomeric state, the C-terminal domain of MxiD is proposed to be unstructured, in particular the S-domain [86, 87]. Upon binding of its pilotin protein MxiM, the S-domain folds into a helix-turn-helix motive and MxiD is guided to the outer membrane [32, 86]. In the ssNMR structure, residues 549 – 566 of the S-domain are bound to MxiM [32].

If MxiM is not present, the C-terminal amino acids of MxiD would be accessible for recognition by periplasmic proteases. The last four MxiD residues, 563 – 566, are YLNY, which match the PDZ domain ligand sequence class II, X $\phi$ X $\phi$ ,  $\phi$  being a hydrophobic and X any residue [88]. Binding of the C-terminal MxiD residues to, for instance, DegP would activate the DegP protease domain, which cleaves the respective substrate between two hydrophobic residues [89]. In the case of MxiD, the stretch of amino acid 171-180 connecting the N1 and N3 domain could be accessible, and cleavage between V173 and S174 might occur. Nevertheless, it is unclear when the degradation of the C-terminus could happen. Processing after insertion of N0N1 domain into the connector would require protection of the neighboring MxiD subunits forming the OM pore by, for instance, chaperones. Processing of the MxiD C-terminus could also happen prior to insertion of the N0N1 domains into connector, degrading the 16<sup>th</sup> subunit as a single entity, followed by insertion of the N-terminal N0 and N1 domains into the connector region.

To address this question, specific inhibitors such as diisopropylfluorophosphate (DFP), which acts on the *E. coli* DegP, the later sharing a 99.8 % sequence identity with the *Shigella flexneri* orthologue, could be used. Additionally, mutating the putative cleavage site in the N1-N3 linker region might be an approach to answer this question.

### 3 Discussion and perspectives

#### 3.4 IM ring stability and assembly

The IM ring stability is mediated by several conserved, intermolecular interactions between MxiG and MxiJ. As shown for *Salmonella*, D311K is essential for effector secretion [57]. This study provides further evidence that it also impairs invasiveness and is essential for needle complex assembly.

For MxiJ, an interesting polar pod-socket mediated interaction, supported by a surrounding hydrophobic patch could be identified. The residues involved in formation of the polar pod, E111, E115 and R113 are conserved in *Salmonella* and might be further investigated by mutational analysis. In addition to the published D1-D2 linker region, which has been shown to be essential for oligomerization in *Salmonella*, this polar/hydrophobic region in the D2 domain contributes to MxiJ ring stability and could support MxiJ ring assembly [57].

Furthermore, the lower loop of MxiJ facing the export apparatus with a hydrophobic tip (F90-P99) could be resolved. In the Apo and effector trapped needle complex, the hydrophobic tip is in a similar position, facing the export apparatus. According to the inside-out assembly model suggested for *Salmonella* [2, 90], this loop, together with the upper loop exposing rather polar residues towards the export apparatus, could represent a focal point for IM ring assembly. Additionally, the putative hydrophobic interaction between the IM ring and the export apparatus might be functionally relevant, allowing rotational freedom between both needle complex components relative to each other, as suggested in a previous study [91]. Though, this putative rotational freedom would be limited by the interaction of the inner rod protein with the connector, found in *Salmonella* [2].

Point mutants of conserved residues participating in IM ring interaction and of the lower IM ring loop were generated. For the lower loop, the hydrophobicity of the side chains was lowered or removed by substituting them with large polar amino acids. Those mutants could be used to analyse the importance of the F90-P99 region for assembly and / or the functionality of the T3SS.

### 3.5 PMF dependent effector transport

Across the bacterial inner membrane, a proton motive force (PMF) is present [92-94]. The PMF, which is an electrochemical gradient established by the pH and charge differences between the periplasm and the cytoplasm, has been shown to be indispensable for effector transport through T3SSs in *Pseudomonas* and *Yersinia* [95, 96] and for flagella rotation in *Salmonella* [92-94]. The flagellar stator proteins MotA and MotB are suggested to conduct flagellar rotation, undergoing a conformational change upon proton binding [97]. Binding of a proton to the side chain of an aspartic acid residue and subsequent formation of a hydrogen bond with the backbone carbonyl group of the neighboring chain was suggested to induce a helical kink, leading to a so-called power stroke and the rotational motion of the flagellum [97]. It is important to mention that no T3SS orthologue of the stator proteins is known so far [18]. A study by Ohgita *et al.* suggested, based on attaching a fluorescent probe to the needle tip, that upon effector transport, similar to the flagellar apparatus, the T3SS needle rotates and facilitates the delivery of the effector to the host cells [91]. This observation, however, has not been repeated nor could be directly linked to effector transport yet. Furthermore, the recent structure solved at 3.8 Å published by Hu *et al.* (PDB ID 6PEM) suggests that the N-terminus of the inner rod orthologue, PrgJ, binds to the N-terminus to the orthologues MxiD N1 domain  $\beta$ -sheet [2]. This connection links the outer basal body components to the inner basal body components and stabilizes the T3SS, allowing only minimal rotational freedom of the needle with respect to the outer basal body components.

The protein MxiA, which is an orthologue of the flagellar protein FlhA and expected to be located at the export cage [59, 61, 90] is likely lost upon purification and hence cannot be resolved in the cryo-EM maps. It was suggested that FlhA is involved in proton transport to the cytoplasmic ATPase complex [62, 98]. Since fully hydrated sodium ions are reported to have a Na-O radius of  $\sim 2.4$  Å and therefore should be too large to pass through the channels [65], it is possible to speculate that protons traverse the channels. Furthermore, if protons traverse the channels, they could be involved in PMF driven effector secretion, maybe fueling the cytoplasmic ATPase complex, which contributes to stripping chaperones off to-be secreted substrates [99]. Since proton transport through water channels requires charge

### 3 Discussion and perspectives

transmission between adjacent water molecules [100], subtle local conformational changes of the IM ring subunits could interfere with this process and the overall function of the T3SS.

The conserved MxiG residue R208 is not relevant for structural integrity but needed for successful effector secretion. Its protonated amine group might coordinate a water molecule, which would be released upon protonation and replaced by an adjacent water molecule. It is possible that local conserved residues, E205 and Y263, are involved in maintaining T3 functionality by stabilizing R208, in particular E205, which is also required for the structural integrity of the needle complex. Since the cluster of E205, R208 and Y263 is conserved in *Salmonella* and other gram-negative organisms, it is tempting to assume that it is also of functional and structural relevance in orthologous structures.

Patch clamp experiments were suggested to examine the role of proton flux for effector transport. Using a protonophore like carbonyl cyanid *m*-chlorophenyl hydrazine (CCCP) [91] might be another option, but should be performed with controls, taking side effects causing a reduced functionality of the T3SS into consideration.

How the translocation of proteins through the needle lumen happens is still an unresolved question. Several mechanisms for effector secretion were suggested. Most refer to a pushing force from the bottom. A radically different approach was suggested for the growth of flagellar: Unfolded substrates are transported head-to-tail through the flagellum and an entropic pulling force is generated upon refolding and polymerization of the subunits at the top of the flagellum [101]. A similar process could be accounted for the polymerization of needle subunits, but not for effectors, since a spontaneous refolding, similar to co-translational folding of the nascent protein chain, of previously chaperoned effectors seems unlikely and was not published to-date.

### 3.6 Structural changes in the basal body upon effector transport

In both states, apo and the needle complex trapped with an effector, the IM ring is channeled, traversing two MxiG subunits and three MxiJ subunits. In the trapped state, the MxiG D2  $\beta$ -sheet is slightly lifted upwards, which could cause the reorientation of the periplasmic channel exit B into the direction of the MxiG D2 domain. It remains unknown whether this reorientation is of functional relevance.

Additional low density features are visible in the needle lumen and at the base of the export apparatus core in the cryo-EM map of the needle complex trapped with an effector. Considering the results of Dohlich *et al.* and Radics *et al.* [5, 71], the density feature in the needle lumen supports further the finding that the needle complex is trapped with an effector. Due to intrinsic flexibility of unfolded proteins, the effector was detected at low threshold levels. The unfolding grade upon transport might also vary between transported effectors, depending on their stability. Using an effector of higher molecular weight as Radics *et al.* did ( $\sim 2x$  the MW of the IpaB effector located in the *Shigella* channel) might result in better visibility in the channel by cryo-EM. Whether the extra density visible at the base of the export apparatus core is the C-terminal region of the trapped effector IpaB-knot or another subunit of the export apparatus requires further experimental analysis.

It seems that the connector and the IM ring do undergo only minor local structural changes upon effector transport, demonstrating the flexibility of the T3SS. A similar observation was found in *Salmonella* by Marlovits *et al.*, comparing effector trapped and apo cryo-EM T3SS maps [102]. In *Shigella*, initial analysis superposing tetramers of both states on one chain indicated that global reorientation of the apo and trapped subunit backbones occur in the range of  $\sim 1$  Å, respectively. Since the rod and the connector as well as the inner membrane ring and the connector are covalently bound to each other, reorientations of connector to IM ring and export apparatus to connector are limited to a rotational degree of  $\sim 22^\circ$  [2]. Normal mode analysis might help to decipher rotational reorientation of subunits or whole building blocks as the IM ring and the connector relative to each other.

## 4 Materials and methods

### 4.1 Kits, Machinery, Chemicals and consumables

The commercially available kits, fine chemicals, reagents and machines used in the experiments during this study are listed below. Kits (Table 4: Commercially available kits used during this study) were used according to manufacturer's instructions. Fine chemicals were purchased in pro analysis grade, if available.

Table 4: Commercially available kits used during this study

Designation	Manufacturer
QIAprep Spin Miniprep Kit	Quiagen
GeneJET Gel Extraction Kit	Thermo Fisher Scientific
SuperSignal West ECL Enhancer	Thermo Fisher Scientific
PCR Purification Kit	Jena Bioscience
SuperSignal West PicPLUS ECL	Thermo Scientific

Table 5: Machines used during the study

Device	Designation	Manufacturer
Analytical Balance	CP64	Sartorius
Analytical Balance	TE3102S	Sartorius
C02 incubator	Heracell vios 250i	Thermo Fisher Scientific
Cell counting chamber	Neubauer Improved	Marienfeld
Centrifuge	Avanti J-30I	Beckman Coulter
Centrifuge	5804 R	Eppendorf
Centrifuge	Tresco 21	Thermo Fisher Scientific
Chemiluminescence Detector	ImageQuant LAS 4000 mini	GE Healthcare

Cryo electron microscope	Titan Krios	FEI
Electroporation system	Gene Pulser Xcell	BioRad
Fridge and freezer	Premium	Liebherr
Glow discharger	Med 020	Bal-Tec
Incubation shaker	Multitron Pro	Infors HT
Incubator	UNB500	Memmert
Laminar airflow cabinet	Maxisafe 2020	Thermo Fisher Scientific
Light microscope	CKX 31	Olympus
Magnetic stirrer	MR3001	Heidolph Scientific Industries
Mixer	Vortex genie 2	Bio-Rad
PCR cyclor	CFX-96 Real Time 1000	Hanna instruments
pH meter	HI 221	Gilson
Pipettes	Pipetman	Bio-Rad
Power Supply	Powerpack 300	Thermo Scientific
Spectrophotometer for 260/280nm	NanoDropOD600nm	Eppendorf
Spectrophotometer for 600nm	BioPhotometer	Thermo Scientific
SpeedVac	Savant DNA120	Eppendorf
Thermomixer	Thermomixer compact	Zeiss
Transmission electron microscope	Leo 906E	Backman Coulter
Ultracentrifuge	Optima XPN-90 ChemiDoc XRS Imaging System	Biorad INTAS Science Imaging
UV cabinet	UV Transilluminator 312nm	FEI
UV Table	Mark IV	Merck Millipore
Vitrobot	MilliQ Q-Pod	
Water purifier		

Table 6: Chemicals used during the study

Designation	Manufacturer
Acrylamide / Bisacrylamid 30%	Roth
Acetic acid	Roth
Agarose	Serva
Ammonium chloride	Sigma
Ammonium persulfate (APS)	Roth
Anhydrotetracyclin (AHT)	Thermo Fisher Scientific
Bacto Agar	BD
Bromophenol Blue	Sigma Aldrich
Carbinicilline disodium salt	Roth
Chloramphenicol	Sigma Aldrich
Congo red	Sigma Aldrich
Calicum chloride	Roth
Coomassie Brilliant Blue G-250	Serva

#### 4 Materials and methods

d-Biotin	Sigma
Beta-Mercaptoethanol	Sigma
Desthiobiotin	IBA Lifesciences
Dimethylformamide (DMF)	Sigma-Aldrich
di-sodium hydrogen phosphatedihydrate	Roth
Dithiothreitol (DTT)	Enzo Life Sciences
DNA SmartLadder	Eurogentec
Dimethyl sulfoxide (DMSO)	Sigma-Aldrich
Dulbecco's Modified Eagle's Medium (DMEM)	Gibco
Dulbecco's Phosphate Buffered Saline (DPBS)	Gibco
Ethylenglycol-bis(aminoethylether)-N,N,N',N'tetraacetic acid (EGTA)	Roth
Ethanol	Merck
Ethidium bromide (EtBr)	Sigma Aldrich
Ethylenediaminetetraacetic acid (EDTA)	Serva
GelRed nucleic Acid Stain	Biotium
Glycerol	Roth
Glycine	Roth
Glucose	Roth
Hydrochloric acid	Roth
Kanamycin	Sigma Aldrich
Kanamycine	Roth
Lauryldimethylamine N-oxide (LDAO)	Sigma Aldrich
LB agar	Roth
L-Glutamine solution	Thermo Fisher Scientific
Lyophilized coffee	Fairglobe
Lysogeny broth (LB) medium (Luria/Miller)	Roth
M9 minimal salts	Sigma
Magnesium sulphate heptahydrate	Alfa Aesar
MEM Non-Essential Amino Acids solution	Thermo Fisher Scientific
Methanol	Acros
Mowiol 4-88	Merck
N,N,N',N'-Tetramethylethylenediamin (TEMED)	Bio-Rad
n-Dodecyl $\beta$ -D-maltoside (DDM)	Roth
Paraformaldehyd	Sigma Aldrich
PBS Dubelco	Biochrome
Penicillin-Streptomycine solution 100x	Thermo Fisher Scientific
Phosphotungstic acid (PTA)	Sigma Aldrich
potassium dihydrogenphosphate	Roth
Protease inhibitor complete ultra EDTA-free	Roche
Protein ladder PageRuler prestained	Thermo Fisher Scientific
Protein ladder PageRuler unstained	Thermo Fisher Scientific
Skimmed milk powder	sucofin
Sodium Chloride (NaCl)	Roth
Sodium dodecyl sulfate (SDS)	Sigma
Sodium hydroxyde	Roth
Succrose	Serva
Trichloroacetic acid	Roth

Tris –Hydrochloride (Tris –HCl)	Roth
Triton X-100	Sigma Aldrich
Trizma Base	Sigma
Trypan Blue Stain (0.4 %)	Thermo Fisher Scientific
Tryptic soy broth (TSB) medium	Sigma Aldrich
Tryptone	Sigma-Aldrich
Tryptone Soy agar (TSA)	Sigma-Aldrich
Tween20	Applichem
Xylene Cyanol FF	Serva

Table 7: Consumables used during the study

Designation	Manufacturer
Steril filters 0.2 µm lurlock	Braun
Poly-Prep Chromatography Columns	Bio-Rad
Strep-Tactin Sepharose 50% suspension	IBA
Cell culture flasks	SARSTEDT
Reaction tubes 0.5 – 2 ml	SARSTEDT
Reaction tubes 15 – 50 ml	SARSTEDT
Petri dishes	PerkinElmer
24 well plates	Corning
Pipet tips	VWR
Single use examination gloves	Microflex
PCR tubes	Thermo Fisher Scientific
PVDF membrane with 0.22 µm pore size	Millipore
Carbon coated formowar grid with 400 mesh	Electron Microscopy Science
33 mm µ-petri dish for microscopy	ibidi

## 4 Materials and methods

### 4.2 Buffer solutions

Buffers specific to experiments are included in the respective section in this chapter. Common buffer solutions and growth media are listed below, ingredients given for 1 liter of solution, if not stated otherwise. Standard buffer recipes are taken from the lab collection or Sambrook & Russel, 2001.

Table 8: List of standard buffers and solutions used in this study

Designation	Ingredients
PBS	137 mM NaCl 2.7 mM KCl 4.3 mM Na <sub>2</sub> HPO <sub>4</sub> 1.47 mM KH <sub>2</sub> PO <sub>4</sub>
TEN	50 mM Tris, pH 8.0 @4°C 5 mM EDTA 100 mM NaCl
TEND	50 mM Tris, pH 8.0 5 mM EDTA 100 mM NaCl 0.02% DDM
Lysisbuffer	100 mM Tris pH 8.0 100 mM NaCl 10% Triton X-100
DNA loading dye (6x, 10 ml)	25 mg Bromophenol Blue 25 mg Xylene Cyanol FF 3.3 ml Glycerol 6.7 ml ddH <sub>2</sub> O
TAE	40 mM Tris acetate, pH 8.0 1 mM EDTA
Congo red plates	30 g TSB 15 g Bacto Agar 0.1 g Congo red adjust pH to 7.3 and autoclave

M9 salts	64 g Na <sub>2</sub> HPO <sub>4</sub> 15 g KH <sub>2</sub> P0 <sub>4</sub> 2.5 g NaCl 5.0 g NH <sub>4</sub> Cl in 1 l H <sub>2</sub> O and autoclaved
M9 Minimal medium	200 ml M9 salts 2 ml 1M MgSO <sub>4</sub> 20 ml 20% glucose 100 µl 1 M CaCl <sub>2</sub> In 1 l
SDS-PAGE running buffer	30,2 g Tris Base 144 g Glycine 100 g SDS
Western blot transfer buffer	3,03 g Trizma base 14,4 g glycine 200 ml methanol
SDS-PAGE sample buffer (10 ml of 4x stock)	2,5 ml 1M Tris-HCl pH 6.8 1.0 g SDS 0.8 ml 0.1% Bromophenol Blue 4 ml 100% Glycerol 2 ml 14,3 M β-mercaptoethanol
PBS-T	PBS 0.04 % (v/v) Tween20
Coomassie stain	0,3 % (v/v) 37% HCl 0.01 % (w/v) Coomassie Brilliant in 1l of distilled water
SDS-PAGE destaining solution	40 % (v/v) methanol 10 % (v/v) acetic acid
12% PAGE resolving gel (15 ml)	3.8 ml 1.5 M Tris pH 8.8 6 ml 30% Acrylamide 150 µl 10% SDS 150 µl 10% APS 15 µl TEMED
4% PAGE separation gel (5 ml)	2.77 ml 0.5 M Tris pH 6.8 830 µl 30% Acrylamide 50 µl 10% SDS 50 µl 10% APS 5 µl TEMED

#### 4 Materials and methods

DMEM complete medium

DMEM (incl. 4.5 g/l glucose)  
100 u/ml Penicilline / Streptomycine  
1x non-essential amino acid  
2 mM L-Glutamine  
20% v/v fetal calf serum

---

### 4.3 Bacteria & DNA

All bacteria that were either used or generated during this study are listed below in Table 9: Bacterial strains used in this study, DNA plasmids in Table 10: Plasmid DNA used in this study and oligonucleotides used for qualitative DNA analysis, genetic modifications or generation of plasmid constructs were synthesized by MWG Eurofins and Thermo Scientific and are listed in table 11.

Constructs with pASK-IBA7+ and pASK-IBA5+ carry a 3' *strep*-tag and confer resistance to ampicillin. *His-mxiG* on the pASK5C plasmid carries a 3' *his*-tag and confers chloramphenicol resistance. These constructs have a *tet*-promoter and are inducible with anhydrotetracyclin (AHT). The sequence of *rrmA* is derived from RrmA from *Thermus thermophilus* (PDB ID: 1IPA).

The strains used for the collection of the cryo-EM data sets are *S. flexneri*  $\Delta ipaD \Delta mxiH$  + *Strep-Xa-MxiH* (apo needle complex) and *S. flexneri*  $\Delta ipaD ipaB::rrmA$  + *Strep-Xa-MxiH* (effector trapped needle complex). *S. flexneri* M90T (positive control), *S. flexneri* M90T BS176 (negative control) were used for invasion assays. For secretion assays, *S. flexneri* M90T and *S. flexneri*  $\Delta mxiG$  + *Strep-MxiG* and the respective mutant strain were tested. *Escherichia coli* DH5 $\alpha$  were used for plasmid amplification. *S. flexneri*  $\Delta ipaD \Delta mxiH$  + *His-MxiG* + *Strep-Xa-MxiH* and *S. flexneri*  $\Delta mxiG$  + *Strep-Xa-MxiH* + *His-MxiG* were designed to foster a vertical orientation of the needle complexes on the TEM grids.

Table 9: Bacterial strains used in this study

Bacterial strain	Genotype	Source
<i>S. flexneri</i> M90T	wild type strain, serovar 5a isolate	Sansonetti <i>et al.</i> (1982)
<i>S. flexneri</i> $\Delta ipaD ipaB::rrmA$ + <i>Strep-Xa-MxiH</i>	M90T <i>ipaD</i> <sup>-</sup> with <i>Strep-Xa-MxiH</i> on a IBA7+ plasmid	Lab collection, Kim Dohlich
<i>S. flexneri</i> $\Delta mxiG$ + <i>Strep-Xa-MxiH</i> + <i>His-MxiG</i>	M90T <i>mxiG</i> <sup>-</sup> with <i>Strep-Xa-MxiH</i> on a IBA7+ plasmid and <i>His-MxiG</i> on pASK-IBA5C	This study
<i>S. flexneri</i> $\Delta ipaD \Delta mxiH$ + <i>His-MxiG</i> + <i>Strep-Xa-MxiH</i>	M90T <i>ipaD</i> <sup>-</sup> <i>mxiH</i> <sup>-</sup> with <i>His-MxiG</i> on pASK5C and <i>Strep-Xa-MxiH</i> on pASK-IBA5+	This study
<i>S. flexneri</i> $\Delta ipaD ipaB::rrmA$ + <i>Strep-Xa-MxiH</i>	M90T <i>ipaD</i> <sup>-</sup> , with <i>ipaBknot</i> fusion with C-terminal-strep-tag and <i>Strep-Xa-MxiH</i> on a IBA7+ plasmid	Lab collection
<i>S. flexneri</i> M90T BS176	M90T derivative cured of	Lab collection

#### 4 Materials and methods

	virulence plasmid	
<i>S. flexneri</i> $\Delta mxiG$ + <i>Strep-MxiG</i>	M90T <i>mxiG</i> <sup>-</sup> with <i>Strep-Xa-MxiG</i> on a IBA5+ plasmid	This study
<i>S. flexneri</i> $\Delta mxiG$ + <i>Strep-MxiG_D311K</i>	M90T <i>mxiG</i> <sup>-</sup> with <i>Strep-Xa-MxiG</i> on a IBA5+ plasmid	This study
<i>S. flexneri</i> $\Delta mxiG$ + <i>Strep-MxiG_E205R</i>	M90T <i>mxiG</i> <sup>-</sup> with <i>Strep-Xa-MxiG</i> on a IBA5+ plasmid	This study
<i>S. flexneri</i> $\Delta mxiG$ + <i>Strep-MxiG_E205A</i>	M90T <i>mxiG</i> <sup>-</sup> with <i>Strep-Xa-MxiG</i> on a IBA5+ plasmid	This study
<i>S. flexneri</i> $\Delta mxiG$ + <i>Strep-MxiG_R208E</i>	M90T <i>mxiG</i> <sup>-</sup> with <i>Strep-Xa-MxiG</i> on a IBA5+ plasmid	This study
<i>S. flexneri</i> $\Delta mxiG$ + <i>Strep-MxiG_R208A</i>	M90T <i>mxiG</i> <sup>-</sup> with <i>Strep-Xa-MxiG</i> on a IBA5+ plasmid	This study
<i>S. flexneri</i> $\Delta mxiG$ + <i>Strep-MxiG_Y263F</i>	M90T <i>mxiG</i> <sup>-</sup> with <i>Strep-Xa-MxiG</i> on a IBA5+ plasmid	This study
<i>S. flexneri</i> $\Delta mxiG$ + <i>Strep-MxiG_Y263F_E205R</i>	M90T <i>mxiG</i> <sup>-</sup> with <i>Strep-Xa-MxiG</i> on a IBA5+ plasmid	This study
<i>S. flexneri</i> $\Delta mxiG$ + <i>Strep-MxiG_347-Stop</i>	M90T <i>mxiG</i> <sup>-</sup> with <i>Strep-Xa-MxiG</i> on a IBA5+ plasmid	This study
<i>Escherichia coli</i> DH5 $\alpha$	<i>fhuA2 lac(del)U169 phoA glnV44 <math>\Phi</math>80' lacZ(del)M15 gyrA96 recA1 relA1 endA1 thi-1 hsdR17</i>	Invitrogen

The His-MxiG on pASK5C plasmid was cloned with the help of Dr. Anne Stinn, the *S. flexneri*  $\Delta ipaD \Delta mxiH$  + *Strep-Xa-MxiH* strain was provided by Dr. Michele Lunelli and the *S. flexneri*  $\Delta ipaD ipaB::rrmA$  strain by Dr. Kim Dohlich, transformed with the *Strep-Xa-MxiH* plasmid from Dr. Michele Lunelli. All persons mentioned are former employees of the MPI for Infection Biology, Berlin.

Table 10: Plasmid DNA used in this study

Plasmid backbone	Insert
pASK-IBA5C	<i>His-mxiG</i>
pASK-IBA7+	<i>Strep-Xa-mxiH</i>
pASK-IBA5+	<i>Strep-Xa-mxiG</i>

The plasmid pASK-IBA7+*Strep-Xa-mxiH* listed in Table 10: Plasmid DNA used in this study has been published before by Demers *et. al* (2013) [76].

Table 11: Oligonucleotides used in this study

#	Name	Sequence (5' to 3')	Description
1	MxiGD311Af	CTGTCAGAGAAGAAGACTGACAGCCGAAAAG CTTGAGCTC	MxiG D311A forward
2	MxiGD311Ar	GAGCTCAAGCTTTTCGGCTGTCAGTTCTT CTCTGACAG	MxiG D311A forward
3	MxiGR208Ef	GGTGTCAAACAAAGAAATAAATGAGATTCA ACAATATATCAATC	MxiG R208E forward
4	MxiGR208Er	GATTGATATATTGTTGAATCTCATTTATTTTC TTTGTTTGACACC	MxiG R208E reverse
5	MxiGR208Af	GGTGTCAAACAAAGAAATAAATGCAATTCA ACAATATATCAATC	MxiG R208A forward
6	MxiGR208Ar	GATTGATATATTGTTGAATTGCATTTATTTTC TTTGTTTGACACC	MxiG R208A reverse
7	MxiGE205Rf	CTGGTGTCAAACAAAAGAATAAATAGAATT CAACAATATATC	MxiG E205R forward
8	MxiGE205Rr	GATATATTGTTGAATTCTATTTATTCTTTTG TTTGACACCAG	MxiG E205R reverse
9	MxiGE205Af	CTGGTGTCAAACAAAGCAATAAATAGAATT CAACAATATATCAATC	MxiG E205A forward
10	MxiGE205Ar	GATTGATATATTGTTGAATTCTATTTATTGC TTTGTTTGACACCAG	MxiG E205A reverse
11	MxiGY263Ff	GTTGAATTTCCGTATTTCAAAAATATTTAA	MxiG Y263F forward
12	MxiGY263Fr	TTTAATATTTTTGAAATACGGAAATTCAAC	MxiG Y263F reverse
13	K347Stop_fwd	GATGATGATTTTTAAGGTAAATCATATC	MxiG K347 Stop forward
14	K347Stop_rvs	GATATGATTTACCTTAAAAATCATCATC	MxiG K347 Stop revers
15	Xba1fwd	GAATAGTTCGACAAAAATCTAGA	Subclone Strep-MxiG from IBA5+ to IBA3C
16	HindIIIrvs	CACTTCACAGGTCAAGCTTAGTTAG	Subclone Strep-MxiG from IBA5+ to IBA3C
17	6xHisMxiG_fwd_new	TTA <b>tGGCTAGCAGAGGATCGCATCACCATC</b> <b>ACCATCACATCGAAGGGCGCATGTCTGAG</b> <b>GCAAAGAACT</b>	Subclone strep-MxiG to His-MxiG in IBA5C
18	MxiG_rvs	GATGCCATGGTCC <b>ctactat</b> ttttatctaaaaaac	MxiG

The underlined region of primers #17 and #18 listed in Table 11: Oligonucleotides used in this study mark the template binding site. The mutation site of the site directed mutagenesis primers (#1-14) is highlighted with bold letters in the respective forward primers.

## 4 Materials and methods

### 4.4 Enzymes

All enzymes for DNA and Protein- and Peptidoglycan modification listed in table 12 were purchased from the indicated manufacturer and handled according to instructions.

Table 12: Enzymes used in this study

Name	Manufacturer
DNA-modifying enzymes	
Restriction endonucleases	New England Biolabs
T4 DNA Ligase	Thermo Fisher Scientific
QuickLigase	New England Biolabs
Q5 DNA Polymerase	New England Biolabs
Phusion High-Fidelity DNA Polymerase	New England Biolabs
Dpn1	Thermo Fisher Scientific
DNase 1	Roche
Protein- and peptidoglycan modifying enzymes	
Lysozyme	Novagen
Trypsin-EDTA 0.5%	Gibco

## 4.5 Cellular Methods

### 4.5.1 General cell culture

Caco-2 cells were obtained from ATTC (ATCC HTB-37). The cells were passaged at a confluency of ~70 % and maintained in Dulbecco Modified Eagle's Medium (DMEM with sodium pyruvate, without glutamine, 4.5 g/L glucose added, Gibco), supplemented with 2mM L-Glutamine (100x, Gibco), 100 u/ml Penicilline, 100 u/ml Streptomycine (100xPEN-STREP, Gibco), 1x non-essential amino acids (100x NEAA, Gibco) and 20% v/v sterile fetal calf serum (FCS, Sigma). Cells were grown in cell culture flasks and passaged using 0.05 % Trypsin –EDTA (Gibco), sterile PBS (Gibco) and FCS-free complete medium following the guidelines of (Manuela Natoli, 2012, Toxicology in Vitro). Cell density was assessed using the Neubauer counting chamber and trypan blue stain to assess cell viability.

### 4.5.2 Gentamicin protection assay

Invasion of *Shigella* strains was quantified as described previously [103].  $2 \times 10^5$  Caco-2 cells were seeded per well in 24-well plates and grown overnight in 1ml DMEM complete. The next day, the cells were washed with FCS-free DMEM and 500  $\mu$ l DMEM without Pen/Strep (DMEM<sup>-P/S</sup>) added. 50% -70% confluent cells ( $= 3 \times 10^5$  cells/well) were infected with  $3 \times 10^7$  bacteria (log phase) to obtain a ratio of 1:100 of cells:bacteria. 0,5 ml Bacteria suspended in FCS-free DMEM were added to cells and centrifuged at 742 rcf for 10 min. Infection occurred for 1 hour at 37 °C, 0.5 % CO<sub>2</sub>. Afterwards, the cells were washed and the medium exchanged to DMEM<sup>-P/S</sup> + 100  $\mu$ g/ml gentamicin to avoid reinfection and bacteria were allowed to replicate inside cells for 2 h at 37 °C. The cells were then washed with sterile PBS and lyzed with 0.1 % (v/v) Triton X-100 in PBS and logarithmic dilutions in PBS till  $10^{-5}$  were prepared, plating the three last dilution steps on TSB Congo red agar. Input references were respective bacteria that did not undergo infection and gentamicin treatment but were otherwise treated identical, diluted and plated. Each bacterial infection sample was prepared in triplicates. Bacterial invasion was quantified by number of colony-forming units (CFU) after overnight incubation at 37°C.

### 4.6 Molecular Methods

#### 4.6.1 Polymerase Chain Reaction (PCR)

For PCR-Primer design, melting temperature  $T_m$  of the binding regions were calculated using the NEB  $T_m$  Calculator, which is based on a sodium ion concentration corrected nearest-neighbour analysis by SantaLucia et al., considering excess primer concentration (J . SantaLucia PNAS 1996 “Improved Nearest-Neighbour parameters for predicting DNA Duplex Stability”, Owczarzy et al (2004) Biochem “Effects of Sodium Ions on DNA duplex oligomers: improved Predictions of melting temperatures”). PCR Primer  $T_m$  was aimed to be 55-65°C and the  $T_m$  of the primer pair to be as close as possible. Guanine/Cytosine (GC)-content was aimed to be 40-60% of total bases and the 3'-end finishing with a Guanine or Cytosine to allow binding and 3'polymerase activity of the DNA-Polymerase. Secondary structure formation like self-dimerisation was checked using the Eurofins Oligo Analysis Tool.

DNA was amplified with commercially available enzymes listed in Table 12: Enzymes used in this study. All reactions for cloning were carried out using Q5 and Phusion High-Fidelity DNA Polymerase (New England Biolabs) according to manufacturer's instructions. dNTPs were used at 200  $\mu$ M concentration, Primers with 0.5  $\mu$ M and template DNA at 10-100 ng per reaction. The total reaction volume varied from 25 to 50  $\mu$ l and contained 0.01-0.02 U/ $\mu$ l Polymerase. DMSO was added up to 3% v/v for reactions on Guanine-Cytosine rich templates.

For amplification, DNA was initially denatured at 95 °C for 30 seconds, followed by another short denaturation (15 sec), annealing (30 sec) and elongation (1 min/kb). The latter three steps were repeated for 25-35 cycles and finished with a final elongation of 5 min. Agarose gel electrophoresis was used to analyse the PCR product for size, amount and unspecific by-products. Positive PCR products were isolated and used for conventional cloning (chapter4.6.5 Conventional cloning) or directly sent for Sanger sequencing and subsequently analysed.

#### 4.6.2 Quick-change Site-Directed Mutagenesis

In contrast to conventional PCR primers, primers for the Quick-change site-directed mutagenesis were self-complementary. The melting temperature  $T_m$  was calculated using

$$T_m = 81.5 + 0.41(\%GC) - \left(\frac{675}{N}\right) - \%mismatch$$

With  $N$  being the primer length in bases (Agilent QuickChange Site-Directed Mutagenesis kit instruction manual catalogue # 200518). Both primers carried the point mutation and were complementary to each other. Since the GC-content of some regions were between 20 -30 % only, the primer length was increased from recommended 10-15 bp flanking sites to 16-22 bp up- and downstream of the mutagenesis site to increase the annealing temperature and consequentially the primer binding specificity.

The PCR reaction contained 125 ng of respective primer, 5-50 ng of dsDNA template plasmid 1x reaction buffer and 2 units of DNA polymerase with 3'- 5' exonuclease proofreading activity (Phusion Polymerase or Q5 DNA Polymerase) in 50  $\mu$ l total volume. The reaction was carried out applying 30 sec. of initial denaturation at 95 °C, with 15 -20 cycles of denaturation for 30 sec at 95 °C, primer annealing at 54-64°C and elongation at 72°C for 2 minutes. The final elongation step was performed at 72°C for 5 minutes. DMSO was added up to 8% to increase PCR reaction efficiency. For some MxiJ mutations, the reaction was carried out separately for the forward and reverse primer to overcome the primer-dimerisation. The reactions were pooled 1:1 (v:v), heated up to 95°C for 30 seconds and cooled down, allowing annealing of mutated plasmid DNA strands. The reactions were processed as follows, like normal PCR products.

Dpn1 digest removed methylated plasmids not carrying the mutation and, 60x less efficiently (NEB product information Dpn1) hemi-methylated plasmids. The PCR products were purified using a PCR purification kit, dialysed and transformed in electro-competent *E. coli* DH5 $\alpha$  cells. Single CFU were picked, cultured in ~ 5 ml and the plasmid DNA extracted (described in Chapter 4.6.5). The isolated plasmid DNA was submitted to Sanger sequencing by Eurofins sequencing service and the chromatograms used to analyse the DNA sequence. Plasmids carrying mutation were transformed in electro-competent *Shigella* M90T  $\Delta$ *mxiG* and selected using the antibiotic resistance on the plasmid.

## 4 Materials and methods

### 4.6.3 Colony PCR

For a colony PCR, single CFU were picked and resuspended in 50 µl of water. 20µl of the suspension was topped up with 100 µl medium for restreaking while 1 µl was used as a template in a 50 µl PCR reaction volume. The initial DNA denaturation step of 95°C for 30 seconds was prolonged to 5 minutes to lyse the bacterial cells. Further steps were carried out as described in 4.6.1, Polymerase Chain reaction, PCR.

### 4.6.4 Agarose gel electrophoresis

Linear DNA strands of 200 bp and 8 kbp length were analyzed by constant field electrophoresis using 0.8-1.2 % agarose gels in TAE buffer. The agarose was molten in TAE buffer using a microwave, supplied with GelRed stain (0,1 µl/ml), poured into gel casts and allowed to cool down for 60 min at RT. Preparative and analytical electrophoresis were performed at 100-140 V. DNA SmartLadder was used as a standard with ~5 µl per lane. For analytical electrophoresis, bands were visualized using a UV cabinet. For preparative purposes, a UV table was used and the bands cleaved out with a scalpel and recovered from the agarose using the gel extraction kit.

### 4.6.5 Conventional cloning

Planning, design, theoretical cleavage and PCR, translation and control of sequencing results was carried out using Ape (A plasmid editor by M. Wayne Davis) and Serial cloner.

After successful PCR (see chapter 4.6.1 Polymerase Chain Reaction (PCR)) PCR products were purified from the reaction by preparative agarose gel electrophoresis (see chapter 4.6.4 Agarose gel electrophoresis) and GeneJET Gel Extraction kit. The concentration of purified PCR product and vector backbone was determined at 260nm with a Nanodrop Spectrophotometer. Up to 1 µg of the target plasmid backbone and the PCR product were digested with restriction enzymes according to manufacturer's recommendations. For standard DNA digestion, 10 units per 50 µl reaction were incubated for 1 h at 37 °C. The digested DNA was purified using the QIAprep Spin Miniprep kit, plasmid backbones were separated from the digestion product by preparative agarose gel electrophoresis (4.6.5 Conventional cloning). Ligation was performed using the T4 DNA Ligase trying different molar

ratios of vector:insert DNA and applying 16°C and overnight or 2h at room temperature incubations. Digested vector backbone without insert served as ligation negative control. Ligated DNA constructs were transformed in electro-competent bacterial cells (4.7.4 Transformation of bacteria) and selected using the antibiotic resistance cassette on the vector backbone. After restriction digest, ligation and successful transformation in *E.coli* DH5 $\alpha$ , a colony PCR was used to check for successful modification of the plasmid (see section 4.6.3 Colony PCR). The DNA of positive clones was isolated applying alkaline cell lysis and purification on silica gel membranes using the QIAprep Spin Miniprep kit. The concentration of isolated DNA was measured at 260nm with a Nanodrop Spectrophotometer and subjected to Sanger sequencing. The verified plasmid was transformed into the respective electro-competent *S. flexneri* strain.

## 4 Materials and methods

### 4.7 Microbiological & Biochemical Methods

#### 4.7.1 Bacterial culture

*S. flexneri* strains were grown in TSB medium or on TSB agar plates supplemented with 0.2 % w/v Congo red. *E. coli* were grown in LB medium or on LB agar plates. Antibiotics were used as listed in table 13. Adaptation to minimal medium was done on M9 minimal medium agar plates.

Table 13: Antibiotics and their concentrations used in this study

Antibiotic	Final concentration
Ampicillin	50 µg/ml
Carbenicillin	50 µg/ml
Chloramphenicol ( <i>E. coli</i> )	34 µg/ml
Chloramphenicol ( <i>S. flexneri</i> )	6 µg/ml
Kanamycin	50 µg/ml

#### 4.7.2 Adaptation to minimal medium

Minimal Medium agar supplemented with 1 mM of all 20 proteinogenic amino acids and Congo red to a final concentration of 0.01% w/v was prepared as follows: 100 ml M9 salts 5x stock solution was mixed with 11g bactoagar and autoclaved at 121 °C for 20 min. When the solution cooled down to ~ 58°C, the following sterile filtered components were added: Congo red, amino acids, MgSO<sub>4</sub> (final conc. 2 mM), glucose (final conc. 0.4% w/v), CaCl<sub>2</sub> (final conc. 0.1 mM). The pH was adjusted to 7.3 with Noah and the agar poured into plates with ~ 20 ml / plate.

The to-be-adopted strains were streaked on the plates using different concentrations of the different antibiotic required and incubated at 37°C. For example, 1/10<sup>th</sup> or 1/5<sup>th</sup> of the full required concentration (see table 4.7.1.1) gave rise to colonies, while at higher concentrations no growth was visible. Single colonies were selected and restreaked, increasing the concentration of antibiotics back to full concentration. The quality of needle complex preparations of strains adapted to M9 + amino acids agar was checked purifying the needle complex and imaging with the TEM.

#### 4.7.3 Electrocompetent cells

*E. coli* DH5 $\alpha$  and *Shigella* were sub cultured in LB and TSE medium, respectively, till the optical density (OD) of the culture reached 0.4 – 0.6 at 600nm, which corresponds to mid-log bacterial growth phase. Bacteria were harvested by centrifugation at 5.000 rcf for 10 min at 4 °C. All subsequent steps were carried out maintaining the bacteria on ice. *E. coli* DH5 $\alpha$  were washed twice with ice-cold ddH<sub>2</sub>O and once with 10 % (v/v) glycerol (sterile filtered). The final pellet was resuspended in 1-2 ml of 10 % (v/v) glycerol to obtain a ~ 50% v/v suspension of bacteria in total volume, aliquoted in 40  $\mu$ l and immediately flash-frozen in liquid N<sub>2</sub>.

*Shigella* were harvested at OD 0.4 – 0.6 and at 10.000 rcf for 10 min at 4 °C and washed with 300 mM sterile filtered sucrose. The final pellet was resuspended in 1-2 ml of 300 mM sucrose and aliquoted in 40  $\mu$ l. For later use, aliquots were flash-frozen in liquid N<sub>2</sub> and stored at -80 °C. For immediate use, cells were kept on ice.

#### 4.7.4 Transformation of bacteria

Electro-competent cells were thawed on ice or freshly prepared and briefly incubated on ice with either 50-100 ng of plasmid DNA or 10  $\mu$ l ligation reaction which had been dialysed against ddH<sub>2</sub>O for 10 min using PVDF membrane floats with 0.22  $\mu$ m pore size. 40  $\mu$ l of competent cells were mixed with the DNA in a pre-cooled electroporation cuvette (Bio-Rad, 0.1  $\mu$ m) and pulsed for 1 sec (200  $\Omega$ , 25 mF, 1.8 kV). Cells were immediately resuspended in 500  $\mu$ l TSB medium without antibiotics and incubated at 37 °C for 1h under agitation. For re-transformation, 50  $\mu$ l were plated on agar plates with selective antibiotics. For ligations, the complete mix was plated on LB agar plates with selection markers.

To introduce a plasmid into electro-competent bacteria that harbour already a plasmid, co-transformation of both plasmids, the new and one already present in the bacteria, was required.

## 4 Materials and methods

Electroporation cuvettes were recycled applying several washing steps. First, five times purified water is applied to remove cell debris, followed by 0.2M HCl for ~ 10 min to hydrolyse DNA remains. After rinsing and incubation o/n in 70% ethanol the cuvettes were dried and reused.

### 4.7.5 Secretion assay

The assay was in most points performed as described by Reinhardt *et al.* (2014). Bacteria were grown over night in TSB medium and a subculture prepared the next day. Expression of proteins encoded on an IBA-plasmid was induced using 0.2 µg/ml AHT solved in DMF at 0.1 OD<sub>600nm</sub>. The induction of T3SS was induced adding Congo red to the final concentration of 200 µg/ml. After incubation of ~ 3 h, when an OD<sub>600nm</sub> of 1 to 2 was reached, *Shigella* were harvested. The cell density was normalized to OD<sub>600nm</sub> 2/ml, bacteria were washed once with PBS and resuspended in 100 µl SDS sample buffer. The supernatant was filtered (0.22 µm) and proteins were precipitated with 10 % ice-cold (v/v) Trichloroacetic acid over night at -20 °C. Subsequent collecting of precipitated proteins was done by centrifugation at 16.100 rcf for 30 min at 4 °C. Pellets were washed once with 1 ml ice-cold acetone and centrifuged again for 30 min. Acetone was discarded directly after centrifugation and the pellets dried in a speedVac vacuum concentrator and resuspended in 50 µl 1 M TrisHCl, pH 8.5, plus 50 µl 2x SDS sample buffer. Supernatants and the equivalent bacterial lysates were analyzed by SDS-PAGE and western blotting.

### 4.7.6 Sodium dodecylsulfate polyacrylamide gel electrophoresis (SDS-PAGE)

All sodium dodecyl sulfate polyacrylamide gel electrophoresis (SDS-PAGE) were performed using manually casted 10-12 % gels. The protein samples suspended in SDS-PAGE sample buffer and a protein molecular weight standard (Protein Ladder PageRuler) were applied to the gel. To prevent aggregation, samples containing membrane proteins were not boiled prior to electrophoresis. Electrophoresis was performed at 90-120 V, with approximately 10V/cm of path through the gel. After electrophoresis, proteins were stained with coomassie stain. To reduce background staining, gels were washed 3x in deionised water to remove excess SDS which binds to coomassie.

#### 4.7.7 Western blotting

Unstained SDS-PAGE proteins gels were used with a Polyvinylidene fluoride (PVDF) membrane for the transfer of membrane proteins and with nitrocellulose membranes for proteins with a rather polar surface, as previously described [104]PVDF membranes were activated with methanol for two minutes, washed in de-ionized water and transfer buffer. A constant current of  $\sim 2 \text{ mA/cm}^2$  membrane was applied for 1 h to transfer the proteins on the membrane in a semi-dry blotter, using transfer buffer. Subsequently, unoccupied binding sites on the membrane surface were blocked with 2 % (w/v) milk powder in PBS-T for 30-60 min. Proteins were detected using monoclonal antibodies (mABs) listed in Table 14: Antibodies used in this study. Primary antibodies were incubated 1-16 h (1 h at RT or overnight at 4 °C), membranes were washed 3-4 times with PBS-T and secondary antibodies coupled to horse radish-peroxidase were incubated for 30-60 min at RT. Visualization was performed with enhanced chemiluminescence (ECL) substrate with a chemiluminescence detector cabinet.

Table 14: Antibodies used in this study

Name	Source
Anti-6xHis tag mouse mAB IgG2a	Amersham
Anti-mouse HRP linked secondary AB	Jackson ImmunoResearch
Anti-rabbit HRP linked secondary AB	Jackson ImmunoResearch
DnaK mouse monoclonal	Stressgen
MxiG mouse monoclonal 7G1	Lab collection
Anti-Strep-tagII Classic mouse monoclonal	IBA Lifesciences
Anti-IpaB	Lab collection
Anti-IpaC rabbit serum	Lab collection
DiO lipidic membrane tracer	Invitrogen
Alexa Flour 647 secondary anti-mouse AB	Invitrogen

Antibodies listed in Table 4.7.6.1 were used according manufacturer's instructions, if not indicated otherwise.

#### 4.7.8 Expression test

## 4 Materials and methods

Expression of IBA-plasmid encoded genes was induced using 0.2 µg/ml AHT. Samples were normalized on OD<sub>600nm</sub> and centrifuged. Cell pellets corresponding to OD 1/ml were resuspended in 100 µl of 1x SDS-sample buffer and equal volumes applied on SDS-PAGE gel. Western blotting was performed as described in section 4.7.7 Western blotting.

### 4.7.9 Expression and purification of needle complexes

Needle complexes were isolated from bacteria using a modification of published protocols [53, 105]. The affinity purification is based on the binding of N-terminal Strep-II-tagged needle protein MxiH to Strep-Tactin coupled beads. Strep-Tactin is an engineered version of streptavidin, showing a higher affinity to the Strep-II-tag.

800 ml of TSB medium with a reduced antibiotic concentration was inoculated 1:50 with an overnight grown bacterial culture and expression of IBA-plasmid encoded proteins induced using 200 mg/ml AHT. At late exponential growth phase of OD<sub>600nm</sub> 0.6 – 1.0, bacteria were harvested by centrifugation for 10 min at 3570g, washed in cold PBS and centrifuged again at 3500g for 10 min.

Cells were osmotically shocked by resuspension in 18% w/v sucrose, 0.1 M TrisHCl, pH 8.0, 100 mM NaCl and 1.25 mM EDTA, protease inhibitor and 0.01% w/v lysozyme for 30 – 60 min at room temperature to break the peptidoglycan layer of the bacterial membrane, checking for the formation of spheroblasts. Lysis was performed in the presence of 2% v/v Triton X-100, 100 mM MgSO<sub>4</sub> and DNase 1. Cell debris was removed by centrifugation for 20 min at 27.100g and needle complexes were harvested by centrifuging the supernatant at 185.000g for 4 h. The pelleted needle complexes were resuspended in TEND buffer in the presence of protease inhibitor at 4 °C. Another centrifugation step at 25.000g for 20 min was performed to remove contaminations. 200 µl of TEND-washed Strep-Tactin 50 % bead suspension (IBA) were added to the supernatant and incubated with gentle rotation at 4 °C for 1-2 h. The suspension was loaded on gravity flow column (Poly-Prep Chromatography Columns) and washed at least 3x with 10 column volumes of TEND buffer. Needle complexes were eluted in 40 µl steps with 25 mM Biotin dissolved in TEND buffer with an increased buffer capacity of 500 mM Tris pH 8.0 and stored on ice until further analysis with negative staining and electron microscopy (see section 4.8.1 grid preparation and negative staining). Elution fractions containing high quality needle complexes were aliquoted to 10 µl -15 µl in PCR-tubes, flash frozen in liquid nitrogen and stored in liquid nitrogen or at -80°C for further analysis.

#### 4.7.10 Immunofluorescence imaging

To analyze the co-localization of the T3SS needle with the bacterial membrane, *Shigella* M90T  $\Delta$ MxiG strains were co-transformed with MxiG mutants encoded on a pASK-IBA5plus plasmid and Strep-MxiH on a pASK-IBA3C plasmid. For co-localization studies of the MxiG mutants in the bacterial membrane, *Shigella* M90T  $\Delta$ MxiG was transformed with MxiG mutants encoded on a pASK-IBA5plus plasmid only and treated with 0.1% Triton X-100 in Dulbecco's - Phosphate buffered Saline (DPBS) and 10% w/v Lysozyme, 5 mM EDTA in DPBS at room temperature to permeabilized the bacterial membrane. Bacterial cells were fixed for 15' at RT with 4% paraformaldehyde, followed by membrane permeabilization, if required. Staining was performed with a monoclonal primary mouse anti-Strep-tag II antibody (Strep MAB-Classic, IBA) diluted 1:100 in combination with an Alexa Flour 647 secondary antibody (Invitrogen) diluted 1:200. The bacterial membrane was stained with a DiO lipophilic tracer (Invitrogen) diluted 1:100 for 10 minutes at room temperature, followed by a washing step with PBS. Bacteria were diluted in water to remove PBS and mounted in Mowiol 4-88 medium on 33 mm  $\mu$ -dishes (ibidi). For visualization, a Leica SP8 confocal microscope equipped with a 63x, N.A. 1.40 oil immersion objective was used, with excitation at 471 nm and 653 nm and operating the instrument in HyVolution mode. Deconvolution was performed with Huygens Essential (Huygens Compute Engine 18.04.0p7 64b) software using express deconvolution and standard profile. Experiments were performed multiple times.

## 4 Materials and methods

### 4.8 Negative staining and cryo-EM

#### 4.8.1 Grid preparation

The quality of isolated needle complexes was checked applying negative staining and electron microscopy. Copper grids with a formvar surface and a 3-4 nm evaporated carbon layer and 400 mesh were used. The grid surface was cleaned and the hydrophilicity increased with a glow discharger in plasma at 30-40 mA for ~ 1 - 5 min with ~0.2 mbar vacuum with argon supply and used immediately after discharging for negative staining.

#### 4.8.2 Negative staining and transmission electron microscopy (TEM)

1% w/v phosphotungstic acid (PTA) solution at pH 7.3 or uranyl acetate solution was centrifuged at top speed in a table top centrifuge for 5 minute to remove aggregates; the supernatant was used for staining. The conventional negative staining procedure described in Ohi *et al.*[106] was adopted and performed on a parafilm covered glass surface. The glow discharged grid was placed on top a 5 µl drop sample for 5 minutes, the carbon side facing the sample, allowing the needle to attach. The grid was blotted from the side with a filter paper and washed twice with 10µl of de-ionized water. 1% staining solution was incubated for 30 seconds with the grid, blotted from the side as described before and ½ of the grid blotted touching the blotting paper directing to have a variation of staining thickness on the grid. Specimens were allowed to air-dry until imaging with the transmission electron microscope.

Images of the specimens were taken in a Leo 906E transmission electron microscope by Christian Goosmann, MPI for Infection Biology Berlin and with a Talos L120C with a CETA camera at the CSSB by Dr. Michele Lunelli.

#### 4.8.3 Cryogenic electron microscopy (cryo-EM) data collection

Grid preparation and recording of the dataset was performed at CEITEC, Brno, Czech Republic, in close collaboration with Jirka Novacek. 400-mesh Quantifoil R2/2 holey grids with a continuous 2nm carbon layer were incubated with the sample and vitrified with a FEI Vitrobot Mark IV. Glow-discharging settings, sample incubation time and blotting times were optimized and the grids inspected at the electron

microscope FEI Tecnai F20. A grid that was glow discharged for 15 seconds, incubated for 5 minutes on ice with 5  $\mu\text{l}$  of sample and 2 seconds of blotting before vitrification was used for collection of the apo cryo-EM dataset. 5238 micrographs were collected with a 300 kV FEI Titan Krios microscope equipped with a falcon II detector. Each micrograph consists of 7 frames, with a exposure time of 1 second per micrograph and a total dose of  $25 \text{ e}^-/\text{\AA}^2$ . The pixel size is 1.38  $\text{\AA}$ , corresponding to  $\sim 100000$  fold magnification. The underfocus value was set between 1.5 – 4  $\mu\text{m}$ .

#### 4.8.4 Single particle analysis

Single particle analysis was performed by Dr. Michele Lunelli, HZI for Infection Biology, CSSB Hamburg, in particular from 3D classification on. Motioncorr 2.1 [107] and xmipp\_movie\_optical\_alignment ([108], Xmipp3.2 software package) were used to align individual frames. Based on power spectrum analysis and image inspection, several micrographs were removed due to drifting effects or contamination. The processing of the apo maps was done as follows: CTFFIND 4.0.17 was used to estimate defocus values and Relion 1.4 was used for subsequent data processing. 2D classification of about 1400 manually picked particles led to 5 classes that were used as templates for automated particle picking. Autopicking resulted in 171833 particles, which were compared with reference images and allowed removal of 28347 junk particles. The remaining particle set was subjected to three rounds of 2D classification, removing false particles after each round. Finally, 104272 particles were subjected to 3D classification. 77108 particles belonging to the first class of 3D classification were used for local refinement, using a  $0.9^\circ$  angular sampling rate and without imposing symmetry. Post processing included e.g. soft-masking, FSC based weighting and B-factor sharpening [109]. The reconstruction obtained of the whole needle complex (C1, no symmetry imposed) showed a resolution of 5.1  $\text{\AA}$ . Soft masks around the inner membrane ring, the outer membrane ring and the connector were built, based on the C1 reconstruction. Based on the symmetries visible in the C1 reconstruction, symmetries were applied to the masked regions of interest. 24-fold symmetry for the inner membrane ring and 16 fold symmetry for the outer membrane ring. 8-fold symmetry was applied to the region of the IM ring and the connector, since 8-fold symmetry is present in both regions. The resolution of the maps was assessed using the FSC value at 0.143 between two independent half data sets (gold standard procedure) [110].

### 4.9 Model building, structure refinement and analysis

#### 4.9.1 Model building

The C24 averaged reconstruction of IM ring shows backbone and side chain features in the periplasmic region which allowed modelling of the atomic structure for MxiJ and the periplasmic domains of MxiG. Phyre2 [111] was used to generate homology models for both proteins based on the X-ray crystal structure of the *Salmonella* homologues PrgH (PDB ID 3GR0) [45] and an EM Structure of PrgK (PDB ID 2Y9J) [53], due to their high sequence identity of ~ 25% for MxiG<sub>152-340</sub> and 52% for MxiJ<sub>21-197</sub>. The initial MxiJ model MxiJ<sub>22-189</sub> was split into two domains, MxiJ<sub>22-80</sub> and MxiJ<sub>98-189</sub>, to allow proper rigid body positioning in the map. The single subunits MxiG<sub>172-340</sub>, MxiJ<sub>22-80</sub> and MxiJ<sub>98-189</sub> were fitted as rigid body in the map with the software Chimera 1.11.2 [112] and refined using Coot 0.8.8 [113]. Manual building of the linker between the two MxiJ domains, the MxiJ N- and C-terminus and the MxiG N-terminus was done in coot and oligomerization in Chimera, followed by real-space refinement with phenix.real\_space\_refine release 2919 [114], applying NCS-like constraints between identical chains, secondary structure and geometrical restraints. The secondary structure information are based on the bonds length of atoms involved in formation of  $\alpha$  helices and  $\beta$ -sheets and their respective phi and psi angles. As a starting point for refinement, the secondary structure information of PrgH (3GR0 for amino acids 172-340 and 5TCP for 152-171 of MxiG) and PrgK (5TCP and 2Y9J for MxiJ) were used. The final models of the apo IM ring are MxiJ<sub>21-197</sub> and MxiG<sub>152-340</sub>, their Ramachandran plot scores are given in 2.7

#### Validation of the atomic models.

The connector region is formed by the two N-terminal domains of MxiD and the C-terminus of MxiG. An initial model of the hexadecameric MxiD<sub>37-171</sub> was built using the *E.coli* EscC structure (PDB 3GR5) [45] as template. MxiD<sub>37-171</sub> was fitted into the C8 map with Chimera fitmap global search. The density of the C8 map allowed *de novo* building of two of three MxiG C-termini in coot, using the large aromatic side chains as point of orientation. During refinement with phenix.real\_space\_refine geometrical and secondary structure restraints and NCS-like constraints were applied. The Ramachandran plot shows no

outliers and 87.80% of the residues are in the favoured regions. The EMRinger score is 3.50 and the approximate resolution at FSC 0.5 is  $\sim 3.7$  Å.

To build models of the trapped T3SS, the Apo- models of the connector and the IM ring were fitted as rigid bodies in their respective post-refined maps. For the connector, a C8 averaged map was used and for the inner membrane ring a 24 symmetrised map. Phenix.real\_space\_refinement was applied using NCS-like constrains, secondary structure and general geometry restraints, like for the apo needle complex models. Rotamer outlier corrections and side chain flips were performed in the cryo-EM density map using coot [113]. Model geometry and resolution data are given in chapter 2.7 Validation of the atomic models.

#### 4.9.2 Structure validation

Validation against structural overfitting was done according to Brown *et al.* [77], randomizing the model coordinates by 0.5 (connector) and 1.0 (IM ring) Ångström and refining them against the first independent map using phenix.real\_space\_refine applying geometrical and secondary structure restraints. The FSC of the model refined against the first half map ( $FSC_{work}$ ) and the first half map refined model fitted into the second half map ( $FSC_{test}$ ) were generated using phenix.mtriage, using masked model based maps. The FSC between the maps (masked model map1 vs first half map and masked model map1 vs. 2<sup>nd</sup> half map) was plotted against the resolution and checked for a) good overlap in region that does not contain noise b) no sharp decrease at the resolution limit applied upon refinement. The resolution limit of the maps applied during refinement varied around the resolution of the map estimated after post refinement.

To estimate the resolution of the model, the FSC of the masked model based map against the experimental map that was used for refinement was plotted against the inverted resolution and checked at 0.143 FSC.

Upon refinement, the geometrical quality of the model was assessed using energetically favoured positions of backbone angles in the Ramachandran plot, the root mean square deviation of bond length and angles to published structures, steric clashes between atoms, rotamers and the side chain position

## 4 Materials and methods

using the EMringer score. MolProbity [115] was used for this purpose. Outliers were checked for support by the EM map and the chemical surrounding.

The fit of the model to the EM map was quantified using the cross-correlation function implemented in Phenix.

### 4.9.3 Structural analysis

The multiple sequence alignment of the inner membrane ring was done doing a structural alignment between MxiG/PrgH (PDB ID 3GR0) (and MxiJ/PrgK (PDB ID 2Y9J) with PDBeFold [116]. Orthologue sequences were added accordingly based on the Pfam alignment families PF09480 and PF01514, selecting T3SS proteins of gram-negative bacteria that are preferably human pathogens or of other biological relevance. Clustal Omega [117] was used for aligning the last 12 amino acids of MxiG.

Electrostatic analysis was carried out with APBS [118] defining the N- and C-termini as neutral in the parse force field, two-step focusing and multiple Debye-Hückel spheres as boundary conditions. Interface analysis was performed in Pymol [119], coot and Chimera [120] and with the PISA server [121]. Transmembrane predictions are based on results of the TMpred [122] and the TMHMM pred server [123]. Predictions of the MxiJ Palmitoylation site are based on PROSITE [124] results.

For the needle channel comparison of the C1 maps, the map of the trapped needle complex was segmented with Segger inside Chimera at threshold level below 0.02 for the trapped needle complex with default settings and resampled the resulting map on the original map. To obtain the needle of the apo needle complex, a mask was created from the segmented trapped map with Relion 1.4 and multiplied with the apo needle complex C1 map.

CHEXVIS [60] was used for the analysis of the IM ring channels with a probe radius of 1.4 Å, selecting the most significant channels ranked by length and diameter. For the identification, an oligomer comprising three MxiG subunits and three MxiJ subunits was used. The electrostatic potential at the central line is based on the APBS results of the IM ring model. Map validation was done by Dr. Michele Lunelli, including the calculation of local resolution maps with the program blocres of the Bsoft package [125].

Diameter measurements of ring structures like the connector and the IM ring are based on the distance between identical atoms of neighbouring subunits applying

$$d = \frac{c}{\sin\left(\frac{360^\circ}{x}\right)}$$

With  $d$  being the diameter,  $x$  the number of identical subunits per ring structure and  $c$  the distance of identical atoms of neighbouring subunits. Several residues of the same area were selected for measurements. Statistical analysis (e.g. paired t-test) was performed to test the null-hypothesis. For calculation of the RMSD between apo and effector trapped needle complex, a sequence alignment followed by a structural superposition was done in Pymol, followed by the rms function, considering only C $\alpha$  atoms. To calculate the RMSD of *Salmonella* and *Shigella* connector and IM ring domain, the PDBeFold server was used. ProSmart ALIGN was used with a fragment length of 9 amino acids for the structural comparison of apo and trapped needle complex.

All structural figures were generated with Chimera and PyMol [119].

# References

1. Galan, J.E., M. Lara-Tejero, T.C. Marlovits, and S. Wagner, *Bacterial type III secretion systems: specialized nanomachines for protein delivery into target cells*. *Annu Rev Microbiol*, 2014. **68**: p. 415-38.
2. Hu, J., L.J. Worrall, M. Vuckovic, C. Hong, W. Deng, C.E. Atkinson, B. Brett Finlay, Z. Yu, and N.C.J. Strynadka, *T3S injectisome needle complex structures in four distinct states reveal the basis of membrane coupling and assembly*. *Nat Microbiol*, 2019.
3. Yan, Z., M. Yin, D. Xu, Y. Zhu, and X. Li, *Structural insights into the secretin translocation channel in the type II secretion system*. *Nat Struct Mol Biol*, 2017. **24**(2): p. 177-183.
4. Goessweiner-Mohr, N., V. Kotov, M.J. Brunner, J. Mayr, J. Wald, L. Kuhlen, S. Miletic, O. Vesper, W. Lugmayr, S. Wagner, F. DiMaio, S. Lea, and T.C. Marlovits, *Structural control for the coordinated assembly into functional pathogenic type-3 secretion systems*. *bioRxiv*, 2019: p. 714097.
5. Dohlich, K., A.B. Zumsteg, C. Goosmann, and M. Kolbe, *A substrate-fusion protein is trapped inside the Type III Secretion System channel in *Shigella flexneri**. *PLoS Pathog*, 2014. **10**(1): p. e1003881.
6. Burkinshaw, B.J. and N.C. Strynadka, *Assembly and structure of the T3SS*. *Biochim Biophys Acta*, 2014. **1843**(8): p. 1649-63.
7. Humphries, R.M. and A.J. Linscott, *Laboratory diagnosis of bacterial gastroenteritis*. *Clin Microbiol Rev*, 2015. **28**(1): p. 3-31.
8. WHO, *The top 10 causes of death*. Fact Sheet, 2017.
9. Hale, T.L. and G.T. Keusch, *Shigella*, in *Medical Microbiology*, th and S. Baron, Editors. 1996: Galveston (TX).
10. Mounier, J., T. Vasselon, R. Hellio, M. Lesourd, and P.J. Sansonetti, *Shigella flexneri enters human colonic Caco-2 epithelial cells through the basolateral pole*. *Infect Immun*, 1992. **60**(1): p. 237-48.
11. Mani, S., T. Wierzba, and R.I. Walker, *Status of vaccine research and development for Shigella*. *Vaccine*, 2016. **34**(26): p. 2887-2894.
12. Belotserkovsky, I. and P.J. Sansonetti, *Shigella and Enteroinvasive Escherichia Coli*. *Curr Top Microbiol Immunol*, 2018. **416**: p. 1-26.
13. Ruetz, T.J., A.E. Lin, and J.A. Guttman, *Shigella flexneri utilize the spectrin cytoskeleton during invasion and comet tail generation*. *BMC Microbiol*, 2012. **12**: p. 36.
14. Tsirigotaki, A., J. De Geyter, N. Sostaric, A. Economou, and S. Karamanou, *Protein export through the bacterial Sec pathway*. *Nat Rev Microbiol*, 2017. **15**(1): p. 21-36.
15. Schibich, D., F. Gloge, I. Pohner, P. Bjorkholm, R.C. Wade, G. von Heijne, B. Bukau, and G. Kramer, *Global profiling of SRP interaction with nascent polypeptides*. *Nature*, 2016. **536**(7615): p. 219-+.
16. Korotkov, K.V., T.L. Johnson, M.G. Jobling, J. Pruneda, E. Pardon, A. Heroux, S. Turley, J. Steyaert, R.K. Holmes, M. Sandkvist, and W.G. Hol, *Structural and functional studies on the interaction of GspC and GspD in the type II secretion system*. *PLoS Pathog*, 2011. **7**(9): p. e1002228.
17. Green, E.R. and J. Mecsas, *Bacterial Secretion Systems: An Overview*. *Microbiol Spectr*, 2016. **4**(1).
18. Diepold, A. and J.P. Armitage, *Type III secretion systems: the bacterial flagellum and the injectisome*. *Philos Trans R Soc Lond B Biol Sci*, 2015. **370**(1679).

19. Buchrieser, C., P. Glaser, C. Rusniok, H. Nedjari, H. D'Hauteville, F. Kunst, P. Sansonetti, and C. Parsot, *The virulence plasmid pWR100 and the repertoire of proteins secreted by the type III secretion apparatus of Shigella flexneri*. Mol Microbiol, 2000. **38**(4): p. 760-71.
20. Kane, C.D., R. Schuch, W.A. Day, Jr., and A.T. Maurelli, *MxiE regulates intracellular expression of factors secreted by the Shigella flexneri 2a type III secretion system*. J Bacteriol, 2002. **184**(16): p. 4409-19.
21. Kuhlen, L., P. Abrusci, S. Johnson, J. Gault, J. Deme, J. Caesar, T. Dietsche, M.T. Mebrhatu, T. Ganief, B. Macek, S. Wagner, C.V. Robinson, and S.M. Lea, *Structure of the core of the type III secretion system export apparatus*. Nat Struct Mol Biol, 2018. **25**(7): p. 583-590.
22. Thomas, N.A., W. Deng, N. Baker, J. Puente, and B.B. Finlay, *Hierarchical delivery of an essential host colonization factor in enteropathogenic Escherichia coli*. J Biol Chem, 2007. **282**(40): p. 29634-45.
23. Gallegos, M.T., R. Schleif, A. Bairoch, K. Hofmann, and J.L. Ramos, *Arac/XylS family of transcriptional regulators*. Microbiol Mol Biol Rev, 1997. **61**(4): p. 393-410.
24. Bongrand, C., P.J. Sansonetti, and C. Parsot, *Characterization of the promoter, MxiE box and 5' UTR of genes controlled by the activity of the type III secretion apparatus in Shigella flexneri*. PLoS One, 2012. **7**(3): p. e32862.
25. Koppolu, V., I. Osaka, J.M. Skredenske, B. Kettle, P.S. Hefty, J. Li, and S.M. Egan, *Small-molecule inhibitor of the Shigella flexneri master virulence regulator VirF*. Infect Immun, 2013. **81**(11): p. 4220-31.
26. Falconi, M., B. Colonna, G. Prosseda, G. Micheli, and C.O. Gualerzi, *Thermoregulation of Shigella and Escherichia coli EIEC pathogenicity. A temperature-dependent structural transition of DNA modulates accessibility of virF promoter to transcriptional repressor H-NS*. EMBO J, 1998. **17**(23): p. 7033-43.
27. Albus, A.M., E.C. Pesci, L.J. Runyen-Janecky, S.E. West, and B.H. Iglewski, *Vfr controls quorum sensing in Pseudomonas aeruginosa*. J Bacteriol, 1997. **179**(12): p. 3928-35.
28. Diepold, A., M. Amstutz, S. Abel, I. Sorg, U. Jenal, and G.R. Cornelis, *Deciphering the assembly of the Yersinia type III secretion injectisome*. EMBO J, 2010. **29**(11): p. 1928-40.
29. Deng, W., N.C. Marshall, J.L. Rowland, J.M. McCoy, L.J. Worrall, A.S. Santos, N.C.J. Strynadka, and B.B. Finlay, *Assembly, structure, function and regulation of type III secretion systems*. Nat Rev Microbiol, 2017. **15**(6): p. 323-337.
30. Kimbrough, T.G. and S.I. Miller, *Contribution of Salmonella typhimurium type III secretion components to needle complex formation*. Proc Natl Acad Sci U S A, 2000. **97**(20): p. 11008-13.
31. Korotkov, K.V., T. Gonen, and W.G. Hol, *Secretins: dynamic channels for protein transport across membranes*. Trends Biochem Sci, 2011. **36**(8): p. 433-43.
32. Schuch, R. and A.T. Maurelli, *MxiM and MxiJ, base elements of the Mxi-Spa type III secretion system of Shigella, interact with and stabilize the MxiD secretin in the cell envelope*. J Bacteriol, 2001. **183**(24): p. 6991-8.
33. Ross, J.A. and G.V. Plano, *A C-terminal region of Yersinia pestis YscD binds the outer membrane secretin YscC*. J Bacteriol, 2011. **193**(9): p. 2276-89.
34. Allaoui, A., P.J. Sansonetti, R. Menard, S. Barzu, J. Mounier, A. Phalipon, and C. Parsot, *MxiG, a membrane protein required for secretion of Shigella spp. Ipa invasins: involvement in entry into epithelial cells and in intercellular dissemination*. Mol Microbiol, 1995. **17**(3): p. 461-70.
35. Allaoui, A., P.J. Sansonetti, and C. Parsot, *MxiJ, a lipoprotein involved in secretion of Shigella Ipa invasins, is homologous to YscJ, a secretion factor of the Yersinia Yop proteins*. J Bacteriol, 1992. **174**(23): p. 7661-9.
36. Guo, E.Z., D.C. Desrosiers, J. Zalesak, J. Tolchard, M. Berbon, B. Habenstein, T. Marlovits, A. Loquet, and J.E. Galan, *A polymorphic helix of a Salmonella needle protein relays signals defining distinct steps in type III secretion*. PLoS Biol, 2019. **17**(7): p. e3000351.
37. Mills, E., K. Baruch, G. Aviv, M. Nitzan, and I. Rosenshine, *Dynamics of the type III secretion system activity of enteropathogenic Escherichia coli*. MBio, 2013. **4**(4).

38. Worrall, L.J., C. Hong, M. Vuckovic, W. Deng, J.R. Bergeron, D.D. Majewski, R.K. Huang, T. Spreter, B.B. Finlay, Z. Yu, and N.C. Strynadka, *Near-atomic-resolution cryo-EM analysis of the Salmonella T3S injectisome basal body*. Nature, 2016.
39. Barison, N., J. Lambers, R. Hurwitz, and M. Kolbe, *Interaction of MxiG with the cytosolic complex of the type III secretion system controls Shigella virulence*. FASEB J, 2012. **26**(4): p. 1717-26.
40. von Heijne, G., *The structure of signal peptides from bacterial lipoproteins*. Protein Eng, 1989. **2**(7): p. 531-4.
41. Narita, S. and H. Tokuda, *Sorting of bacterial lipoproteins to the outer membrane by the Lol system*. Methods Mol Biol, 2010. **619**: p. 117-29.
42. Dunstan, R.A., I.D. Hay, J.J. Wilksch, R.B. Schittenhelm, A.W. Purcell, J. Clark, A. Costin, G. Ramm, R.A. Strugnell, and T. Lithgow, *Assembly of the secretion pores GspD, Wza and CsgG into bacterial outer membranes does not require the Omp85 proteins BamA or TamA*. Mol Microbiol, 2015. **97**(4): p. 616-29.
43. Hoang, H.H., N.N. Nickerson, V.T. Lee, A. Kazimirova, M. Chami, A.P. Pugsley, and S. Lory, *Outer membrane targeting of Pseudomonas aeruginosa proteins shows variable dependence on the components of Bam and Lol machineries*. MBio, 2011. **2**(6).
44. Picking, W.L., H. Nishioka, P.D. Hearn, M.A. Baxter, A.T. Harrington, A. Blocker, and W.D. Picking, *IpaD of Shigella flexneri is independently required for regulation of Ipa protein secretion and efficient insertion of IpaB and IpaC into host membranes*. Infect Immun, 2005. **73**(3): p. 1432-40.
45. Spreter, T., C.K. Yip, S. Sanowar, I. Andre, T.G. Kimbrough, M. Vuckovic, R.A. Pfuetzner, W. Deng, A.C. Yu, B.B. Finlay, D. Baker, S.I. Miller, and N.C. Strynadka, *A conserved structural motif mediates formation of the periplasmic rings in the type III secretion system*. Nat Struct Mol Biol, 2009. **16**(5): p. 468-76.
46. Takizawa, Y., E. Binshtein, A.L. Erwin, T.M. Pyburn, K.F. Mittendorf, and M.D. Ohi, *While the revolution will not be crystallized, biochemistry reigns supreme*. Protein Sci, 2017. **26**(1): p. 69-81.
47. Datsenko, K.A. and B.L. Wanner, *One-step inactivation of chromosomal genes in Escherichia coli K-12 using PCR products*. Proc Natl Acad Sci U S A, 2000. **97**(12): p. 6640-5.
48. Menard, R., P. Sansonetti, and C. Parsot, *The secretion of the Shigella flexneri Ipa invasins is activated by epithelial cells and controlled by IpaB and IpaD*. EMBO J, 1994. **13**(22): p. 5293-302.
49. Piran, U. and W.J. Riordan, *Dissociation rate constant of the biotin-streptavidin complex*. J Immunol Methods, 1990. **133**(1): p. 141-3.
50. Hofmann, K., S.W. Wood, C.C. Brinton, J.A. Montibeller, and F.M. Finn, *Iminobiotin affinity columns and their application to retrieval of streptavidin*. Proc Natl Acad Sci U S A, 1980. **77**(8): p. 4666-8.
51. Knoppel, A., M. Knopp, L.M. Albrecht, E. Lundin, U. Lustig, J. Nasvall, and D.I. Andersson, *Genetic Adaptation to Growth Under Laboratory Conditions in Escherichia coli and Salmonella enterica*. Front Microbiol, 2018. **9**: p. 756.
52. Lyumkis, D., *Challenges and opportunities in cryo-EM single-particle analysis*. J Biol Chem, 2019. **294**(13): p. 5181-5197.
53. Schraidt, O. and T.C. Marlovits, *Three-dimensional model of Salmonella's needle complex at subnanometer resolution*. Science, 2011. **331**(6021): p. 1192-5.
54. Melchior, V., C.J. Hollingshead, and M.E. Cahoon, *Stacking in lipid vesicle-tubulin mixtures is an artifact of negative staining*. J Cell Biol, 1980. **86**(3): p. 881-4.
55. Lunelli, M., Kamprad A., Bürger J., Mielke T, C. M. T. Spahn, Kolbe M., *Cryo-EM structure of the Shigella type III needle complex*. Plos Pathogens.
56. Bergeron, J.R., L.J. Worrall, S. De, N.G. Sgourakis, A.H. Cheung, E. Lameignere, M. Okon, G.A. Wasney, D. Baker, L.P. McIntosh, and N.C. Strynadka, *The modular structure of the inner-*

- membrane ring component PrgK facilitates assembly of the type III secretion system basal body.* Structure, 2015. **23**(1): p. 161-72.
57. Bergeron, J.R.C., L.J. Worrall, S. De, N.G. Sgourakis, A.H. Cheung, E. Lameignere, M. Okon, G.A. Wasney, D. Baker, L.P. McIntosh, and N.C.J. Strynadka, *The modular structure of the inner-membrane ring component PrgK facilitates assembly of the type III secretion system basal body.* Structure, 2015. **23**(1): p. 161-172.
  58. Gupta, K., J.A.C. Donlan, J.T.S. Hopper, P. Uzdevinys, M. Landreh, W.B. Struwe, D. Drew, A.J. Baldwin, P.J. Stansfeld, and C.V. Robinson, *The role of interfacial lipids in stabilizing membrane protein oligomers.* Nature, 2017. **541**(7637): p. 421-424.
  59. Abrusci, P., M. Vergara-Irigaray, S. Johnson, M.D. Beeby, D.R. Hendrixson, P. Roversi, M.E. Friede, J.E. Deane, G.J. Jensen, C.M. Tang, and S.M. Lea, *Architecture of the major component of the type III secretion system export apparatus.* Nat Struct Mol Biol, 2013. **20**(1): p. 99-104.
  60. Masood, T.B., S. Sandhya, N. Chandra, and V. Natarajan, *CHEXVIS: a tool for molecular channel extraction and visualization.* BMC Bioinformatics, 2015. **16**: p. 119.
  61. Johnson, S., L. Kuhlen, J.C. Deme, P. Abrusci, and S.M. Lea, *The Structure of an Injectisome Export Gate Demonstrates Conservation of Architecture in the Core Export Gate between Flagellar and Virulence Type III Secretion Systems.* MBio, 2019. **10**(3).
  62. Minamino, T., Y.V. Morimoto, N. Hara, P.D. Aldridge, and K. Namba, *The Bacterial Flagellar Type III Export Gate Complex Is a Dual Fuel Engine That Can Use Both H<sup>+</sup> and Na<sup>+</sup> for Flagellar Protein Export.* PLoS Pathog, 2016. **12**(3): p. e1005495.
  63. Minamino, T., Y.V. Morimoto, N. Hara, and K. Namba, *An energy transduction mechanism used in bacterial flagellar type III protein export.* Nat Commun, 2011. **2**: p. 475.
  64. Makino, F., D. Shen, N. Kajimura, A. Kawamoto, P. Pissaridou, H. Oswin, M. Pain, I. Murillo, K. Namba, and A.J. Blocker, *The Architecture of the Cytoplasmic Region of Type III Secretion Systems.* Scientific Reports, 2016. **6**.
  65. Mahler, J. and I. Persson, *A study of the hydration of the alkali metal ions in aqueous solution.* Inorg Chem, 2012. **51**(1): p. 425-38.
  66. Burns, R.E., A. McDaniel-Craig, and A. Sukhan, *Site-directed mutagenesis of the Pseudomonas aeruginosa type III secretion system protein PscJ reveals an essential role for surface-localized residues in needle complex function.* Microb Pathog, 2008. **45**(3): p. 225-30.
  67. Brok, R., P. Van Gelder, M. Winterhalter, U. Ziese, A.J. Koster, H. de Cock, M. Koster, J. Tommassen, and W. Bitter, *The C-terminal domain of the Pseudomonas secretin XcpQ forms oligomeric rings with pore activity.* J Mol Biol, 1999. **294**(5): p. 1169-79.
  68. Hu, J., L.J. Worrall, C. Hong, M. Vuckovic, C.E. Atkinson, N. Caveney, Z. Yu, and N.C.J. Strynadka, *Cryo-EM analysis of the T3S injectisome reveals the structure of the needle and open secretin.* Nat Commun, 2018. **9**(1): p. 3840.
  69. Schraidt, O., M.D. Lefebvre, M.J. Brunner, W.H. Schmied, A. Schmidt, J. Radics, K. Mechtler, J.E. Galan, and T.C. Marlovits, *Topology and organization of the Salmonella typhimurium type III secretion needle complex components.* PLoS Pathog, 2010. **6**(4): p. e1000824.
  70. Nureki, O., M. Shirouzu, K. Hashimoto, R. Ishitani, T. Terada, M. Tamakoshi, T. Oshima, M. Chijimatsu, K. Takio, D.G. Vassylyev, T. Shibata, Y. Inoue, S. Kuramitsu, and S. Yokoyama, *An enzyme with a deep trefoil knot for the active-site architecture.* Acta Crystallogr D Biol Crystallogr, 2002. **58**(Pt 7): p. 1129-37.
  71. Radics, J., L. Konigsmaier, and T.C. Marlovits, *Structure of a pathogenic type 3 secretion system in action.* Nat Struct Mol Biol, 2014. **21**(1): p. 82-7.
  72. Loquet, A., N.G. Sgourakis, R. Gupta, K. Giller, D. Riedel, C. Goosmann, C. Griesinger, M. Kolbe, D. Baker, S. Becker, and A. Lange, *Atomic model of the type III secretion system needle.* Nature, 2012. **486**(7402): p. 276-9.
  73. Sani, M., A. Allaoui, F. Fusetti, G.T. Oostergetel, W. Keegstra, and E.J. Boekema, *Structural organization of the needle complex of the type III secretion apparatus of Shigella flexneri.* Micron, 2007. **38**(3): p. 291-301.

74. Kudryashev, M., M. Stenta, S. Schmelz, M. Amstutz, U. Wiesand, D. Castano-Diez, M.T. Degiacomi, S. Munnich, C.K. Bleck, J. Kowal, A. Diepold, D.W. Heinz, M. Dal Peraro, G.R. Cornelis, and H. Stahlberg, *In situ structural analysis of the Yersinia enterocolitica injectisome*. Elife, 2013. **2**: p. e00792.
75. Yip, C.K., T.G. Kimbrough, H.B. Felise, M. Vuckovic, N.A. Thomas, R.A. Pfuetzner, E.A. Frey, B.B. Finlay, S.I. Miller, and N.C. Strynadka, *Structural characterization of the molecular platform for type III secretion system assembly*. Nature, 2005. **435**(7042): p. 702-7.
76. Demers, J.P., N.G. Sgourakis, R. Gupta, A. Loquet, K. Giller, D. Riedel, B. Laube, M. Kolbe, D. Baker, S. Becker, and A. Lange, *The common structural architecture of Shigella flexneri and Salmonella typhimurium type three secretion needles*. PLoS Pathog, 2013. **9**(3): p. e1003245.
77. Brown, A., F. Long, R.A. Nicholls, J. Toots, P. Emsley, and G. Murshudov, *Tools for macromolecular model building and refinement into electron cryo-microscopy reconstructions*. Acta Crystallogr D Biol Crystallogr, 2015. **71**(Pt 1): p. 136-53.
78. Galkin, V.E., W.H. Schmied, O. Schraidt, T.C. Marlovits, and E.H. Egelman, *The structure of the Salmonella typhimurium type III secretion system needle shows divergence from the flagellar system*. J Mol Biol, 2010. **396**(5): p. 1392-7.
79. Hodgkinson, J.L., A. Horsley, D. Stabat, M. Simon, S. Johnson, P.C. da Fonseca, E.P. Morris, J.S. Wall, S.M. Lea, and A.J. Blocker, *Three-dimensional reconstruction of the Shigella T3SS transmembrane regions reveals 12-fold symmetry and novel features throughout*. Nat Struct Mol Biol, 2009. **16**(5): p. 477-85.
80. Hu, B., D.R. Morado, W. Margolin, J.R. Rohde, O. Arizmendi, W.L. Picking, W.D. Picking, and J. Liu, *Visualization of the type III secretion sorting platform of Shigella flexneri*. Proc Natl Acad Sci U S A, 2015. **112**(4): p. 1047-52.
81. Hu, B., M. Lara-Tejero, Q. Kong, J.E. Galan, and J. Liu, *In Situ Molecular Architecture of the Salmonella Type III Secretion Machine*. Cell, 2017. **168**(6): p. 1065-1074 e10.
82. Doyle, D.A., A. Lee, J. Lewis, E. Kim, M. Sheng, and R. MacKinnon, *Crystal structures of a complexed and peptide-free membrane protein-binding domain: molecular basis of peptide recognition by PDZ*. Cell, 1996. **85**(7): p. 1067-76.
83. Remaut, H. and G. Waksman, *Protein-protein interaction through beta-strand addition*. Trends Biochem Sci, 2006. **31**(8): p. 436-44.
84. Iwanczyk, J., D. Damjanovic, J. Kooistra, V. Leong, A. Jomaa, R. Ghirlando, and J. Ortega, *Role of the PDZ domains in Escherichia coli DegP protein*. J Bacteriol, 2007. **189**(8): p. 3176-86.
85. Schuhmann, H. and I. Adamska, *Deg proteases and their role in protein quality control and processing in different subcellular compartments of the plant cell*. Physiol Plant, 2012. **145**(1): p. 224-34.
86. Okon, M., T.F. Moraes, P.I. Lario, A.L. Creagh, C.A. Haynes, N.C. Strynadka, and L.P. McIntosh, *Structural characterization of the type-III pilot-secretin complex from Shigella flexneri*. Structure, 2008. **16**(10): p. 1544-54.
87. Guilvout, I., M. Chami, E. Disconzi, N. Bayan, A.P. Pugsley, and G.H. Huysmans, *Independent domain assembly in a trapped folding intermediate of multimeric outer membrane secretins*. Structure, 2014. **22**(4): p. 582-9.
88. Tonikian, R., Y. Zhang, S.L. Sazinsky, B. Currell, J.H. Yeh, B. Reva, H.A. Held, B.A. Appleton, M. Evangelista, Y. Wu, X. Xin, A.C. Chan, S. Seshagiri, L.A. Lasky, C. Sander, C. Boone, G.D. Bader, and S.S. Sidhu, *A specificity map for the PDZ domain family*. PLoS Biol, 2008. **6**(9): p. e239.
89. Kolmar, H., P.R. Waller, and R.T. Sauer, *The DegP and DegQ periplasmic endoproteases of Escherichia coli: specificity for cleavage sites and substrate conformation*. J Bacteriol, 1996. **178**(20): p. 5925-9.
90. Wagner, S., L. Konigsmayer, M. Lara-Tejero, M. Lefebvre, T.C. Marlovits, and J.E. Galan, *Organization and coordinated assembly of the type III secretion export apparatus*. Proc Natl Acad Sci U S A, 2010. **107**(41): p. 17745-50.

91. Ohgita, T., N. Hayashi, S. Hama, H. Tsuchiya, N. Gotoh, and K. Kogure, *A novel effector secretion mechanism based on proton-motive force-dependent type III secretion apparatus rotation*. FASEB J, 2013. **27**(7): p. 2862-72.
92. Paul, K., M. Erhardt, T. Hirano, D.F. Blair, and K.T. Hughes, *Energy source of flagellar type III secretion*. Nature, 2008. **451**(7177): p. 489-92.
93. Minamino, T., M. Kinoshita, and K. Namba, *Fuel of the Bacterial Flagellar Type III Protein Export Apparatus*. Methods Mol Biol, 2017. **1593**: p. 3-16.
94. Manson, M.D., P. Tedesco, H.C. Berg, F.M. Harold, and C. Van der Drift, *A protonmotive force drives bacterial flagella*. Proc Natl Acad Sci U S A, 1977. **74**(7): p. 3060-4.
95. Lee, P.C., S.E. Zmina, C.M. Stopford, J. Toska, and A. Rietsch, *Control of type III secretion activity and substrate specificity by the cytoplasmic regulator PcrG*. Proc Natl Acad Sci U S A, 2014. **111**(19): p. E2027-36.
96. Shen, D.K. and A.J. Blocker, *MxiA, MxiC and IpaD Regulate Substrate Selection and Secretion Mode in the T3SS of Shigella flexneri*. Plos One, 2016. **11**(5).
97. Mandadapu, K.K., J.A. Nirody, R.M. Berry, and G. Oster, *Mechanics of torque generation in the bacterial flagellar motor*. Proc Natl Acad Sci U S A, 2015. **112**(32): p. E4381-9.
98. Erhardt, M., P. Wheatley, E.A. Kim, T. Hirano, Y. Zhang, M.K. Sarkar, K.T. Hughes, and D.F. Blair, *Mechanism of type-III protein secretion: Regulation of FlhA conformation by a functionally critical charged-residue cluster*. Mol Microbiol, 2017. **104**(2): p. 234-249.
99. Akeda, Y. and J.E. Galan, *Chaperone release and unfolding of substrates in type III secretion*. Nature, 2005. **437**(7060): p. 911-5.
100. de Grotthuss, C.J., *Memoir on the decomposition of water and of the bodies that it holds in solution by means of galvanic electricity. 1805*. Biochim Biophys Acta, 2006. **1757**(8): p. 871-5.
101. Evans, L.D., S. Poulter, E.M. Terentjev, C. Hughes, and G.M. Fraser, *A chain mechanism for flagellum growth*. Nature, 2013. **504**(7479): p. 287-90.
102. Miletic, S., N. Goessweiner-Mohr, and T.C. Marlovits, *The Structure of the Type III Secretion System Needle Complex*. Curr Top Microbiol Immunol, 2019.
103. Sansonetti, P.J., A. Ryter, P. Clerc, A.T. Maurelli, and J. Mounier, *Multiplication of Shigella flexneri within HeLa cells: lysis of the phagocytic vacuole and plasmid-mediated contact hemolysis*. Infect Immun, 1986. **51**(2): p. 461-9.
104. Towbin, H., T. Staehelin, and J. Gordon, *Electrophoretic transfer of proteins from polyacrylamide gels to nitrocellulose sheets: procedure and some applications*. Proc Natl Acad Sci U S A, 1979. **76**(9): p. 4350-4.
105. Blocker, A., N. Jouihri, E. Larquet, P. Gounon, F. Ebel, C. Parsot, P. Sansonetti, and A. Allaoui, *Structure and composition of the Shigella flexneri "needle complex", a part of its type III secretion*. Mol Microbiol, 2001. **39**(3): p. 652-63.
106. Ohi, M., Y. Li, Y. Cheng, and T. Walz, *Negative Staining and Image Classification - Powerful Tools in Modern Electron Microscopy*. Biol Proced Online, 2004. **6**: p. 23-34.
107. Li, X.M., P. Mooney, S. Zheng, C.R. Booth, M.B. Braunfeld, S. Gubbens, D.A. Agard, and Y.F. Cheng, *Electron counting and beam-induced motion correction enable near-atomic-resolution single-particle cryo-EM*. Nature Methods, 2013. **10**(6): p. 584-+.
108. Abrishami, V., J. Vargas, X.M. Li, Y.F. Cheng, R. Marabini, C.O.S. Sorzano, and J.M. Carazo, *Alignment of direct detection device micrographs using a robust Optical Flow approach*. Journal of Structural Biology, 2015. **189**(3): p. 163-176.
109. Rosenthal, P.B. and R. Henderson, *Optimal determination of particle orientation, absolute hand, and contrast loss in single-particle electron cryomicroscopy*. J Mol Biol, 2003. **333**(4): p. 721-45.
110. Chen, S., G. McMullan, A.R. Faruqi, G.N. Murshudov, J.M. Short, S.H. Scheres, and R. Henderson, *High-resolution noise substitution to measure overfitting and validate resolution in 3D structure determination by single particle electron cryomicroscopy*. Ultramicroscopy, 2013. **135**: p. 24-35.

111. Kelley, L.A., S. Mezulis, C.M. Yates, M.N. Wass, and M.J. Sternberg, *The Pyre2 web portal for protein modeling, prediction and analysis*. Nat Protoc, 2015. **10**(6): p. 845-58.
112. Pettersen, E.F., T.D. Goddard, C.C. Huang, G.S. Couch, D.M. Greenblatt, E.C. Meng, and T.E. Ferrin, *UCSF Chimera--a visualization system for exploratory research and analysis*. J Comput Chem, 2004. **25**(13): p. 1605-12.
113. Emsley, P., B. Lohkamp, W.G. Scott, and K. Cowtan, *Features and development of Coot*. Acta Crystallogr D Biol Crystallogr, 2010. **66**(Pt 4): p. 486-501.
114. Adams, P.D., P.V. Afonine, G. Bunkoczi, V.B. Chen, I.W. Davis, N. Echols, J.J. Headd, L.W. Hung, G.J. Kapral, R.W. Grosse-Kunstleve, A.J. McCoy, N.W. Moriarty, R. Oeffner, R.J. Read, D.C. Richardson, J.S. Richardson, T.C. Terwilliger, and P.H. Zwart, *PHENIX: a comprehensive Python-based system for macromolecular structure solution*. Acta Crystallogr D Biol Crystallogr, 2010. **66**(Pt 2): p. 213-21.
115. Chen, V.B., W.B. Arendall, 3rd, J.J. Headd, D.A. Keedy, R.M. Immormino, G.J. Kapral, L.W. Murray, J.S. Richardson, and D.C. Richardson, *MolProbity: all-atom structure validation for macromolecular crystallography*. Acta Crystallogr D Biol Crystallogr, 2010. **66**(Pt 1): p. 12-21.
116. Krissinel, E. and K. Henrick, *Secondary-structure matching (SSM), a new tool for fast protein structure alignment in three dimensions*. Acta Crystallogr D Biol Crystallogr, 2004. **60**(Pt 12 Pt 1): p. 2256-68.
117. Sievers, F., A. Wilm, D. Dineen, T.J. Gibson, K. Karplus, W. Li, R. Lopez, H. McWilliam, M. Remmert, J. Soding, J.D. Thompson, and D.G. Higgins, *Fast, scalable generation of high-quality protein multiple sequence alignments using Clustal Omega*. Mol Syst Biol, 2011. **7**: p. 539.
118. Baker, N.A., D. Sept, S. Joseph, M.J. Holst, and J.A. McCammon, *Electrostatics of nanosystems: application to microtubules and the ribosome*. Proc Natl Acad Sci U S A, 2001. **98**(18): p. 10037-41.
119. Schroedinger, L., *The PyMol Molecular Graphics System, Version 2.0*. 2015.
120. Pintilie, G.D., J. Zhang, T.D. Goddard, W. Chiu, and D.C. Gossard, *Quantitative analysis of cryo-EM density map segmentation by watershed and scale-space filtering, and fitting of structures by alignment to regions*. J Struct Biol, 2010. **170**(3): p. 427-38.
121. Krissinel, E. and K. Henrick, *Inference of macromolecular assemblies from crystalline state*. J Mol Biol, 2007. **372**(3): p. 774-97.
122. K. Hofmann, W.S. *TMBASE - A database of membrane spanning protein segments*. 1993. Biol. Chem. Hoppe-Seyler
  
123. Moller, S., M.D. Croning, and R. Apweiler, *Evaluation of methods for the prediction of membrane spanning regions*. Bioinformatics, 2001. **17**(7): p. 646-53.
124. Sigrist, C.J., E. de Castro, L. Cerutti, B.A. Cuche, N. Hulo, A. Bridge, L. Bougueleret, and I. Xenarios, *New and continuing developments at PROSITE*. Nucleic Acids Res, 2013. **41**(Database issue): p. D344-7.
125. Heymann, J.B. and D.M. Belnap, *Bsoft: image processing and molecular modeling for electron microscopy*. J Struct Biol, 2007. **157**(1): p. 3-18.

# Attachment

Table 15: Globally harmonized system (GHS) declaration of dangerous substances used in this study according to chemical safety sheets, european chemicals agency (ECHA) and the GESTIS database

Substance	Danger symbol	GHS (Hazard)	GHS Maßnahmen (Precaution)
Acrylamide / Bisacrylamid 30%		H301, H312, H315, H317, H319, H332, H340, H350, H361f, H372	P201, P202, P260, P264, P280, P281, P301+P310, P302+P352, P304+P340, P305+P351+P338, P308+P313, P321, P330, P333+P313, P337+P313, P362, P405, P501
Acetic acid		H226, H314	P210, P233, P240, P241, P242, P243, P260, P264, P280, P301+P330+P331, P303+P361+P353, P304+P340, P305+P351+P338, P310, P321, P370+P378, P403+P235, P405, P501
Ammonium chloride		H302 -H 319	P305, P351, P338
Ammonium persulfate (APS)		H272, H302, H315, H317, H319, H334, H335	P210, P220, P221, P261, P264, P280, P285, P301+P312, P302+P352, P304+P340, P305+P351+P338, P321, P330, P333+P313, P337+P313, P342+P311, P362, P370+P378, P403+P233, P405, P501
Anhydrotetracycline (AHT) hydrochloride		H301, H311, H315, H319, H331, H361	P304+340, P304+312, P305+351+338, P301+330+331
Congo red		H350, H361, H319	201, 280, 308+313
Calcium chloride		H319	305+351+338
Beta-Mercaptoethanol		H302, H311, H314, H332, H411	P260, P264, P273, P280, P301+P312, P301+P330+P331, P302+P352, P303+P361+P353, P304+P340, P305+P351+P338, P310, P321, P391, P405, P501
Dimethylformamide (DMF)		H226, H312, H332; H319, H360D	P201, P210, P302+P352, P304, P340, P305+P351+P338, P308+P313
Dithiothreitol (DTT)		302, 315, 319, 335	261, 305+351+338
Ethanol		H225	P210, P233, P240, P241, P242, P243, P280, P303+P361+P353, P370+P378, P403+P235, P501
Ethidium bromide (EtBr)		H373	P260, P314, P501
Ethylenediaminetetraacetic acid (EDTA)		H226, H314	P210, P233, P240, P241, P242, P243, P260, P264, P280, P301+P330+P331, P303+P361+P353, P304+P340, P305+P351+P338, P310, P321, P370+P378, P403+P235, P405, P501
GelRed nucleic Acid Stain		H373	P260, P314, P501

Hydrochloric acid		H290-H314-H335	P260, P264, P280, P301+P330+P331, P303+P361+P353, P304+P340, P305+P351+P338, P310, P321, P403+P233, P405, P501
Methanol		H225, H301, H311, H331, H370(Augen)	P210, P261, P280.1-3+7, P301+310, P307+311, P402+433
Paraformaldehyd		H360D	P201-P308, P313
Phosphotungstic acid(PTA)		H314, H318, H290, H319	<u>280, 305+351+338, 310</u>
Sodium dodecyl sulfate (SDS)		H302, H312, H315, H319, H335	P261, P264, P280, P301+P312, P302+P352, P304+P340, P305+P351+P338, P321, P330, P332+P313, P337+P313, P362, P403+P233, P405, P501
Sodium hydroxyde		H314	P260, P264, P280, P301+P330+P331, P303+P361+P353, P304+P340, P305+P351+P338, P310, P321, P405, P501
Trichloroacetic acid		H314, H335, H410	P260, P273, P280, P301+P330+P331, P303+P361+P353, P305+P351+P338
Triton X-100		H302, H318, H411	P264, P273, P280, P301+P312, P305+P351+P338, P310, P330, P391, P501
TEMED (N,N,N',N'-tetramethylethylenediamine)		H225, H302, H314, H332	P210, P233, P240, P241, P242, P243, P260, P264, P280, P301+P312, P301+P330+P331, P303+P361+P353, P304+P340, P305+P351+P338, P310, P321, P370+P378, P403+P235, P405, P501

# List of tables

Table 1: C $\alpha$ RMSD of orthologues <i>Shigella</i> and <i>Salmonella</i> domains in the IM ring. ....	21
Table 2: C $\alpha$ RMSD of <i>Shigella</i> MxiD to <i>Salmonella</i> InvG. ....	48
Table 3: Cryo-EM data collection, refinement and validation statistics. ....	61
Table 4: Commercially available kits used during this study ....	72
Table 5: Machines used during the study ....	72
Table 6: Chemicals used during the study ....	73
Table 7: Consumables used during the study. ....	75
Table 8: List of standard buffers and solutions used in this study ....	76
Table 9: Bacterial strains used in this study. ....	79
Table 10: Plasmid DNA used in this study ....	80
Table 11: Oligonucleotides used in this study ....	81
Table 12: Enzymes used in this study ....	82
Table 13: Antibiotics and their concentrations used in this study. ....	88
Table 14: Antibodies used in this study. ....	91
Table 15: Globally harmonized system (GHS) declaration of dangerous substances used in this study .	107

# List of figures

Figure 1: <i>Shigella</i> pathogenesis.....	2
Figure 2: Overview on the T3SS architecture.....	4
Figure 3: Optimization of the elution buffer composition for needle complex isolation.....	12
Figure 4: Protein expression levels of M90T <i>ΔipaD ipaB::knot + strep-Xa-mxiH</i> before and after adaptation to minimal medium.....	13
Figure 5: Cloning of His-MxiG into pASK5C.....	15
Figure 6: Expression and purification of His-MxiG and Strep-MxiG constructs .....	17
Figure 7: The <i>Shigella</i> T3SS inner membrane ring .....	20
Figure 8: Topology plots of the inner membrane ring proteins MxiG and MxiJ. ....	21
Figure 9: Ring building motives are present in MxiG and MxiJ.....	22
Figure 10: MxiG-MxiG interaction. ....	24
Figure 11: Channels of the periplasmic IM ring. ....	25
Figure 12: A) Multiple sequence alignment of the periplasmic domains of MxiG.....	26
Figure 13: Immunofluorescent images and isolated needle complexes of <i>Shigella</i> mutant strains. ....	28
Figure 14: Expression test, Secretion Assay and Invasion assay of <i>Shigella</i> mutant strains. ....	30
Figure 15: <i>Salmonella</i> possess channels in the IM ring.....	31
Figure 16: Polar interaction of MxiG (blue) and MxiJ (orange and beige). ....	32
Figure 17: Site-directed mutagenesis of MxiG D311K. ....	33
Figure 18: Adjacent MxiJ subunits are stacked. ....	34
Figure 19: Multiple sequence alignment of MxiJ <sub>21-197</sub> .....	35
Figure 20: The MxiJ-MxiJ interaction interface. ....	36
Figure 21: Polar interaction of MxiJ. ....	37
Figure 22: C16 cryo-EM map of the <i>Shigella</i> needle complex.....	39
Figure 23: Multiple sequence alignment of MxiD <sub>34-171</sub> .....	40
Figure 24: Model of the connector. ....	41
Figure 25: Density of the C8 symmetrized post-processed map of the apo NC. ....	42
Figure 26: The $\beta$ -sheet augmentation in the connector.....	43
Figure 27: Intermolecular interaction of MxiD <sub>34-171</sub> . ....	45
Figure 28: Dimensions of the <i>Shigella</i> and <i>Salmonella</i> T3SS connector. ....	47
Figure 29 IpaB is fused with the 'trefoil'-knot protein rrmA at the C-terminus. ....	49
Figure 30: Trapped needle complexes can form extended needles. ....	50

Figure 31: Unsymmetrized C1 maps of the apo and effector trapped needle complex.....	51
Figure 32: Vertical central cross section of needle, inner rod and export apparatus core of post-refined C1 maps of apo needle complexes and effector trapped needle complexes.....	53
Figure 33: Density differences in post refined C1 maps of effector trapped and apo needle complexes... ..	54
Figure 34: Superposition of the IM ring and connector models.....	56
Figure 35: Structural changes in MxiG and MxiJ. ....	57
Figure 36: Connector of the trapped NC. ....	59
Figure 37: The MxiD $\beta$ 7 strand of the trapped NC. ....	60
Figure 38: Fourier shell correlation curves of the atomic models of the apo IM ring and the connector with their respective maps. ....	62
Figure 39: Fourier Shell Correlation curves of the atomic models of the trapped NC with their respective maps.....	63

# Acknowledgement

I would like to thank Prof. Dr. Michael Kolbe for giving me the opportunity to work on this project and for discussions and Dr. Michele Lunelli for discussions and TEM imaging. Furthermore, I would like to thank Prof. Dr. Henning Tidow for being the second reviser of the thesis and Prof. Dr. Arwen Pearson and Dr. Charlotte Uetrecht for being members of the thesis committee board.

I would like to thank the PIER graduate school to enable me to attend the cryo-EM symposium in Princeton, USA and the IMPRESS graduate school to enable me to attend the EMBL Bioinformatics Course in Hinxton, GB. I would like to acknowledge Dr. Jiří Nováček for help with preparing the sample for cryo-EM data collection and collection of the dataset at CEITEC Brno and Dr. Roland Thünauer at CSSB Hamburg for help with the fluorescence microscopy and discussions. I am grateful for the advices of Dr. Edu Mullapudi and Dr. Juana de Diego on the manuscript and Jutta Lambers and Christian Goosmann at MPI Berlin for help with needle complex isolation and for help with grid preparation, respectively.

I thank Dr. Susanne Witt, Dr. Tonio Schütze and Dr. Martin Seeger for mentoring support during last phases of the thesis and Dr. Karine dos Santos, Dr. Martin Seeger and Ivonne Bernal for help during the writing process. I would like to thank members of the Kolbe group for discussions.

# Eidesstattliche Versicherung

Gemäß der Promotionsordnung der Fakultät für Mathematik, Informatik und Naturwissenschaften der Universität Hamburg versichere ich hiermit an Eides statt, dass ich die vorliegende Arbeit selbst und ohne Benutzung anderer als der angegebenen Quellen und Hilfsmittel angefertigt habe.

Die wörtlich oder inhaltlich anderen Arbeiten entnommenen Stellen sind als Zitat bzw. Paraphrase unter genauer Quellenangabe kenntlich gemacht.

Ich versichere, dass diese Dissertation nicht in einem früheren Promotionsverfahren eingereicht wurde. Die Arbeit wurde bisher weder im In- noch im Ausland in gleicher oder ähnlicher Form einer anderen Prüfungsbehörde vorgelegt.

---

Antje Kamrad, 15.12.2019